The deposition of multilayer and gradient index thin films by Matrix Distributed Electron Cyclotron Resonance Plasma Enhanced Chemical Vapor Deposition MDECR-PECVD.

Bicher Haj Ibrahim

Laboratoire de physique des interfaces et couches minces
ÉCOLE POLYTECHNIQUE

THÈSE

présentée pour obtenir le grade de

DOCTEUR DE L'ECOLE POLYTECHNIQUE

Spécialité : Physique.

Bicher HAJ IBRAHIM

Dépôt de couches minces à saut et gradient d'indice par plasma en résonance cyclotron

The deposition of multilayer and gradient index thin films by MDECR-PECVD

Date de soutenance : le 12 avril 2007

Jury

Bernard AGIUS	**Président**
Jean-Eric BOURÉE	**Directeur de thèse**
Pavel BULKIN	**Co-directeur**
Mireille COMMANDRÉ	
Frédéric FERRIEU	**Rapporteur**
Agnès GRANIER	**Rapporteur**
Jean-Christophe ROSTAING	

LABORATOIRE DE PHYSIQUE DES INTERFACES ET COUCHES MINCES, CNRS UMR 7647
ÉCOLE POLYTECHNIQUE

"The Virtue of the man is to discipline his mind."

Friedrich Nietzsche

I offer this work to :
all those who participated from near or far
in the orientation of my life and my mind.
Especially, to the soul of my father,
to my mother,
to my fiancée,
to my sisters and their husbands,
to my beloved nephews and nieces,
to all my teachers during my studies,
and my friends.

Acknowledgements

I would thank for this work :

- **M. Bernard Drévillon** Director of Laboratoire de Physique des Interfaces et des Couches Minces at Ecole Polytechnique who received me in his laboratory, and supported me during the PhD.

- **M. Jean Eric BOURÉE** the director of my PhD., who helped me scientifically, and took care of the advancement of the PhD.

- Special thanks to **M. Pavel BULKIN** for his daily help, his orientation was essential for me to improve and achieve this project. His know-how made me save time, and encouraged me to progress steadily.

- **Miss Roelene BOTHA**, my successor in the team, for her help during her internship and her thesis.

- **M. Frédéric LIÈGE and M. Garry ROSE KITCHNER** who installed the electronic equipments, and helped me to program the control of the different parts, and with whom I appreciated work and cooperation.

- **M. Jean Luc MONCEL, M. Cyril JADAUD, M. Dominique CLÉMENT and M. Éléonor CARISTAN** who installed the mechanical parts of the experiment, and who veiled on the security of the work.

- **M. Grégory GIRARD**, the previous PhD student for his support and advice during the beginning of the PhD.

- **Mrs. Laurence CORBEL and Chantal GENESTE,** for the administrative help and the good environment they installed in the laboratory.

- From Jobin-Yvon, **Michel STHCAKOVSKY and Dmitri KOUZNETSOV.**

- Special acknowledgment to **Pere ROCA i CABARROCAS, Dmitri DAINEKA, Tatiana NOVIKOVA, Antonello DE MARTINO, Razvigor OSSIKOVSKI and Yvan BONNASSIEUX,** for the interesting scientific explanation and cooperation.

- All the team of the Laboratory LPICM for the precious moments I passed with them : **Quentin BRULIN, Céline BERNON, Ning NING, Martin FOLDYNA, Erik JOHNSON, Nans PHAM, Makrina ANASTASIADOU, Régis BISSON, Jérôme CHARLIAC, Arnaud-Julien GUILLEY, Gowtham MANOHARAN, Olivier GODDE, Laurent EUDE, Régis VANDERHAGHEN, Razvan NEGRU, Kim HYUN JONG, Alexei ABRAMOV, Yassine DJERIDANE, Costel-Sorin COJOCARU, Holger VACH, Laurent SCHWARTZ, Didier PRIBAT, Jean-Yves PAREY, Josiane MABRED, Dominique CONNE, Fatiha KAIL, Enric GARCIA-CAUREL, Dohyung KIM, Jérôme DAMON-LACOSTE, Marc CAHTELET, Van Diep BUI, Sami BEN-HATIT, Laurent PHILIPPE, Thien Hai DAO, Quang NGUYEN, Tran Thuat NGUYEN, Gregoriy DOLGONOS.**

Table of Contents

List of Figures

Nomenclature

Table of Abbreviations

AR, ARC	Antireflection, and antireflection coating
a-Si:H, pm-Si, c-Si, μc-Si	Respectively, amorphous, polymorphous, crystalline and microcrystalline silicon
EM	Electromagnetic
ECR	Electron Cyclotron Resonance
FTIR	Fourier Transform Infra Red
HDP	High Density Plasma
H, L, M	High, Low, Medium QWOT layer
ICP	Inductively Coupled Plasma
IR, UV, VIS	Infrared, Ultraviolet and Visible ranges
MFP	Mean Free Path
MW	Microwave
OES	Optical Emission Spectroscopy
OLE	Object Linking and Embedding
OPC	OLE for Process Control
PECVD	Plasma Enhanced Chemical Vapor Deposition
PEM	Photo-Elastic Modulator
PME	Phase Modulation Ellipsometry
QWOT	Quarter Wavelength Optical Thickness
RF	Radio Frequency
SE	Spectroscopic Ellipsometry
STP	Standard temperature and pressure (0°C, 1 atmosphere)
TCP	Transformer Coupled Plasma
TCP/IP	Transmission Control Protocol and the Internet Protocol

Definitions and units

- Mole: A quantity of the material corresponding to the molecular weight in grams. A mole of any gas at STP corresponds to 22.4 liters of volume.

- Avogadro's number: The number of molecules contained in one mole of any material. It equals 6.022×10^{23}.

- Pressure units: 1 standard atmosphere = 760 mm Hg = 760 torr [a]
1 Pa = 1 N/m^2 = 7.5 mtorr
1 mbar = 100 Pa = 750.06 mtorr

- sccm: Gas flow unit as Standard Cubic Centimeter per Minute, standard refers to STP [b].

$$1 \text{ sccm} = \frac{6.022\times10^{23}}{22414} = 2.69\times10^{19} \text{ molecules/min}$$

- MFP: *Mean Free Path*, is the average distance traveled by a gas molecule between two successive collisions with other molecules.
At 1 mtorr and room temperature, the MFP is about 8 cm for argon gas atoms.

- Molecule energy: The gas energy is stored as a kinetic energy (transitional, vibrational, and rotational). The average kinetic energy of a molecule depends on the absolute temperature as follows:

$$\frac{1}{2}m\overline{c^2} = \frac{3}{2}kT$$

where m is its mass, $\overline{c^2}$ is the mean square speed, and k is Boltzmann constant.

$$k = 1.38\times10^{23}\, J/Kelvin = 8.617\times10^{-5}\, eV/Kelvin$$

It gives 11605 K per eV.

[a] It comes with 35 gas molecules per cubic micrometers at 1 mtorr, which is an easy number to remember for people interested in etched semiconductors.

[b] See page xi for abbreviations.

Chapter 0

Introduction

This work is devoted to the study of the deposition of optical thin films and to the control of this process. Initially, the task was to develop a robust ellipsometric control technique for gradient refractive index layers. During the course of the work, it has evolved towards the broader area of ECR PECVD research and multilayer optical filter ellipsometry control.

Despite the fact that HDP-PECVD is used routinely in microelectronic fabrication, many questions about this technique are still unanswered. We have investigated aspects of this technique with the aim of gaining new insights on the physical processes involved.

In the thesis, the following parts of the work will be discussed, in order to present a coherent view of the subject:

1. Optical thin films, plasmas and plasma deposition technology.
2. ECR-PECVD features and development.
3. The MDECR deposition system *Venus* and the characterization of deposition plasmas.
4. Deposition of optical filters based on silicon oxynitride alloys, and several characterization techniques such as spectroscopic ellipsometry.
5. Kinetic ellipsometry and ellipsometric control of optical thin films.
6. Conclusion and recommendations for future work.

These points represent the structure of this document. They will be detailed in the next sections and expanded upon in the following chapters.

1. PECVD of Optical Thin Films

The first chapter deals with a brief history of optical thin film development. It explains the different types of materials used for the fabrication of optical filters in view of the specific requirements of this field. The basics of design and material specifications are presented, with an overview of the elementary design structures. The underlying physics is discussed along with the main principles of the thin film matrix formalism. A short review of plasma deposition techniques is presented - as well as a review of the materials used for optical thin films – in order to place the ECR-PECVD of silicon oxynitrides in the proper context. At the end of the chapter a short discussion of methods for the control of deposition will be given.

2. High Density Plasma Sources

The second chapter will be an introduction into plasma physics and ECR principles. In this chapter we will review the basic characteristics of the plasma and most common plasma parameters. The ECR effect and its principles will be expanded upon. Different types of low-pressure plasma reactors will be considered, in order to explain the choice of MDECR PECVD.

3. Implementation of MDECR-PECVD: Reactor *Venus*

The third chapter will enter into all the details of the deposition system, Venus. The general design considerations, vacuum system, microwave system, MDECR plasma source, gas distribution system and control system and software will be described. The basic operation parameters of the machine will be presented and the characterization of the deposition plasma using optical emission spectroscopy will be detailed, in order to understand the link between the plasma and deposited materials.

4. Deposition of SiO_xN_y Optical Filters by MDECR-PECVD

The fourth chapter will give insight into photoelastic modulation ellipsometry and its use in spectroscopic mode for the characterization of the optical properties of materials, which will then be applied to the silicon oxynitrides. FTIR measurements will be used in order to corroborate the results obtained by SE. The measurements will help to improve the antenna configuration in the MDECR reactor and to understand the influence of the different deposition parameters such as the precursor ratio and gas flows, the pressure, the microwave power and the radio-frequency biasing. Some direct applications of this characterization - such as a gradient index antireflection coating for the visible range and a rugate filter - will be shown and explained.

5. Real-time Control Using Multi-Channel Kinetic Ellipsometry

Advanced optical control, using multi-wavelength kinetic ellipsometry, will be the subject of the fifth chapter. The principles, main advantages and limitations of the technique will be given. Special attention will be paid to photoelastic modulation ellipsometry, including its calibration and use for plasma deposition. Various control strategies and methods will be considered. Some examples will be given, such as a Fabry-Perot filter, a Bragg mirror and a three-layer antireflection coating, in order to show the capacity and the accuracy of the method.

6. Conclusion and Perspectives

In the final chapter, the above mentioned work will be summarized. Several suggestions for the modification of the Venus system to better suit the needs of optical thin film deposition will be given. Some ideas concerning work to be done in the future will be presented.

Chapter 1

PECVD of Optical Thin Films

After a brief introduction to optical thin film technology and material requirements, this chapter discusses the different PECVD technologies. It represents a summary of the state of the art of these subjects.

1.1. Requirements for Optical Thin Film Technology

Optical thin films were first used by Josef von Fraunhofer in 1817, when he observed that the aging of lenses made them acquire a higher transmission due to their corrosion by environmental conditions. He made the first antireflection coating ever known, by etching glass through exposure to a concentrated mixture of sulfuric and nitric acid vapours. The corrosion of the glass surface increased its porosity, which reduced its refractive index and resulted in a reduced reflection.

This method was used until the beginning of the 20th century, but the fact that these lenses were less solid and consequently not very durable, made it less popular. During the 1930's, the first vacuum depositions of a MgF_2 antireflective layer was done [1]. It was developed and used extensively during the Second World War. Since then, numerous techniques and materials have been developed. Nowadays, thin film materials can broadly be divided into three different groups [2] as can be seen in Table 1.1.

The main advantage of thin film systems is their compactness on substrates; they allow the modification of properties without considerably increasing the overall dimensions of the optical system.

Table 1.1. Different types of thin film materials

Type	Example	Applications
Metals	Al, Ag, Au, Cu alloys Fe, Ni, Co	– IR and VIS mirrors – Optical storage – Magnetic layers – Broad-band absorbers – Clusters for CNTs
Semiconductors	Si, Ge, GaAs, SiC	– IR applications – Microelectronics and optoelectronics – Photovoltaics – LCD displays – Laser diodes, LEDs
Dielectrics	Oxides *(SiO_2, TiO_2, Al_2O_3, ZrO_2)* Fluorides *(MgF_2, CaF_2, Cryolite Na_3AlF_6)* Nitrides *(Si_3N_4, TiN)* Diamond	– Functional coatings – Antireflection coatings – Optical filters, windows – Protective films (abrasion-resistant, encapsulation layers,…) – Semiconductor applications

The increasing requirements of new applications have resulted in the continuous development of new components based on optical thin films, such as different types of AR[a] coatings, encapsulation layers for organic devices, narrow band-pass filters, laser mirrors, beam splitters and waveguides. As a result of these developments, interest in transparent dielectrics is greater than ever. These components are widely used in different areas, such as telecommunications, imaging, medical instruments, meteorology, and many others. They influence our daily lives, as AR coatings for the visible range on spectacles and cameras, hot or cold mirrors for dentistry, AR or hydrophobic coating on cars' windshields, etc. Dielectrics are also widely used, as mentioned above, in microelectronics and displays.

In this study, we are interested in the in-situ control of the deposition of silica and silicon-oxynitride layers, as well as their structural and optical properties. All these films have been fabricated mainly for optical filter applications.

[a] cf. Chapter 0 for the abbreviations used in the manuscript.

1.1.1 The Design of Optical Thin Films

In designing and manufacturing optical thin films, one should take into consideration three sets of factors [2, 3]:

- **Design Specifications**

  These include the transmittance, reflectance, absorption, spectral range and angle of incidence. A beam splitter of 60% transmittance, with low absorption in the visible range (400-700 nm) at an incidence angle of 45° can be considered as an example. The tolerance on these specifications is also important, depending on the application. For example, 2% reflectance for a commercial AR coating for spectacles can be acceptable whereas the same value can be catastrophic for a visible range telescope containing more than 20 reflective interfaces, since it would result in a drop of the total transmittance down to 67% and dramatically reduced visibility and luminance.

- **Optical Properties of the Materials**

  These include the refractive index, absorption and dispersion for the substrate, medium and deposited layers. These properties determine the choice of materials to be used, the number of layers in the design and the thickness of each layer. They can be represented by the complex index:

$$N(\lambda) = n(\lambda) - i \cdot k(\lambda)$$

  where *n* represents the refractive index and *k* the extinction coefficient, dependence on λ being the dispersion of the material.

  The specified precision of *n* and *k* values usually depends on the application. For optical coatings (excluding waveguides) it is between 0.01 and 0.001. The accuracy of the deposition method in terms of index reproducibility influences these properties and should also be taken into consideration.

- **Material Constraints**

These may result from other, non-optical properties of the materials and may limit the applications for which different materials can be used. Some of these constraints may include: availability, cost, aging or long-term stability, roughness, water incorporation, laser damage threshold, resistance to heating and stress, adhesion, hardness, toxicity, hydrophilicity[a] or hydrophobicity. These constraints also include the available deposition technology, thus the importance of its choice and the need for its constant improvement.

In practice, optical designs are first explored theoretically[b], with the aid of special software. They are then adapted to the design specifications. The choice of materials requires the consideration of available technology and the area of application. Usually a very simple starting design is chosen. To achieve the required specifications, an intelligent iterative optimization procedure is then performed. Several software packages are available commercially for this purpose. The most commonly used are *FilmStar* by FTG Software, *TFCalc* by Software Spectra Inc., *Essential Macleod* by the Thin Film Center USA and *Optilayer* by Optilayer Ltd. Russia, or different in-house programs. They allow the fitting of simple targets for reflectance and/or transmittance or for a larger number of design parameters, and they all contain a database of generic materials. Some of them also allow the treatment of graded index layers, which are acquiring more importance with the development of new deposition technologies[2].

Figure 1.1 shows the most common types of optical designs such as AR coatings, laser mirrors, filters and beam splitters.

[a] Hydrophilicity *(hydrophilia)* is the chemistry term used to describe the affinity of a material for water. Hydrophobicity *(hydrophobia)* is the chemistry term used to describe the repulsion of a material for water. The terms *hydrophilia/hydrophobia* are used more for medical or psychological states.

[b] Good references for optical designs include *Thin Film Optical Filters* by H. A. Macleod, and *Design of Optical interference Coatings* by A. Thelen.

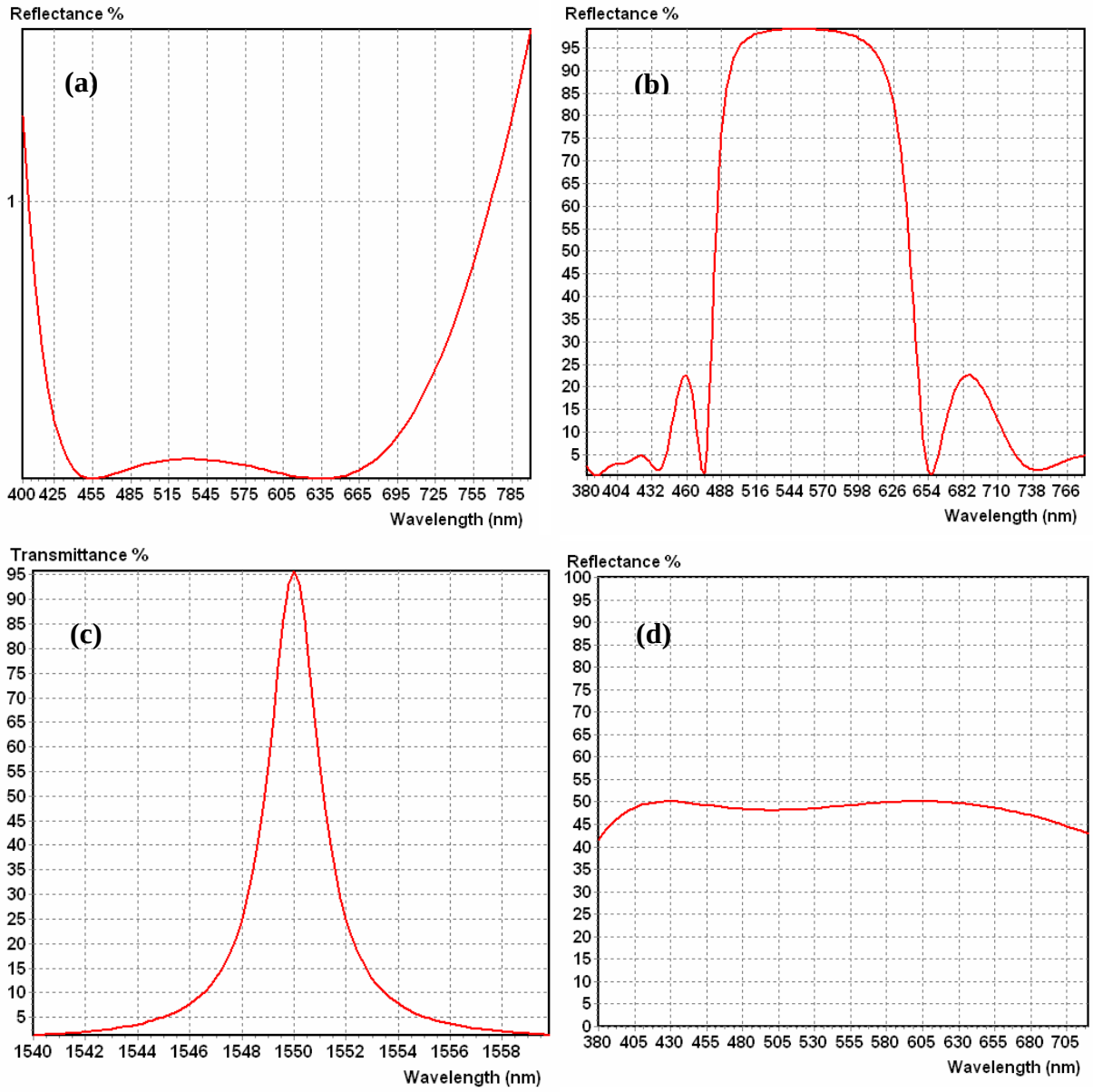

Figure 1.1. Most common types of optical depositions (all at a normal angle of incidence) : (a) three layer standard M2HL visible AR coating, (b) HL-multilayer laser mirror, (c) HL-multilayer narrow-band filter, (d) 50 % visible range beam splitter.

1.1.2 The Theory of Optical Thin Films: The Matrix Formalism

Optical thin films have been studied comprehensively during the past fifty years. Nowadays, conferences and meetings are periodically organized in order to exchange ideas and discuss the state-of–the-art of deposition and characterization techniques, designs and software[a]. At this point in time, the design of optical thin films (using exact calculations and available software) is an easier stage than their manufacture [4]. The manufacturing of optical filters, involving the use of deposition and control techniques, has always been a limiting factor and is still the subject of intense research. Improvements in filter accuracy and the fabrication of more complex filters with new specifications or special spectral shapes using new deposition tools are areas of continuing interest for scientists and engineers alike.

F. Abelès, university of Pierre & Marie Curie.

The matrix representation is a very practical method for the design and calculation of optical layer stacks [5-9]. We are interested by its study at oblique incidence, which is the general case, and which was first treated by F. Abelès. The case of normal incidence is much simpler and it can be found in many books concerning optics.

At oblique incidence, the response of an interface to a plane wave is sensitive to its polarization. After reflection or transmission, the polarization may change in different ways. Conventionally, two orthogonal linear polarizations are considered as a basis. Figure 1.2 shows these polarizations with the positive direction convention. These are the polarizations with electric fields parallel (p-polarized light) or perpendicular (s-polarized light) to the plane of incidence[b]. The incidence point is the phase reference [10].

[a] See the *Topical Meetings on Optical Interference Coatings* of the Optical Society of America.

[b] p refers to *parallel* and s to *senkrecht* in German. In electromagnetic wave theory, they are correspondingly called TM (transverse magnetic) waves and TE (transverse electric) waves, respectively.

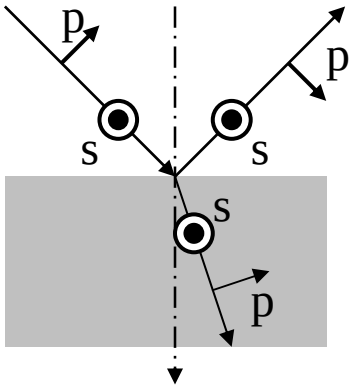

Figure 1.2. Conventions of *s* and *p* polarizations.

Each optical layer with constant index can be represented by a 2x2 complex matrix called an *Abelès Matrix*. This matrix links the EM field on the two interfaces of the layer.

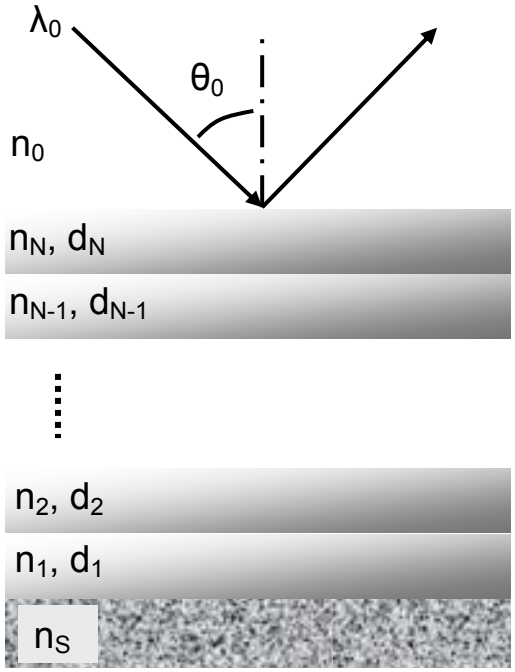

Figure 1.3. Representation of a multilayer stack.

For the j^{th} layer in the multilayer stack shown in Figure 1.3, with n_j as refractive index, d_j as thickness, λ_0 as wavelength of the light in free space and with angle of incidence θ_j, the change of phase introduced by the layer to the EM wave is:

$$\varphi_j = \frac{2\pi d_j}{\lambda_0} n_j \cos\theta_j \qquad (1.1)$$

The Abelès matrix for this layer is written as [8]:

$$M_j = \begin{pmatrix} \cos\varphi_j & \frac{i}{q_j}\sin\varphi_j \\ iq_j \sin\varphi_j & \cos\varphi_j \end{pmatrix} \quad (1.2)$$

The *tilted admittance*, q is given by the following formula for s-polarization:

$$q_j = n_j \cos\theta_j \quad (1.3)$$

and for p-polarization:

$$q_j = \frac{n_j}{\cos\theta_j} \quad (1.4)$$

For a multilayer stack (Figure 3), the resulting matrix is the product of all the layers matrices:

$$A = \begin{pmatrix} a_{11} & a_{12} \\ a_{21} & a_{22} \end{pmatrix} = \prod_{j=N}^{1} M_j \quad (1.5)$$

NB: The layer number j is counted starting from the substrate, in order to be able to easily write an iterative matrix formula:

$$A_j = M_j A_{j-1} \quad (1.6)$$

The resulting vector can be written as follows:

$$\begin{pmatrix} B \\ C \end{pmatrix} = A \times \begin{pmatrix} 1 \\ q_S \end{pmatrix} \quad (1.7)$$

Where S refers to the substrate and q is defined according to polarizations as before.

With $Y = \frac{C}{B}$, we deduce the Fresnel coefficients[9] in amplitude[a]

$$r_S = \frac{Y_{0,S} - Y_S}{Y_{0,S} + Y_S} \quad (1.8)$$

$$r_P = \frac{Y_P - Y_{0,P}}{Y_P + Y_{0,P}} \quad (1.9)$$

[a] R. Petit in his book, *Ondes Électromagnétiques en radioélectricité et en optique,* did a very interesting study of a single plane interface and multilayer system. He demonstrated these formulas in a methodological way, with the use of clear and more detailed sign conventions and boundary conditions (the continuity of tangential components of the EM field).

And for the transmittance:

$$t_S = \frac{2Y_{0,S}}{Y_{0,S} + Y_{S,S}} \tag{1.10}$$

$$t_P = \frac{2Y_{S,P}}{Y_{0,P} + Y_{S,P}} \tag{1.11}$$

In terms of intensity, the same expression can be used for the reflectance for the two polarizations separately:

$$R = |r|^2 \tag{1.12}$$

While the transmittance is given by the following[9, 10]:

$$T = \begin{vmatrix} \mathrm{Re}\left(\frac{Y_{0,S}}{Y_{S,S}}\right) |t_S|^2 \\ \mathrm{Re}\left(\frac{Y_{0,P}}{Y_{S,P}}\right) |t_P|^2 \end{vmatrix} \tag{1.13}$$

In the case of normal incidence, the result is no longer sensitive to polarization. If we imagine a decrease of the incidence angle until it reaches zero in Figure 1.3, incident and reflected p-polarization direction conventions become identical. Since we can no longer define a plane of incidence, there is no difference between s and p anymore.

1.1.3 Thin Film Deposition

Manufacturing methods of thin films can be divided into two categories: physical deposition processes and chemical deposition processes [11-14]. With the exception of the electroplating of metals, processes usually pass through an intermediate gas phase, so they are called Physical Vapor Deposition (PVD) or Chemical Vapor Deposition (CVD). Figure 1.4 shows the main PVD and CVD technologies.

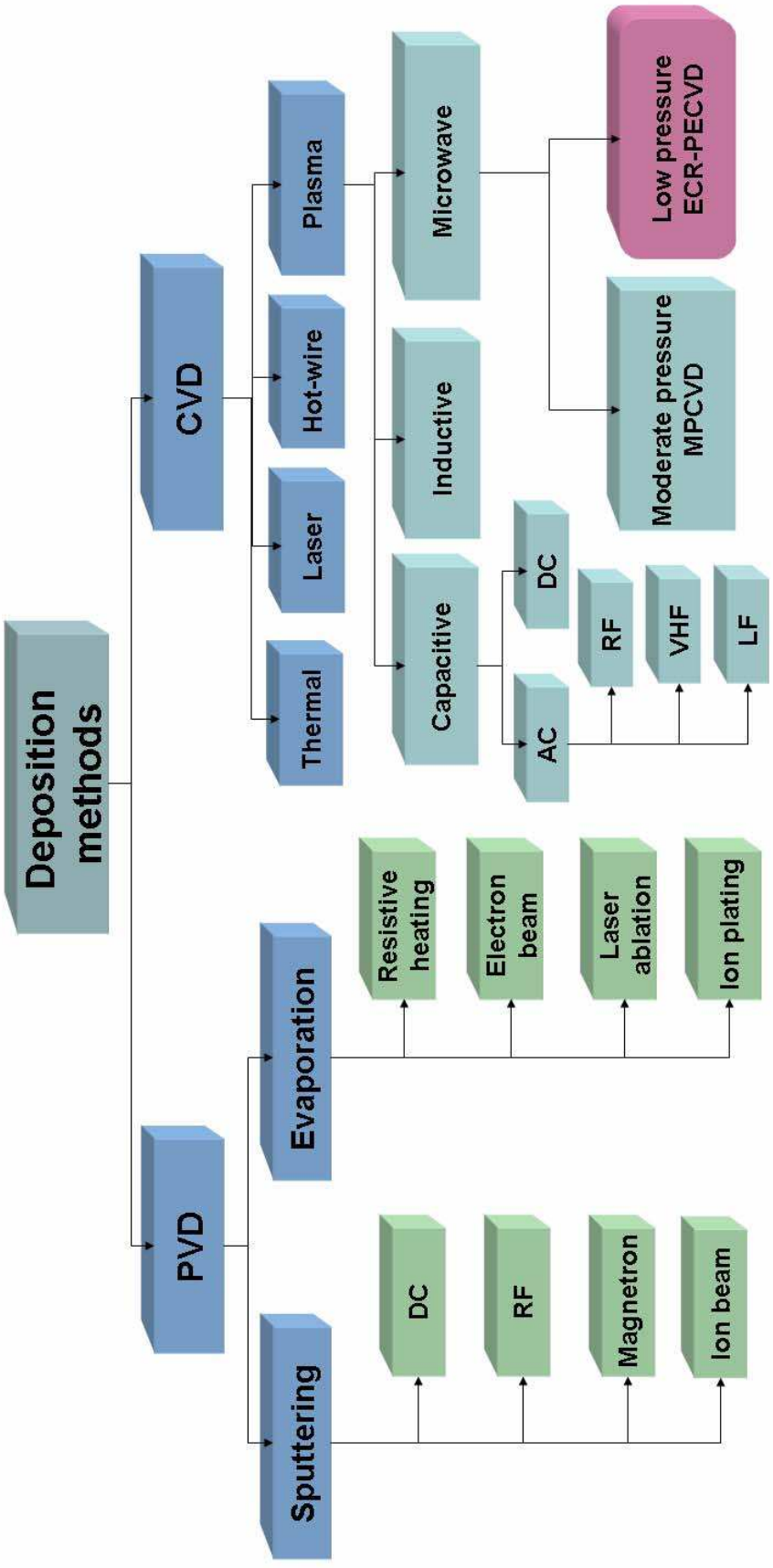

Figure 1.4. Thin film deposition techniques.

1.2. Principles of PECVD : Different Deposition Reactors

Chemical Vapor Deposition [11-13] is the formation of a film of solid phase on a heated substrate, using chemical reactions of precursors in the gaseous phase. This technique is widely used in the manufacturing of microelectronics and optical components, because it is a well controlled and fast process, and allows the use of oriented growth (epitaxy), large substrates, and a large variety of materials. It also allows the accurate control of the film composition and properties by changing the gas mixture, temperature and other process parameters.

Figure 1.5 shows a typical schema of a CVD reactor. A typical example of CVD process is the deposition of polycrystalline silicon by pyrolysis of silane gas at 650°C which leads to decomposition of the gas by the following reaction:

$$SiH_4(gas) \rightarrow Si(solid) + 2H_2(gas)$$

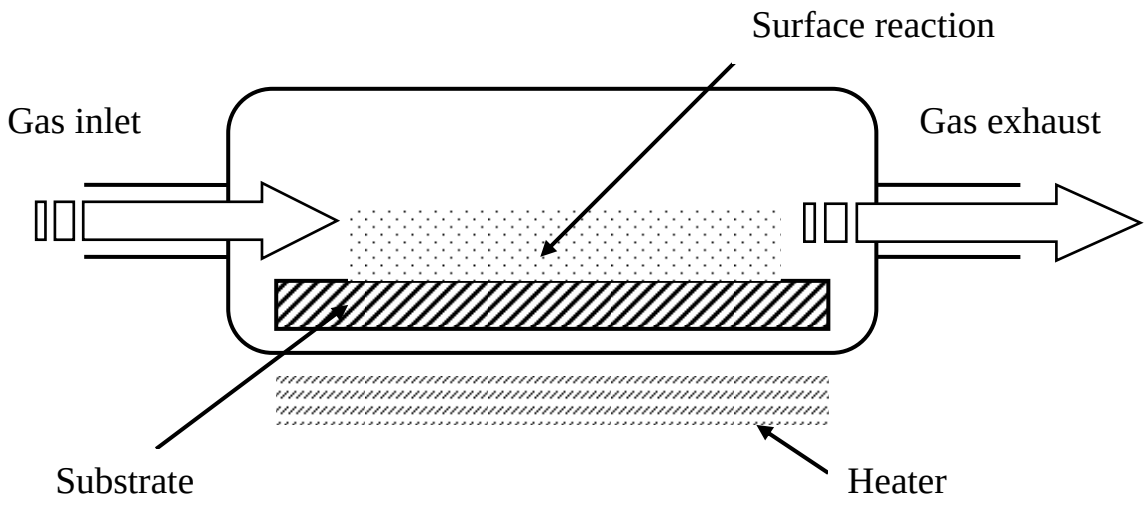

Figure 1.5. Standard CVD reactor.

Many different CVD techniques have been developed such as atmospheric pressure (APCVD), low-pressure (LPCVD), hot-wire (HWCVD), laser-enhanced (LECVD) and plasma enhanced (PECVD).

PECVD uses energetic electrons to dissociate and ionize neutral molecules of precursors and thus activate reactions which would normally require high temperatures in typical CVD[a]. This gives the possibility of depositing a larger variety of materials onto many different substrate types, provided the necessary gas phase precursors exist. It also enables different types of etching, cleaning and deposition processes. As plasmas are partially ionized gases, they have found applications in many different fields: thermonuclear fusion research, welding technology, industrial exhaust gas treatment, sterilization of medical tools, fluorescent lights and plasma displays [15].

The plasma commonly used in deposition reactors is a **cold plasma**, named so because the temperature of the neutrals and ions is less than 5000 K. It is composed of relatively hot electrons (several eV) and of colder molecules, radicals and ions. The high temperature of the electrons compared to that of the neutrals and ions can be attributed to the electrons' smaller mass. The energy exchange between the electrons, ions and neutrals also has a low probability when working at low pressure, because of the increased mean free path (MFP)[b]. The plasma reactors' dimensions usually need to be larger than the MFP to make electrons exchange energy with molecules before impinging onto the walls. The reason for working at low pressure is to have an MFP large enough to ensure that the electrons reach an energy higher than the ionization energy of the molecules, as depicted in Figure 1.6.

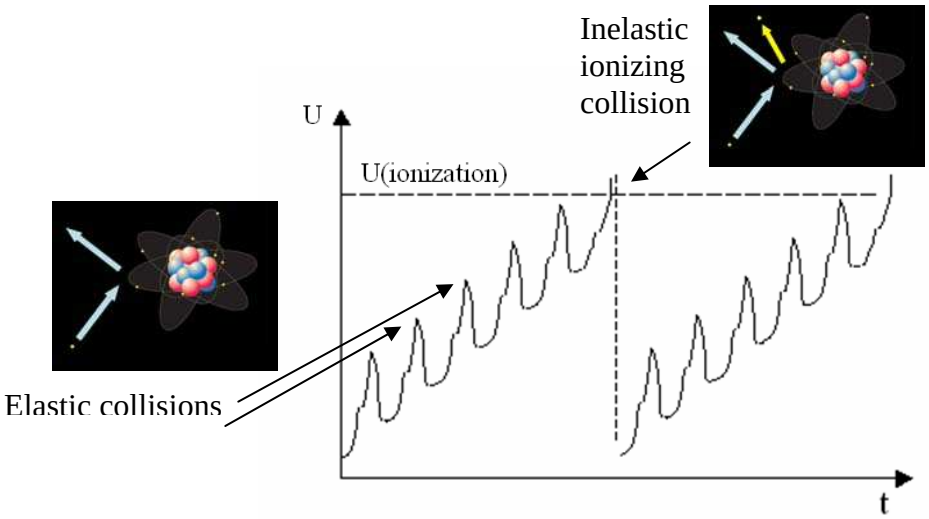

Figure 1.6. Electron-molecule collisions in plasma.

[a] For example, the CVD of SiO_xN_y usually requires temperatures between 700-900°C, while it can be done at 300°C in PECVD systems and at room temperature in ECR PECVD systems.
[b] For the definition of MFP see the list of definitions and units page xii.

The advantage of cold plasmas is the existence of a large number of ions and radicals which are not available in thermal equilibrium. The transfer of the energy to electrons from an electromagnetic field allows them to reach the ionization energy of the gas molecules and thus sustain the plasma continuously. The applied EM field will have only a slight effect on the energies of the radicals and ions. Consequently, the independent control of the mean ion energy and density - through the use of two sources of energy - is possible. Different types of electromagnetic energy sources exist, such as DC, RF or VHF and microwaves.

Certain RF and microwave plasmas have a high degree of ionization (up to several percent) and are consequently called high density plasmas (HDP)[a]. They also have a high degree of dissociation which can reach 100%. This results in high deposition rates and elevated ion bombardment[b]. Figure 1.7 shows an example of a RF PECVD reactor. The next chapter will give a detailed discussion of electron cyclotron resonance PECVD systems.

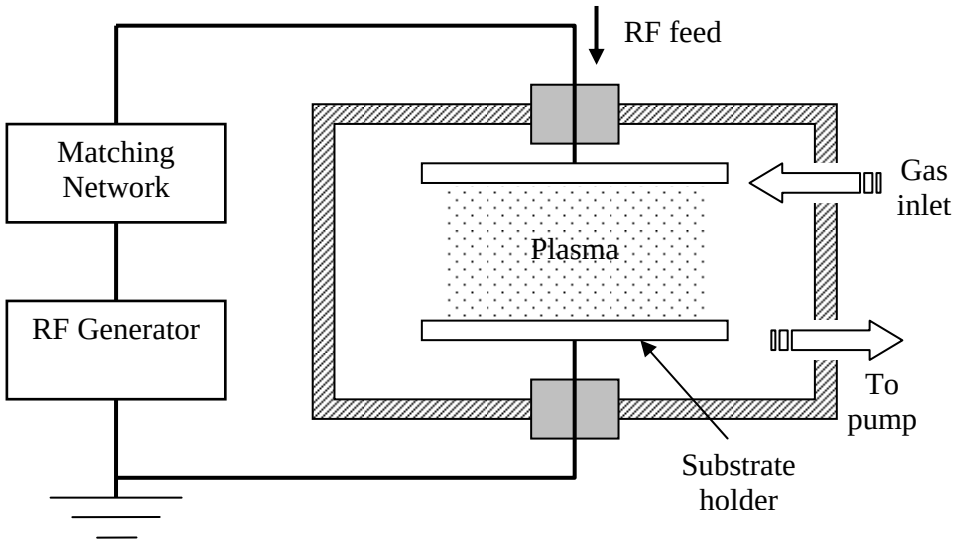

Figure 1.7. A basic RF-PECVD reactor.

[a] In RF plasmas only helicon and inductively coupled plasmas are HDP. Capacitive RF is not.
[b] This may have advantages such as reduced hydrogen incorporation in silicon oxynitride layers.

The working pressure in LF and RF reactors, also called **capacitive reactors**, is between 0.1 and 10 Torr, so the MFP is between 0.5 mm and 5 μm at room temperature[a]. The frequencies used are between 60 Hz and several tens of MHz, but are normally higher than 1 MHz, with generators of 13.56 MHz typically used in CCP RF PECVD reactors. This frequency and its harmonics are reserved for industrial applications and it therefore does not interfere with telecommunication frequencies.

1.3. Range of Materials in PECVD

For the production of optical thin film materials, the method used should ensure the reproducibility of the optical and mechanical properties (§ 1.1) with good uniformity and homogeneity. For the majority of applications, materials should be amorphous, in order to not show birefringence in the absence of external constraints[4]. Certain mechanical properties are also required, such as good adhesion to the substrate, lack of cracking, stability and resistance to changes in environmental conditions.

Through the technique of PECVD, we are usually able to produce materials meeting these requirements. Moreover, this technique allows deposition at higher rates and better packing density (as compared to competing techniques such as evaporation) due to biasing and the contribution of impinging ions. It is also a more suitable technique for the deposition of graded index layers, as it offers continuous deposition of different indices, which is important for rugate filters and waveguides.

Table 1.2 contains a summary of optical materials that can be produced using PECVD systems, taken from literature[4].

[a] These values are calculated from the diameter of the N_2 molecule (d=3.7Å), since the mean free path is given by $\lambda = \frac{1}{\sqrt{2}\pi d^2 n}$ where n is the molecules density calculated from $p = nkT$.

Table 1.2. Optical materials produced by PECVD and their precursors[a].

Material	Precursors	n (550 nm)
a-Si :H	SiH_4	4.0-5.0
SiO_2 :H	SiH_4 / O_2 or N_2O	1.45–1.48
SiO_2 :H:C	Tetraethoxysilane (TEOS)	1.47–1.50
	Hexamethyldisiloxane (HMDSO)	
	Tetramethyldisiloxane (TMDSO)	
SiO_2 :F	SiH_4 / O_2 / CF_4	1.41–1.47
SiO_2 :F:C	TEOS / C_2F_6	
	TEOS / O_2 / CF_4	
	Fluorotriethoxysilane (FTES)	
Al_2O_3	$AlCl_3$ /O_2 or N_2O	1.54–1.62
Al_2O_3 :C:H	Trimethyl-aluminum:$(CH_3)_3Al$ / O_2 or N_2O	1.54–1.64
	Trimethyl-amine alane:$(CH_3)_3$NAlH3 / O2 or N2O	
Si_3N_4 :H	SiH_4 / N_2 or NH_3	1.72–2.04
Si_3N_4 :H:C	Hexamethyldisilazane (HMDSN)	1.75
	Hexamethylcyclotrisilazane (HMCTSZN)	
SiO_xN_y :H	SiH_4 / O_2 /N_2 or SiH_4 /N_2O/NH_3	1.46–2.05
AlO_xN_y	$AlBr_3$ /H_2 /N_2O	1.60–2.10
TiO_2	Titanium tetrachloride: $TiCl_4$ / O_2	2.10–2.45
TiO_2 :C:H	Tetraisopropyltitanate (TIPT): $Ti(OC_3H_7)_4$ / O_2	
	Tetraethoxytitanate (TEOT): $Ti(C_2H_5)_4$ / O_2	
Ta_2O_5	TaF_5 /O_2	2.12–2.16
Ta_2O_5 :H:C	Tantalum pentaethoxide: $Ta(OC_2H_5)_5$ / O_2 or $Ta(OCH_3)_5$ / O_2	
a-C:H	CH_4,C_nH_{2n+2} ,C_nH_{2n} , etc.	1.6–2.20
GeO_2 :H:C	Tetramethylgermanium (TMGe): $Ge(CH_3)_4$ / O_2	1.463–1.477
Y_2O_3-ZrO_2 (YSZ)	Acetylacetonatozirconium: $(C_5H_7O_2)_4Zr$	2.10
	Dipivaloylmethanato yttrium : $(C_{11}H_{19}O_2)_3Y$	

[a] The material properties and conditions of deposition vary with the PECVD technique used. Information pertaining to silicon oxynitrides deposited by ECR-PECVD is given in Chapter 4.

1.4. Control Techniques for Optical Material Deposition

Thin film growth control requires highly sensitive methods of measurement, since the quantity of matter deposited is very small. For optical and semiconductor materials the dynamic measurement of the refractive index and the layer thickness - and therefore its growth rate - is of special interest. It is very important to have precise methods for measuring these parameters, since their accuracy is decisive for the film requirements. The choice of the measurement technique depends on the nature of the sample and the deposition method. The technique should not interfere with the deposition process as this can cause changes to the resulting film properties. Two or more techniques can also be combined in order to have more reliable information. In this study we will describe the principles of the following currently used control techniques:

- Quartz crystal microbalance (QCM).
- Single wavelength and spectral reflectometry.
- Kinetic ellipsometry, which will be detailed in Chapter 4.

1.4.1. Quartz Crystal Microbalance

The QCM technique is used for in-situ thickness or growth rate measurements on a surface near the substrate. It is based on mass measurement, and is achieved by recording the resonance frequency change of a piezoelectric quartz disc [13, 16].

The Sauerbrey relationship gives the resonance frequency decrease Δf with the incremental change in mass Δm of the layer grown:

$$\Delta f = -\frac{2 f_0^{\,2} \Delta m}{A\sqrt{\rho_q \mu_q}} \qquad (1.14)$$

where f_0 is the fundamental frequency of the shear mode of the crystal, A its exposed area to the deposition, ρ_q the quartz density, and μ_q its shear modulus.

Knowing the deposited material density ρ_F and the film area on the quartz A, one can deduce the thickness change, by

$$\Delta d = \frac{\Delta m}{A\rho_F} \qquad (1.15)$$

This technique is widely used in evaporation, but is not suitable for plasma deposition. In evaporation, a scale factor is used to estimate the real thickness deposited on the substrate. It depends on the relative positions of the substrate, the quartz, and the crucible in the vacuum chamber, as well as the angular distribution of the material evaporation. This factor must therefore be characterized using another measurement method. The lifetime of a crystal depends on its minimum oscillation frequency, which is usually between 2 and 4 MHz.

1.4.2. Single Wavelength and Spectral Reflectometry

Single wavelength reflectometry has been used for a long time for monitoring optical layer deposition [6]. This method is very suitable for the control of QWOT multilayer depositions, since the ideal optical thickness of each layer corresponds to an interferometric maximum or minimum at the control wavelength. The technique can be used in either reflectance or transmission mode. Figure 1.8 shows the reflectance profile of a standard three layer antireflection coating on glass for the visible range.

This method can also be used for arbitrary thicknesses by changing the control wavelength for each layer, on the condition of having thicknesses higher than a QWOT of the deposited material for the lowest wavelength allowed by the apparatus.

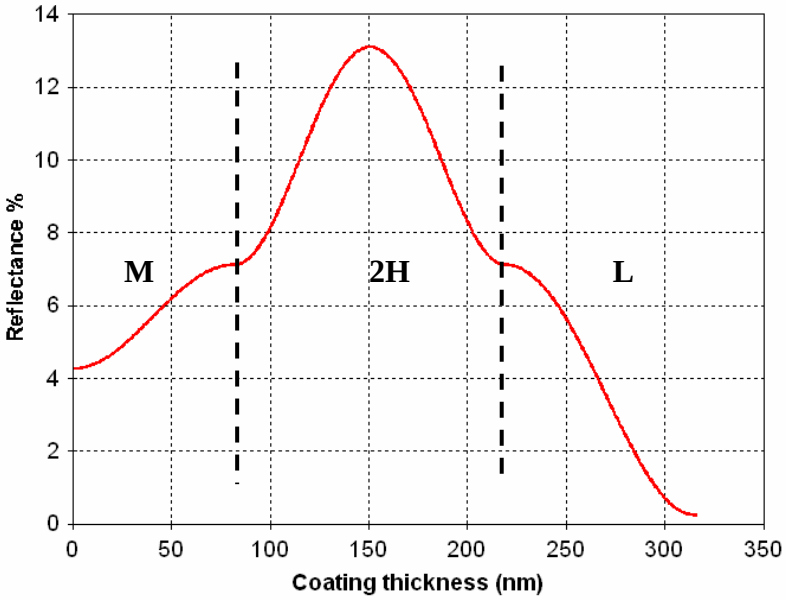

Figure 1.8. Reflectance evolution at 530 nm, for monitoring an M2HL visible ARC.

A newer control method, based on broadband spectroscopic reflectometry, is currently widely applied. It uses an array of photodiodes to do the acquisition at different wavelengths, which permits fast spectroscopic measurements on the order of a few seconds. It consists of the following steps [17-20]:

- Estimating the current layer's deposition time, taking into account the thickness accuracy.
- Stopping the deposition a few percent before the estimated time.
- Taking a wideband measurement of the reflectance or transmission of the deposited layer and calculating the necessary thickness correction.
- Repeating the procedure until reaching the required thickness.

This method is more suitable with deposition systems allowing homogeneous and dense materials, such as magnetron sputtering [21]. It is less accurate with e-beam systems, where porosity needs to be taken into consideration [19].

Kinetic ellipsometry for deposition control will be discussed in Chapters 4 and 5. The advantage of this technique lies in its suitability for all deposition techniques and its fast acquisition rate of less than one second.

References

[1] G.M. Wells (Chairman), *The Application of Metallic Fluoride Reflection Reduction Films to Optical Elements*, Published at Frankford Arsenal, (October 1943).

[2] J.A. Dobrowolski, *Optical properties of films and coatings, in Handbook of Optics*, Vol. I, (M. Bass, E. W. van Stryland, D. R. Williams, and W. L. Wolfe, editors), McGraw-Hill, (1995).

[3] L. Martinu, *Plasma deposition of optical films and coatings: A review*, Journal of Vacuum Science and Technology A, Vol.18 (6), pp. 2619-2645, (2000).

[4] J.A. Dobrowolski, D. Poitras, P. Ma, H. Vakil and M. Acree, *Toward perfect antireflection coatings: numerical investigation*, Applied Optics, Vol. 41(16), pp. 3075-3083, (2002).

[5] S. Furman, A.V.Tikhonravov, *Basics of optics of multilayer systems*, Editions Frontières, Gif-sur-Yvette, (1992).

[6] H.A. Macleod, *Thin Film Optical Filters*, 2nd edition, Macmillan, New York, (1986).

[7] A. Thelen, *Design of Optical interference Coatings*, McGraw-Hill, (1988).

[8] F. Abelès, *Annales de Physique 5*, pp. 596-640, 706-782, (1950).

[9] R. Petit, *Ondes Électromagnétiques en radioélectricité et en optique*, Masson, (1988).

[10] A. Macleod, *Oblique incidence rules*, SVC Winter Bulletin, pp. 22-28, (Feb. 2006).

[11] M.A. Lieberman, A.J. Lichtenberg, *Principles of plasma discharges and materials processing*, 2nd edition, John Wiley & Sons, (2005).

[12] D.M. Dobkin, M.K. Zuraw, D. M. Dobkin, *Principles of chemical vapor deposition*, Kluwer Academic Publishers, (2003).

[13] M. Ohring, *Materials science of thin films*, deposition and structure, 2nd edition, Academic Press, (2002).

[14] F.F. Chen, J.P. Chang, *Lecture notes on principles of plasma processing*, University of California, Los Angeles, (2002).

[15] M. Moisan, J. Pelletier, *Physique des plasmas collisionnels: Application aux décharges hautes fréquences*, EDP Sciences, (2006).

[16] C. Buzea, K. Robbie, *State of the art in thin film thickness and deposition rate monitoring sensors*, Reports on Progress in Physics, Vol. 68(2), pp. 385-409, (2005).

[17] B.T. Sullivan, J.A. Dobrowolski, G. Clarke, T. Akiyama, N. Osborne, M. Ranger, L. Howe, A. Matsumoto, Y. Song and K. Kikuchi, *Manufacture of complex optical multilayer filters using an automated deposition system*, Vacuum, Vol. 51(4), pp.647-654, (1992).

[18] B.T. Sullivan, G. A. Clarke, T. Akiyama, N. Osborne, M. Ranger, J.A. Dobrowolski, L. Howe, A. Matsumoto, Yizhou Song and Kazuo Kikuchi, *High-rate automated deposition system for the manufacture of complex multilayer coatings*, Applied Optics, Vol. 39(1), pp.157-167, (2000).

[19] B.T. Sullivan, J.A. Dobrowolski, *Deposition error compensation for optical multilayer coatings: I. Theoretical description*, Applied Optics, Vol. 31(19), pp.3821-2835, (1992)

[20] B.T. Sullivan, J.A. Dobrowolski, *Deposition error compensation for optical multilayer coatings. II. Experimental results-sputtering system*, Applied Optics, Vol. 32(13), pp. 2351-2360, (1993).

[21] J.A. Dobrowolski, James R. Pekelsky, R. Pelletier, M. Ranger, B.T. Sullivan, A.J. Waldorf, *Practical magnetron sputtering system for the deposition of optical multilayer coatings*, Applied Optics, Vol. 31(19), pp. 3784-3789 (1992).

Chapter 2

High Density Plasma Sources

Microwave excited plasmas are acquiring more and more importance as they can generate high-density plasmas over a large pressure range [1, 2]. In this study, the microwave excited plasma in which we are specifically interested is the Electron Cyclotron Resonance (ECR) discharge that has been adapted from fusion technologies to surface treatment processes such as cleaning, deposition and etching.

ECR plasma sources, together with inductively (also called transformer) coupled and helicon sources, form the pillars on which high density plasma (HDP) PECVD is built. High density plasmas offer several characteristic features, including low pressure operation, large and highly controllable ion fluxes and heterogeneous reaction modes. Several processes benefit from these features, such as etching, plasma immersion ion implantation and surface cleaning, to name a few.

This chapter will begin by giving a brief overview of laboratory plasmas and their properties in Section 2.1, before discussing microwave plasmas and ECR discharges in Section 2.2. Section 2.3 will then focus on the different ECR reactors currently in use. This will serve to explain the choice of a matrix distributed (MD)ECR-PECVD system and provide the necessary background for Chapter 3, where the MDECR-PECVD reactor developped during this study is presented.

2.1. Plasma and Plasma Properties

A plasma can be defined as a gas containing charged and neutral species [3, 4] showing collective behavior. It consists of electrons, positive ions, negative ions, atoms, radicals, molecules and sometimes, in the case of dusty plasmas, atomic clusters with a negative charge. On average plasmas are electrically neutral, since any charge imbalance would create electric fields that would tend to move the charges to eliminate the imbalance. As a result, the combined density of electrons and negative ions will be equal to that of positively charged ions in any given volume of plasma. This property of plasmas is called quasi-neutrality.

Plasmas have two important characteristics making them ideal for thin film processing. Firstly, they are sources of chemically active species, radicals and ions that result from the collision of neutral background gases with electrons which are sufficiently energetic to break their chemical bonds. Substrate surface reactions can thus take place at much lower temperatures than in thermal processing. Secondly, low-pressure plasmas offer the added advantage of a non-collisional sheath, ensuring that the energy of the ions striking the surface can be accurately controlled within a broad range. Energetic ions play a synergetic role in deposition and etching processes and a determining role in sputtering processes.

Plasmas can be described by several important parameters [4-7]. These include:

- The plasma density n_e, which is the concentration of charged species of the same sign.
- The plasma temperature T_e, which is the electron temperature measured in *eV*.
- The degree of ionization, which is the fraction of the original neutral species (atoms and molecules) that have been ionized. Plasmas with a degree of ionization much less than unity are referred to as *weakly ionized* plasmas.
- Other plasma parameters, such as collision frequency, Debye length and plasma frequency, will be discussed later in this chapter.

In order to have ionization, a constant source of energy is required. The loss of both ions and electrons due to recombination and diffusion and/or convection to the walls must be balanced by the rate of ionization. All technological plasmas are initiated and sustained by electric fields, produced by either direct-current (DC) or alternating-current (AC) power supplies. Typical AC frequencies of excitation are 100 kHz in the low frequency range, 13.56 MHz and its harmonics in the RF range and most commonly 2.45 GHz in the microwave region. These plasmas are sometimes correspondingly referred to as *electric*, *gaseous* or *glow* discharges.

2.2. Microwave Discharges and the ECR Effect

2.2.1. The Motion of a Charged Particle in an Electromagnetic Wave

The theoretical study of microwave plasmas is done by solving the equation of motion for an electron in an electromagnetic harmonic field [1, 2, 8]

$$\begin{vmatrix} E\exp(j\omega t) \\ H\exp(j\omega t) \end{vmatrix} \qquad (2.1)$$

It suggests a fluid model of electrons in motion with mean velocity V of the particle and several hypotheses and simplifications:

- The magnetic force of equation *(2.2)* is negligible compared to the electric force.

$$F_M \approx eE \times \frac{V}{c} \qquad (2.2)$$

- No motion of ions, which are heavy compared to the electrons.
- The collision frequency between an electron and heavy particles is given by ν.

The resulting equation of motion is then

$$m_e \frac{dV}{dt} = -eE(t) - m_e V \cdot \nu \qquad (2.3)$$

The first term of the right hand side of the equation (2.3) refers to the electric force, and the second term to the friction force. The mean velocity is thus given by

$$V = -\frac{eE}{m_e}\frac{1}{\nu + j\omega} \qquad (2.4)$$

The solution results in several characteristic definitions, such as the root mean square value of electron displacement:

$$r_{rms} = \frac{eE_{rms}}{m_e\omega(\nu^2+\omega^2)^{1/2}} \qquad (2.5)$$

As this value is small compared to the reactor's dimensions, collisions with the walls can be neglected. The electron-plasma angular frequency is given as:

$$\omega_{pe} = (ne^2 / m_e\varepsilon_0)^{1/2} \qquad (2.6)$$

This value depends only on the electron density. It is used to define the plasma density and identification of the different plasma zone types by comparing it with the electromagnetic field frequency [6].

The Debye length is given by

$$\lambda_D = \left(\frac{k_B T_e}{m_e}\right)^{\frac{1}{2}} \omega_{pe} \approx 743\sqrt{\frac{T_e}{n_e}}(cm) \qquad (2.7)$$

With the electron temperature T_e in Volts. The Debye length depends on the electron temperature and density. It represents the length over which a significant variation of charge density can only be observed, and is used as a characteristic dimension of the plasma and the sheath.

For ECR plasmas the study is very similar, with the exception of two points [1,2]:

- The collision frequency is much lower due to the very low pressure (in the mTorr range) consequently the MFP is much greater and the electrons reach ionization energy with fewer or no elastic collisions.
- We can only neglect the magnetic field linked to the EM wave. The static magnetic field created by the permanent magnets or the magnetic coils cannot be neglected. It creates the cyclotronic motion of the electrons, which will be discussed in the following section.

2.2.2. The Larmor Radius and the ECR Effect

The trajectory of a charged particle in a static magnetic field is determined by the Laplace force[4] :

$$F = q(V \times B) \qquad (2.8)$$

Under a constant magnetic field and in the absence of electric force it will follow a helicoidal trajectory with a constant radius. The Larmor radius is the characteristic of this cyclotronic motion which is the gyration of the charged particle in the magnetic field. In ECR, it is specifically used to describe the motion of electrons.

For an electron in a constant magnetic field, the Larmor radius is given by the formula

$$r_L = \frac{\sqrt{2m_e T}}{eB} = \frac{m_e V_e}{eB} \qquad (2.9)$$

where m_e is the electron mass, T its kinetic energy, V_e its velocity, e the charge of the electron and B the magnetic field strength, as shown in Figure 2.1. The subsequent Larmor angular frequency will then be

$$\omega_L = \frac{eB}{m_e}$$

(2.10)

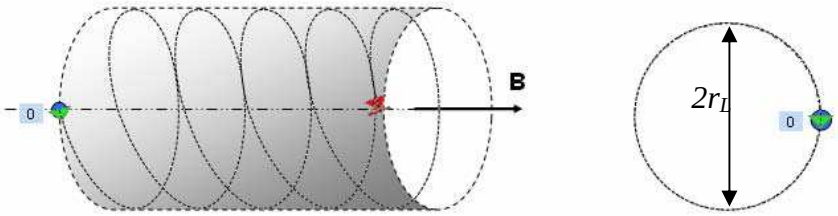

Figure 2.1. Motion of an electron and Larmor radius in a constant magnetic field.

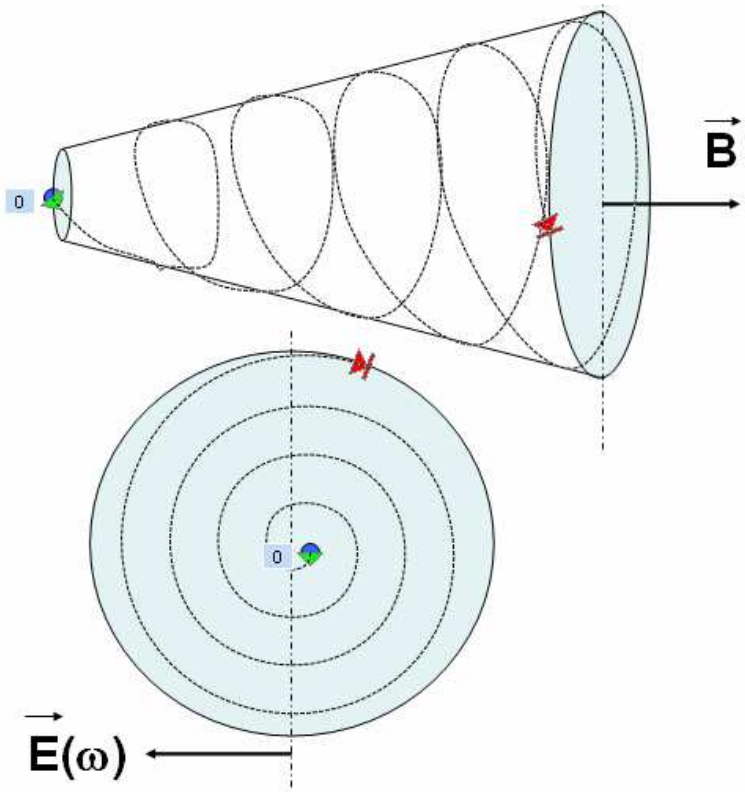

Figure 2.2. Trajectory of an electron under the ECR effect and the resulting increase in the Larmor radius.

When applying microwaves, the alternating electric field (§ 2.2.1) will contribute to this motion. As can be seen in Figure 2.2, resonance will exist when the microwave frequency is equal to the Larmor frequency:

$$\omega_{MW} \approx \omega_L \qquad (2.10)$$

This signifies that the motion of the electron in the field created by the magnets is in harmony with the electric field generated by the microwaves. In the absence of collisions, the electric field constantly increases the electron velocity, and consequently its kinetic energy[a] beyond the ionization threshold required for ionization and the creation of discharges [8, 9]. For a standard microwave power supply operating at 2.45 GHz, ECR will occur in the regions where the magnetic field component perpendicular to the plane of oscillation of the electric field vector is equal to 875 Gauss[b].

Operating at low pressure is an important condition to ensure a sustained ECR effect. Pressures below 10 mTorr are normally used. Higher pressures will increase the collision frequency, which in turn will result in a transition to a collisional microwave plasma [9].

2.3. Low Pressure Microwave Reactors

ECR plasmas have distinct features due to the high ionization and gas dissociation levels at low pressures [9]. The plasma and deposition processes under such conditions depend on several parameters [10], such as the pressure, microwave power, substrate temperature and reactant gas flows. Additionally, the energy and flux of impinging ions depend on these parameters and may additionally be controlled by RF biasing[c]. To apply ECR technology towards thin film fabrication, several different designs of ECR reactors have been developed[11], including divergent ECR, microwave plasma disk reactors, distributed ECR, integrated ECR and multi-dipolar (or matrix distributed) ECR reactors.

[a] Figure 2.2 illustrates this phenomenon. When the radius increases while the gyration frequency is constant, the electron's velocity should increase to make a complete turn for each period.

[b] $\frac{eB}{m_e} = 2\pi \times 2.45 \;\; GHz \;\; \Rightarrow \;\; B \approx 0.08753 \;\; Tesla \approx 875 \;\; G \cdot$

[c] DC biasing can be used in the deposition of conducting materials.

2.3.1. Divergent ECR

Divergent ECR PECVD systems, also referred to as NTT reactors[a], are considered to be the most typical ECR reactors. The microwaves, traveling through a rectangular or circular waveguide, are introduced into the vacuum chamber through a dielectric window [11]. One or several magnetic coils wound around the reactor are used to form a magnetic field with a specific strength and profile. The reactor volume may have from one to several ECR regions. The magnetic field profile along the chamber axis can be adjusted in order to localize the ECR region of the plasma where it is necessary. Figure 2.3 shows an example of such a reactor, taken from the literature [12].

The main disadvantage of these reactors is the radial non-uniformity of the field and thus scaling up beyond 50 cm proves difficult. The deposition of conductive materials such as a-Si on the microwave window may cause the reflection of microwaves and the gradual attenuation of the electric field beyond the dielectric window, while etching can also damage the window [12]. These systems are however the only commercially produced reactors for VLSI technology and used mainly for metal etch applications.

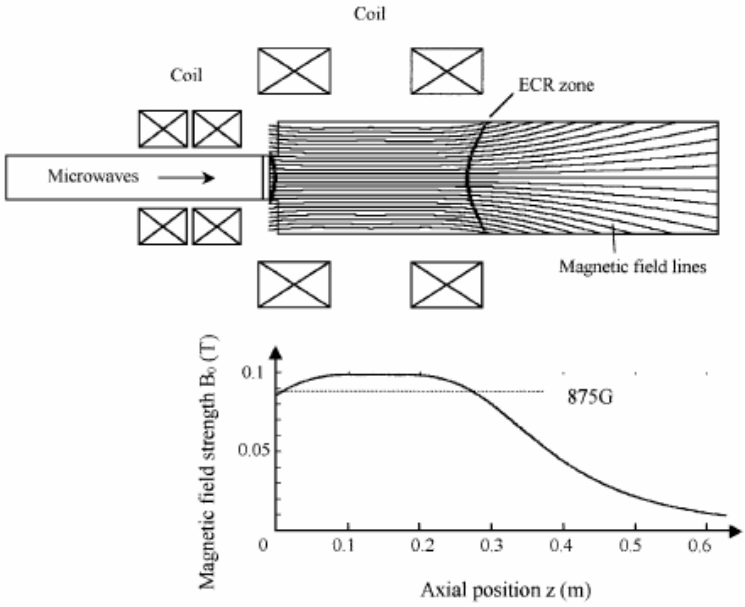

Figure 2.3. Divergent ECR system with resonance locations as modeled in [12].

[a] After Nippon Telephone and Telegraph first demonstrated such a device.

2.3.2. Microwave Plasma Disk Reactors

The microwave plasma disk reactor (MPDR) was developed by Jes Asmussen of Michigan State University [13-17]. It combines multipolar magnetic confinement with a resonant cavity and internal tuning. The microwave mode can be chosen precisely by using such an arrangement, normally excited by a probe antenna. The cavity can be matched over a broad pressure range, from below one mtorr to over 300 torr. Operating as a resonant cavity, an applicator can induce a high strength tangential field against the top of the quartz discharge chamber without reflecting the power from the applicator. Very high powers can thus be coupled into the plasma by an evanescent electric field.

Figure 2.4 shows a commercial MPDR, from which it can be seen that the quartz discharge chamber is a serious drawback, as are the permanent magnets on the chamber's border. Similar to divergent ECR systems, this window is sensitive to damage from etching gases and deposition of conductive layers. Additionally, the rapidly decreasing magnetic field of the permanent magnets will not only expand the ECR zone away from the wafer surface, but will also present a serious problem for scaling up the system due to the increasing radial non-uniformity [17].

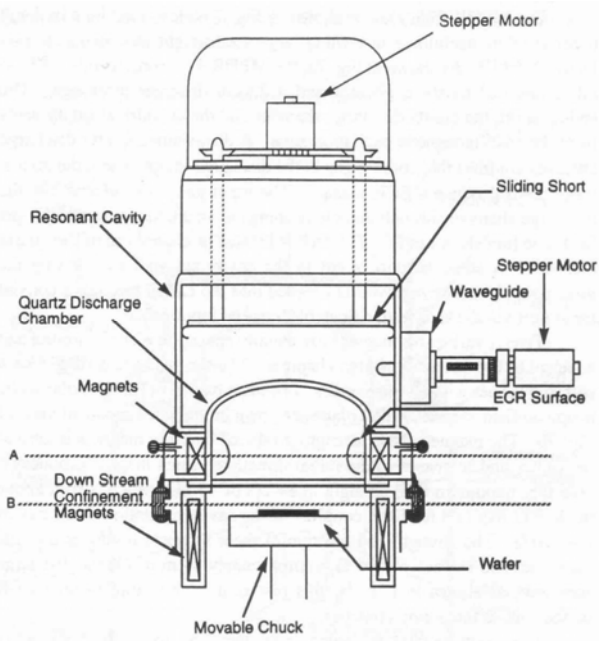

Figure 2.4. Example of a commercial Microwave Plasma Disc Reactor [17].

2.3.3. Distributed ECR

The configuration of the magnets and antennas on the periphery of Distributed ECR reactors, an example of which is presented in Figure 2.5, is suitable for producing a uniform deposition on a large area between the antennas by diffusion of ionized species [18]. A benefit of these reactors is the ease with which the reactor may be scaled up by simply adding extra antennas and magnets, thus enlarging the plasma. The magnets contribute simultaneously to the ECR effect and to the plasma confinement. However, even if the plasma is uniform in the plane perpendicular to the antennas, it is not uniform along the axis, parallel to the antennas, because of attenuation of the microwaves along the applicators. Moreover, with increase of the radius of reactor, plasma density in the center tends to drop.

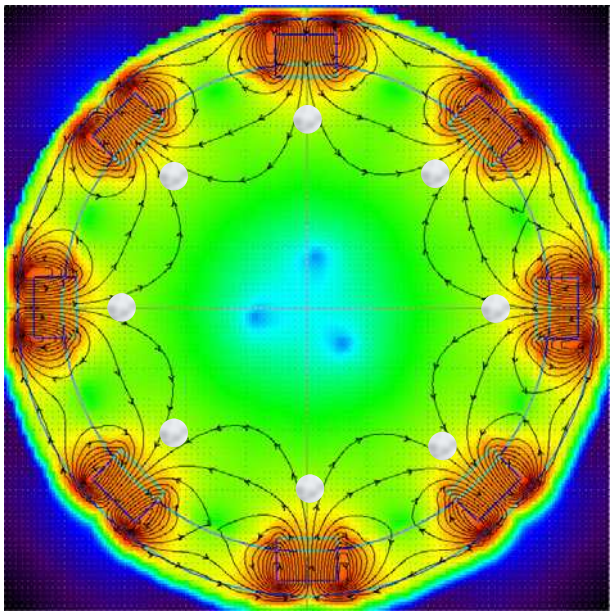

Figure 2.5. Divergent ECR plasma with magnet and antenna positions.

To overcome this problem, a configuration with standing waves with constant quasi-amplitude has been suggested [18]. A considerable reflection on the end of the antennas is consequently needed, therefore a high power supply and the low absorption of microwaves are necessary, which is technically difficult to realize. Moreover, each of the magnet sets and antenna sets need a cooling system. Integrated Distributed ECR, which is discussed next, seems to be a solution for some of these problems.

2.3.4. Integrated Distributed ECR

IDECR reactors allow a single cooling system for all the antennas and perfect proximity of the antennas and the magnets. Figure 2.6 shows the reactor *Plasface*, in the PICM Laboratory. The configuration consists of microwave antennas enveloping long magnets of $SmCo_5$ with alternating polarities facing the substrate [19].

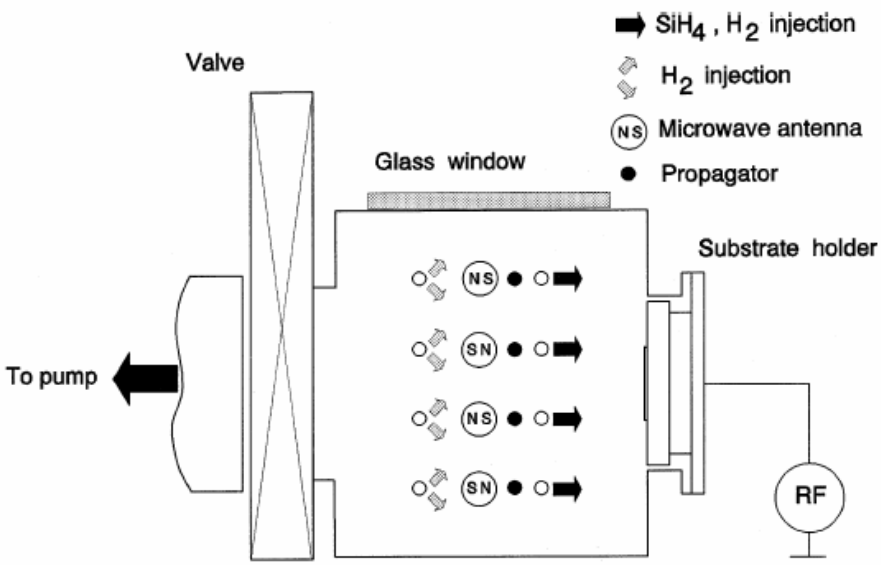

Figure 2.6. The IDECR reactor *Plasface* [19].

Enlargement of the deposition surface consists of increasing the number and the length of the antennas. The problem of microwave propagation and high interaction between the antennas, causing instability are still limiting factors in the scale-up of IDECR reactors. In addition, the lengthening of magnets is not a simple problem to solve.

2.3.5. Matrix Distributed ECR

In order to overcome the technical limitations of DECR and IDECR systems, the MDECR system has been suggested as a logical solution, as it offers some very significant advantages, without any major drawbacks. MDECR[a] systems consist of magnets integrated into the antennas, which are distributed in a matrix configuration [20-22].

Figure 2.7 depicts one row of microwave antennas, with the resulting ECR region around the integrated magnets of each antenna. This configuration combines the advantages of DECR and IDECR - confinement of the plasma as a wall facing the substrate and integration of the magnets and antennas - without propagation interference. It allows deposition on large surfaces, and can be expanded further by increasing the matrix dimensions, in other words the number of antennas.

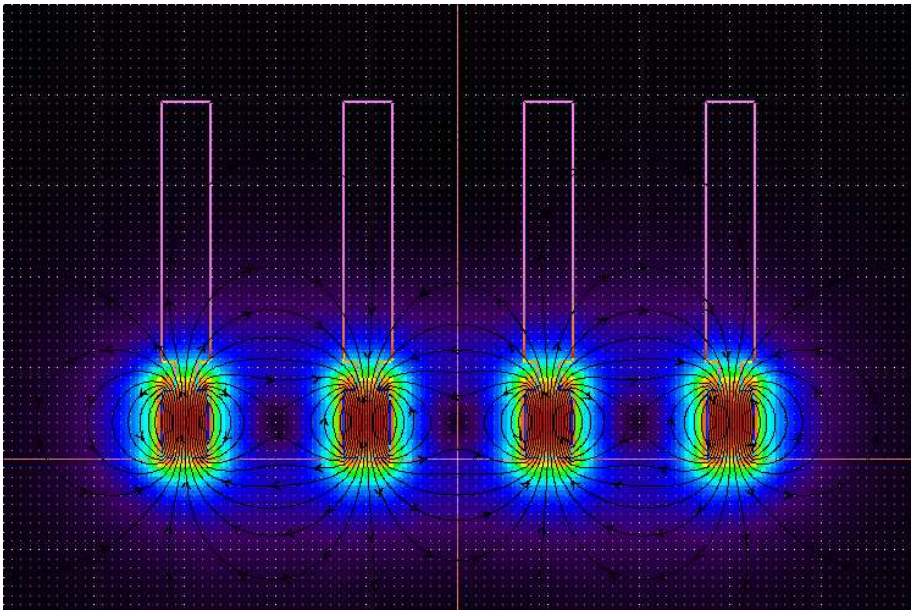

Figure 2.7. MDECR line of antennas with ECR regions.

[a] Matrix Distributed or also called Multi-Dipolar. Multi-Dipolar ECR is usually more general. It can be an extension of DECR to multiple levels of periphery antennas [18], or matrix distribution as in our study.

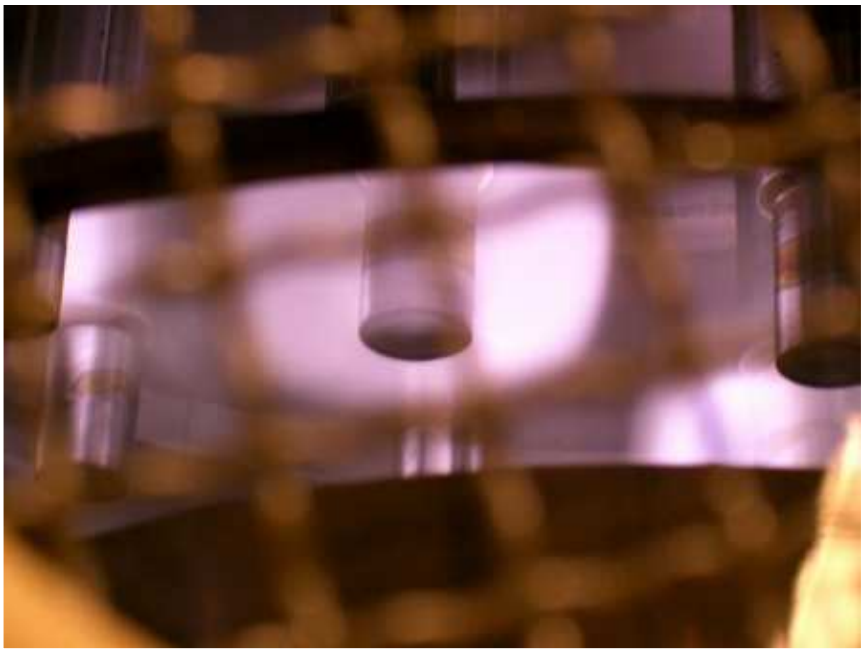

Figure 2.8. ECR zone around an antenna magnet in argon plasma.

An argon plasma in the MDECR-PECVD reactor *Venus* used during this study, with the ECR zone formed around one antenna, is shown in Figure 2.8. Chapter 3 will give further details on the construction and characterization of this reactor.

References

[1] M. Moisan, J. Pelletier, *Microwave Excited Plasmas*, Elsevier Science, (1992).

[2] M. Moisan, J. Pelletier, *Physique des plasmas collisionels: application aux decharges haute fréquence*, EDP Sciences, (2006).

[3] B. Chapman, *Glow discharge processes: Sputtering and plasma etching*, John Wiley & Sons, pp. 49-75, (1980).

[4] F.F. Chen, J.P. Chang, *Lectures notes on principles of plasma processing*, pp. 1-10, Springer, Los Angeles, (2003).

[5] N.St J. Braithwaite, *Introduction to gas discharges*, Plasma Sources Science and Technology, Vol. 9(4), pp. 517 – 527, (2000).

[6] M.A. Lieberman, A. J. Lichtenberg, *Principles of Plasma Discharges and Materials Processing*, 2nd Edition, John Wiley & Sons, pp. 274-283, (2005).

[7] M. Ohring, *Materials Science of Thin Films: Deposition and Structure, 2nd Edition*, Chapter 4, Elsevier Academic Press, (2002).

[8] M.R. Wertheimer, M. Moisan, *Processing of electronic materials by microwave plasma*, Pure and Applied Chemistry, Vol. 66(6), pp. 1343-1352, (1994).

[9] J. Asmussen, *Electron cyclotron resonance microwave discharges for etching and thin-film deposition*, Journal of Vacuum Science and Techology A, Vol. 7(3), pp. 883 - 893, (1989).

[10] P.V. Bulkin, *Electron cyclotron resonance plasma enhanced chemical vapour deposition SiOxNy: Optical properties and applications*, PhD Thesis, Rand Afrikaans University, Johannesburg, South Africa, (1994).

[11] S. Nakayama, *ECR plasma for thin film technology*, Pure and Applied Chemistry, Vol. 62(9), pp. 1751 – 1756, (1990).

[12] H. Muta, *Investigation of Electron Behaviour in ECR Plasmas Using a Self-Consistent Particle Wave Model*, Japanese Journal of Applied Physics, Vol. 38(7B), pp. 4455 – 4459, (1999).

[13] J. Asmussen, M. Dahimene, *The experimental test of a microwave ion beam source in oxygen*, Journal of Vacuum Science and Technology B, Vol. 5(1), pp. 328 - 331, (1987).

[14] J. Hopwood, D.K. Reinhard, J. Asmussen, *Charged particle densities and energy distributions in a multipolar electron cyclotron plasma etching source*, Journal of Vacuum Science and Technology A, Vol. 8(4), pp. 3103 – 3112, (1990).

[15] J. Hopwood, R. Wagner, D.K. Reinhard, J. Asmussen, *Electric fields in a microwave-cavity electron-cyclotron-resonant plasma source*, Journal of Vacuum Science and Technology A, Vol. 8(3), pp. 2904 – 2908, (1990).

[16] P. Mak, G. King, T.A. Grotjohn, J. Asmussen, *Investigation of the influence of electromagnetic excitation on electron cyclotron resonance discharge properties*, Journal of Vacuum Science and Technology A, Vol. 10(4), pp. 1281 – 1287, (1992).

[17] O.A. Popov, *High Denstiy Plasma Sources : Design, Physics and Performance*, pp. 251-311, Noyes Publications, 1995.

[18] S. Béchu, O. Maulat, Y. Arnal, D. Vempaire, A. Lacoste, J. Pelletier, *Multi-dipolar plasmas for plasma-based ion implantation and plasma-based ion implantation and deposition*, Surface and Coatings Technology, Vol. 186(1), pp. 170 – 176, (2004).

[19] P. Bulkin, R. Brenot, B. Drevillon, R. Vanderhaghen, *Structure and transport properties of integrated distributed electron cyclotron resonance grown micro-crystalline silicon*, Journal of Non-Crystalline Solids, Vol. 231, pp. 268 – 272, (1998).

[20] L. Latrasse, A. Lacoste, J. Sirou, J. Pelletier, *High density distributed microwave plasma sources in a matrix configuration: concept, design and performance*, Plasma Sources Science and Technology, Vol. 16(1), pp. 7 -12, (2007).

[21] A. Lacoste, T. Lagarde, S. Béchu, Y. Arnal, J. Pelletier, *Multi-dipolar plasmas for uniform processing: physics, design and performance*, Plasma Sources Science and Technology, Vol. 11, pp. 407 – 412, (2002).

[22] J. Pelletier, T. Lagarde, *Chemical vapour deposition in high-density low-pressure plasmas: reactor scale-up and performance*, Thin Solid Films, Vol. 241, pp. 240 – 246, (1994).

Chapter 3

Implementation of an MDECR-PECVD Reactor: Venus

This chapter will describe the work done to build ***Venus***, the Matrix Distributed (MD) ECR reactor used during all the experiments described in this thesis, shown in Figure 3.1. Section 3.1 will elaborate on the construction of the reactor, development of the necessary control software and first tests. The operation parameters and properties of the plasma are then investigated using various characterization techniques, as described in Section 3.2 and Section 3.3.

Figure 3.1. The reactor Venus during assembly: vacuum chamber with different ports dedicated for characterization and control, the front door and the manual gate valve.

3.1 Description and Construction

The Venus reactor [1], shown schematically in Figure 3.2, is an MDECR reactor designed and installed in the PICM laboratory in the beginning of 2005 and intended for two main applications: the deposition of optical thin films and the encapsulation of organic light-emitting diodes (OLEDs).

It consists of a 70 liter cylindrical stainless steel chamber with an internal diameter of 40 cm. The chamber is equipped with a plasma source at the top, a manual gate valve at the bottom separating the reactor from the turbo-molecular pump, a front loading door and several vacuum, optical and electrical ports for vacuum gauges, plasma and deposition characterization and control. Two special optical ports, inclined at approximately 70º from the vertical, are used for ellipsometric measurements and control with an *in-situ* photo-elastic modulator ellipsometer (PME).

The pumping system consists of a 60 m^3/hour primary rotary vane pump and a 1600 l/sec Alcatel ATP 1600 turbo molecular pump. The pump is close-coupled to the chamber, which allows maximal conductance and permits an optimal pumping speed and a higher flow at lower pressure during the deposition. A Penning gauge is used for base pressure monitoring, while an MKS capacitance manometer with a 0.01 to 100 mTorr pressure range is dedicated to process pressure control and connected to the computer via an RS232 interface.

The aluminum substrate holder is placed horizontally and has a diameter of 22 cm to hold a 200 mm wafer. It can be heated up to 200°C using a resistive heater immersed in AlN ceramic (Shapal) and biased by a 500 Watt, 13.56 MHz RF generator. Two K-type thermocouples are used to monitor the temperature of the substrate holder to prevent overheating. The plane of the sample can be adjusted using three support screws in order to perform optical alignment of the ellipsometer.

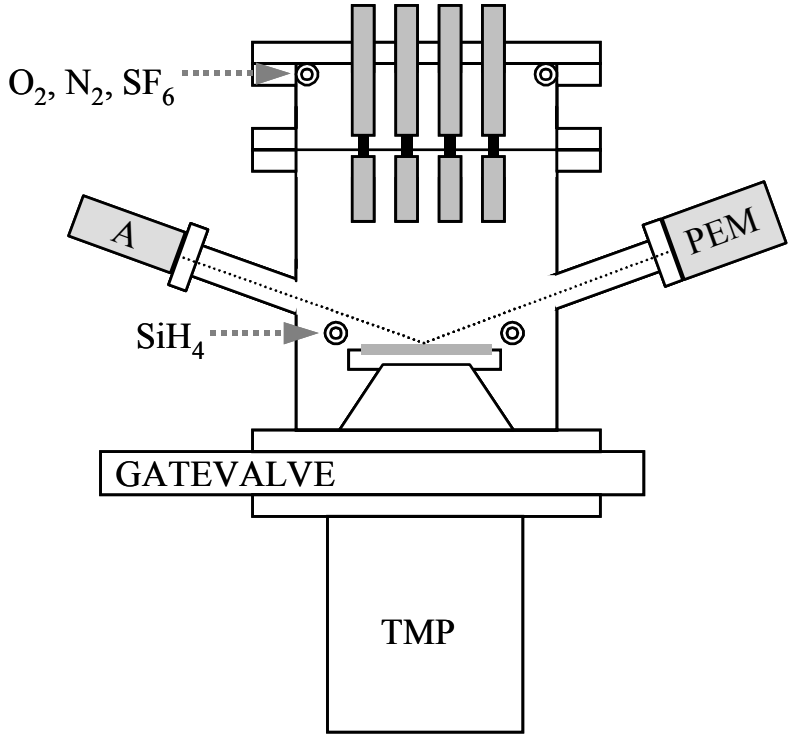

Figure 3.2. Schematic of the Venus reactor.

The microwave discharge at 2.45 GHz is sustained by a set of sixteen water-cooled linear antennas arranged in a 4x4 matrix, each carrying on its end a permanent $SmCo_5$ magnet. Figure 3.3 shows a schematic representation of an antenna [2, 3]. Two magnetrons generating up to 2000 Watts each are used to supply power to the microwave antennas, each one supplying eight antennas via a circulator and an 8-way waveguide-coaxial splitter, as shown in Figure 3.4. Each antenna is connected by a coaxial cable through a coaxial circulator with a dummy load, to minimize the influence of a mismatch on the splitting accuracy. The impedance of each antenna can be manually adjusted using a coaxial impedance matching device.

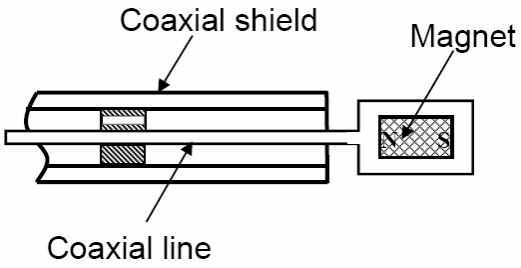

Figure 3.3. Schematic of an antenna used in the Venus reactor.

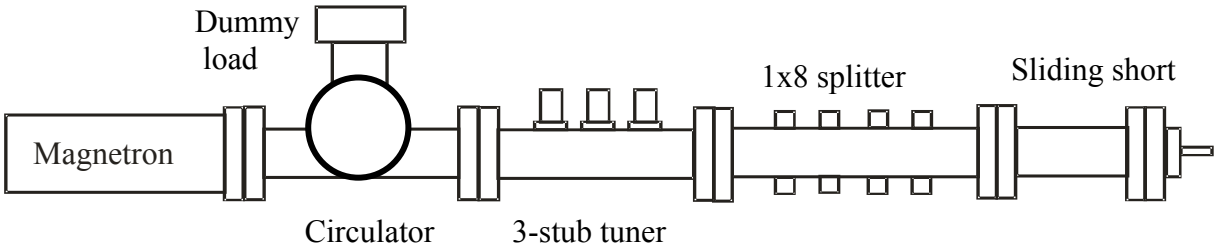

Figure 3.4. The waveguide section of the microwave system.

The injection of precursor gases is done at two levels: oxidant gases (N_2 and O_2), etch-clean gases (SF_6/O_2 mixture) and argon are injected at the top of the reactor above the level of the magnets, where the most intense ECR regions are located. The silane is injected downwards through a circular ring just above the level of substrate (see Fig. 3.2). Figure 3.5 shows the reactor after completion.

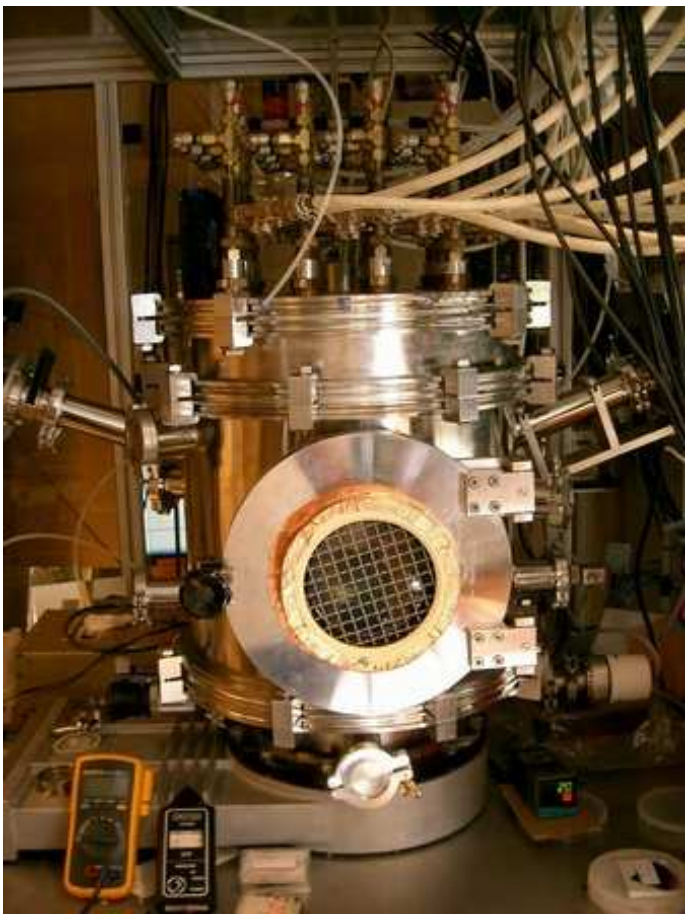

Figure 3.5. *Venus* after construction, showing the loading door in front, the attached ellipsometer on the sides, the microwave antennas and coaxial cables on top.

3.1.1. The Gas Panel, Mass Flow Controllers and Computer Control

As mentioned above, the oxidant gases are supplied into the top flange of the reactor and are injected radially towards the reactor's center through multiple orifices equally spaced on the interior of the flange. The large conductance of the circular channel in the flange, together with the low conductance of the orifices, ensure equal flow through each orifice [4].

The pyrophoric gases are injected below the ECR antennas through a gas distribution ring which, similar to the injection configuration for the oxidants, supplies a radially uniform flow towards the substrate. Gas lines used during computer-controlled deposition are each equipped with a digital MFC, marked with a D in Figure 3.6. The argon, SF_6/O_2 and methane lines have standard analog MFCs. The electro-pneumatic valves are also computer controlled.

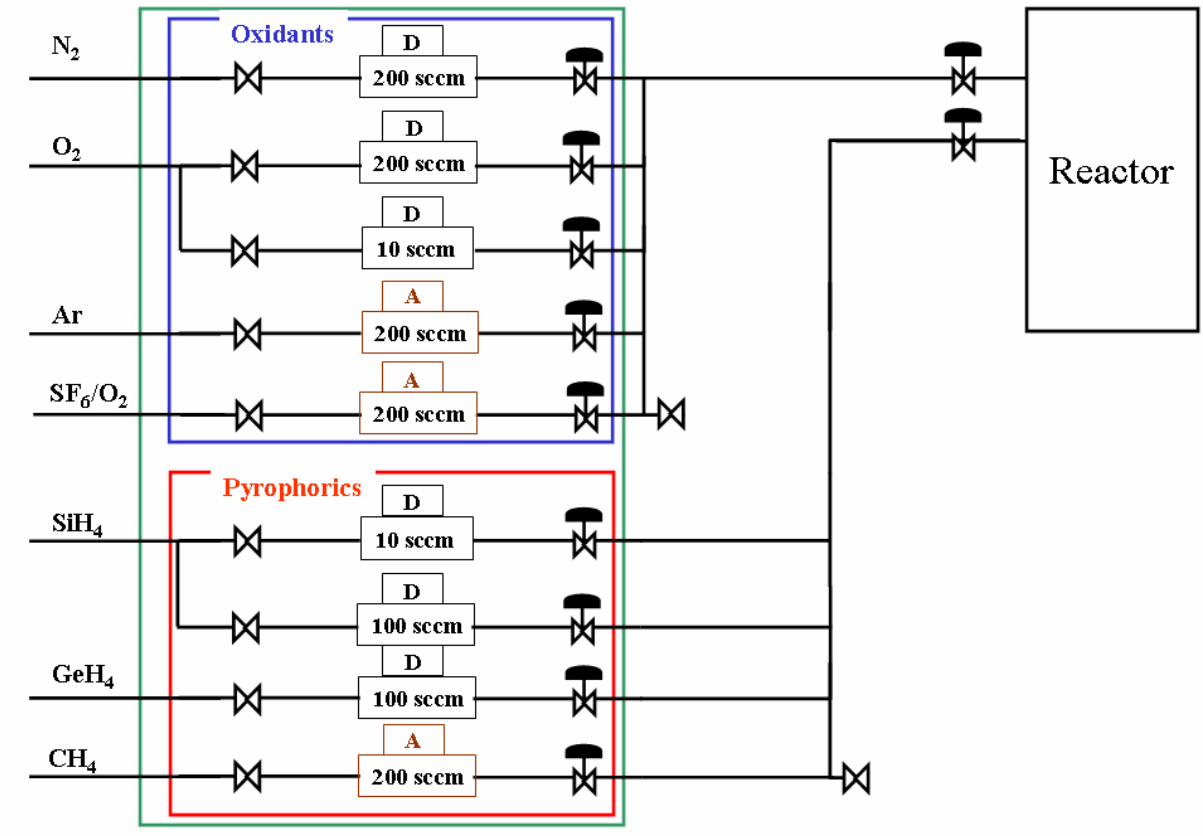

Figure 3.6. Gas distribution system of the reactor.

As the software for the control of the deposition system was written in-house by the author, its structure needs rather detailed explanation. For deposition control two computers connected via a TCP/IP link are used. One is an *Intel Celeron 466 MHz* PC, running the dedicated ellipsometric server and *Microsoft Windows NT4*. The second one is used for gas flow, vacuum and microwave control, as well as intensive calculations for real-time ellipsometric control. Consequently, it is a *Pentium 4* 3 GHz workstation running *Microsoft Windows XP*.

The gas panel consists of two parts, namely the valves and the MFCs, controlled from the *Windows XP* workstation. The valves are programmed via a Profibus card by *Isagraph Workbench* software and are connected by a *Kassl inc.* OPC[a] client-server to the *Delphi* environment. The management of gas flows is done by mass flow controllers (by *STEC / Horiba Group*), which are controlled via a DNet card connected to the *Delphi* environment by the same OPC client. Figure 3.7 shows the hierarchy of the program for the automation process.

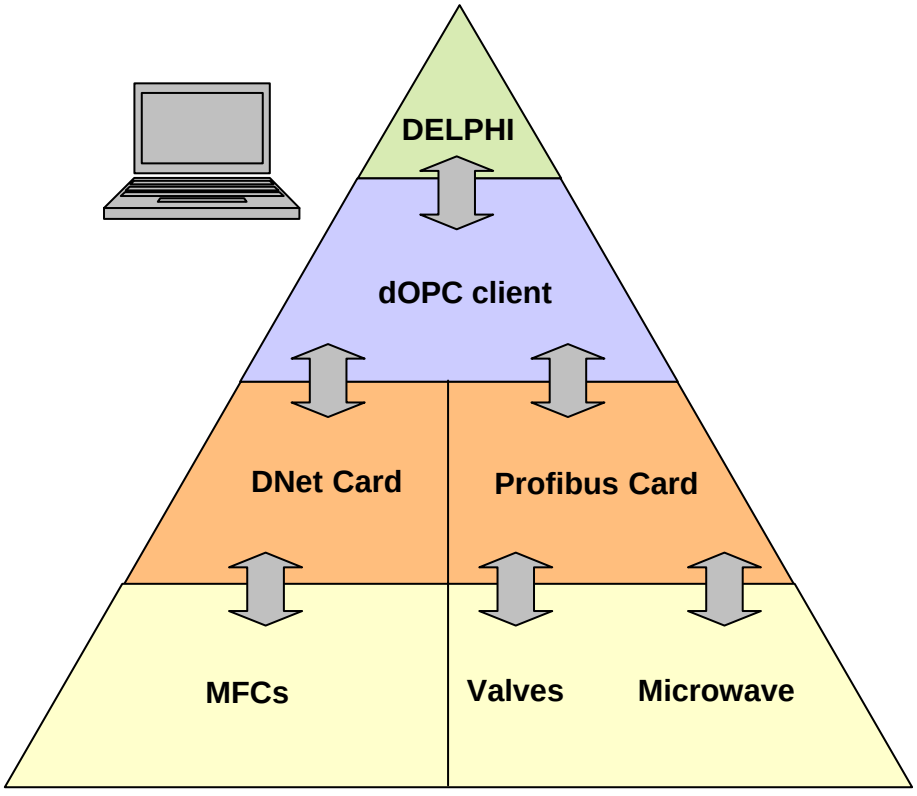

Figure 3.7. The structure of automation of the gas panel on the reactor.

[a] OPC is the abbreviation of OLE (Object Linking and Embedding) for Process Control. It is now an industrial standard for automation.

After programming these procedures, the response time of the MFCs was measured, to verify the possibility of fast transition between different deposited layers and the feasibility of future real-time control which requires rapid feedback on the order of a second, as will be discussed in Chapter 5. Figure 3.8 shows an acceptable response time of between 200 and 250 milliseconds for the two main cases of flow changes: (a) zero to maximal flow transition and (b) a 1 sccm change. In the first case, it takes 0.5 seconds to reach 98% of the required flow, with the delay due to the start from zero. It is thus recommended during fast deposition processes to avoid setting the flow to zero.

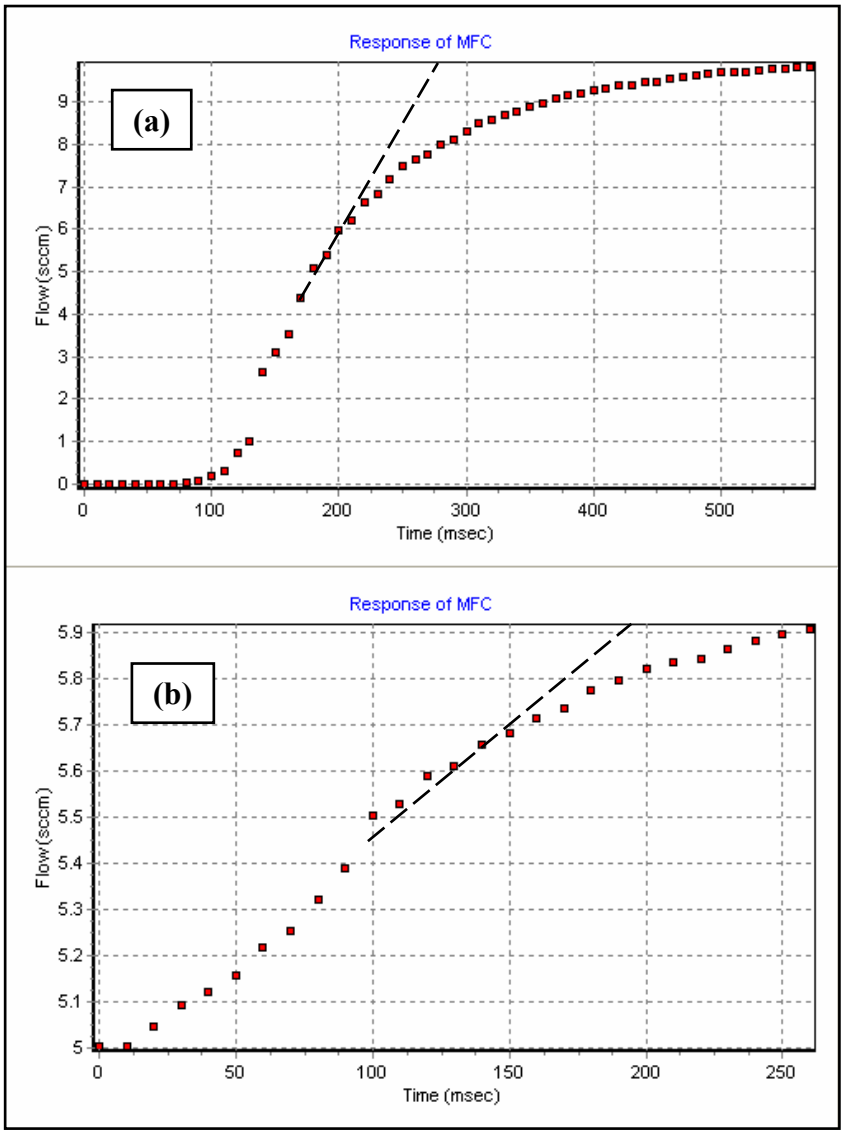

Figure 3.8. MFCs' response time for transitions: (a) zero to maximal flow (b) one sccm.

Figure 3.9 shows the interface developed for management of the MFCs. They can be controlled either by direct manual change on the interface or through a flow versus time definition file in two different ways, as can be seen in Figure 3.10. This provides the ability to program the automatic deposition of a multilayer stack or a gradient index layer, respectively. Forced manual control of the gases while using programmed files is permitted for practical and security reasons.

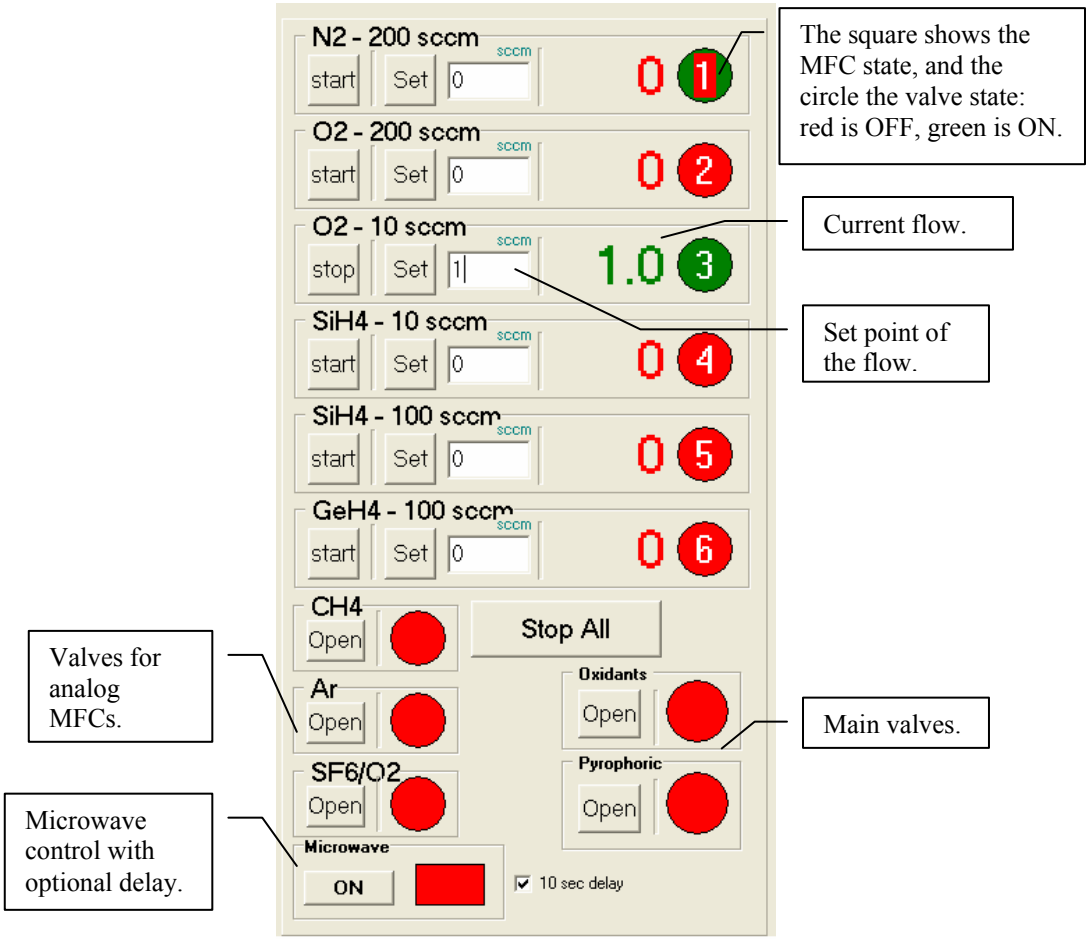

Figure 3.9. Manual control panel of gas flows, valves and microwaves.

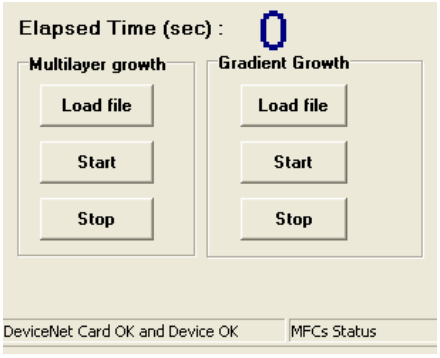

Figure 3.10. Loading of predefined gas flow files with the MFCs and DNET card status.

3.2. Characterization of the Vacuum System and Process Parameter Range

3.2.1. Calculation of the Leak Rate and Residence Time

The main vacuum characteristics of the system are the leak rate R_L, the pumping speed, S and the gas residence time, T [5, 6]. Leak rate evaluation helps in leak detection, which is very important as it allows the user to prevent the presence of undesirable gases inside the chamber and it permits the optimal use of the pumps and gauges. It can be defined as follows in Torr·liter/sec:

$$R_L = V_R \frac{dp}{dt} \qquad (3.1)$$

Where V_R is the volume of the reactor, p is the pressure and t the time. Figure 3.11 shows the leak rate measurements taken, with a total leak rate of less than $5x10^{-4}$ sccm, which guarantees the absence of unwanted impurities. The rise during the first few minutes of the measurement is due to the initial outgasing of the walls. With time, the rise in pressure slows down and the leak rate stabilizes at its real value.

The leak rate defines the ultimate pressure that can be reached inside the reactor:

$$R_L = S \times p_U \qquad (3.2)$$

where the pumping speed S depends on the conductance of the connection to the pump. The same relationship can be used for different flows and pressures to measure the pumping speed, and to deduce from it the residence time T, defined by:

$$T = \frac{V_R}{S} \qquad (3.3)$$

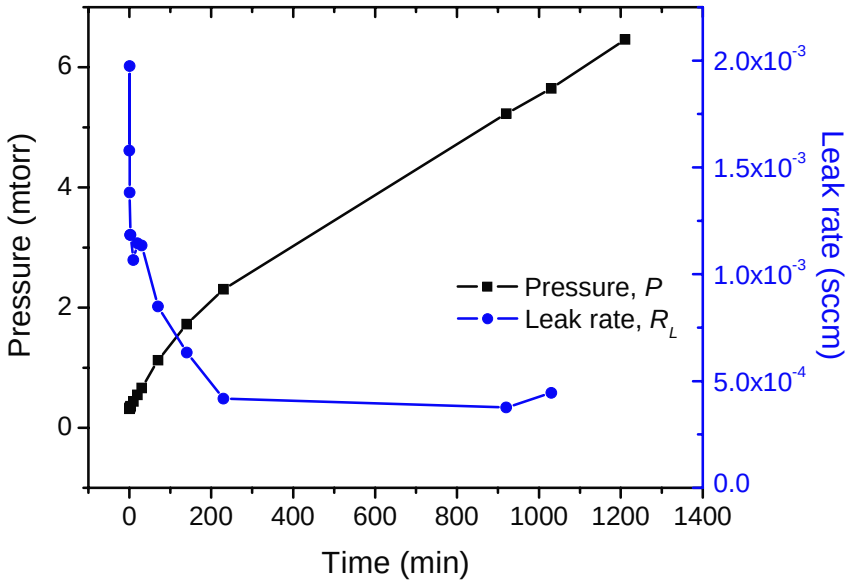

Figure 3.11. Leak rate and pressure increase without pumping.

Figures 3.12 and 3.13 show a residence time of about 60 to 80 milliseconds for argon and oxygen, respectively. The valve was fully opened during these measurements. The lighter the gas is, the slower the pumping rate will be. This is due to a higher thermal speed of the lighter molecules and thus a lower compression ratio of the turbo molecular pump. Consequently, there is an increase in the residence time. The ratio is close to the molecular mass ratios (~ 40 for Ar versus 32 for O_2). When the valve is minimally open the residence time is approximately 20 times greater (about 1 sec) and the base pressure is higher.

It is thus better to use the valve well open and pump at maximal pumping speed when real-time control is required, since changes in the gas flows need to be observed immediately on the substrate surface, within a fraction of a second.

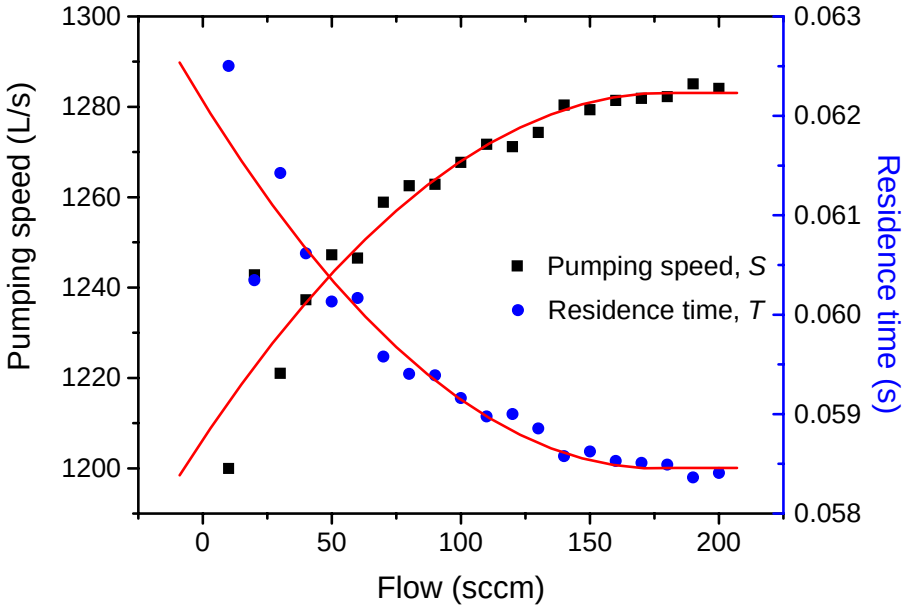

Figure 3.12. Residence time and pumping speed of argon for a fully opened valve.

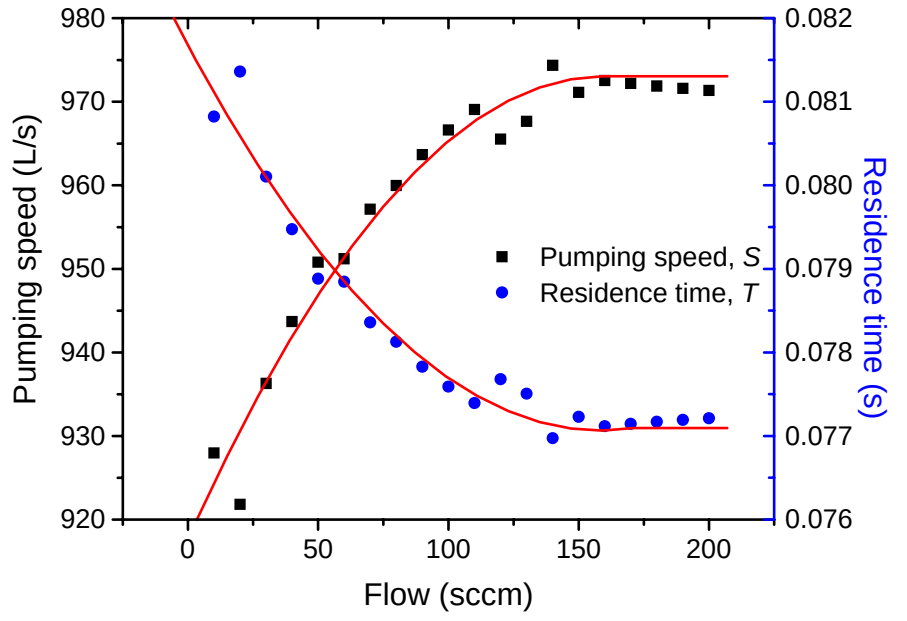

Figure 3.13. Residence time and pumping speed of oxygen for a fully opened valve.

3.2.2. Radio Frequency Biasing of the Substrate

An Advanced Energy 13.56 MHz RF generator with maximal power of 500 Watts was connected to the substrate holder via a matching unit. This allows independent control over the energy of ions impinging on the substrate surface. Figure 3.14 depicts bias voltage values high enough to ensure densification of grown films.

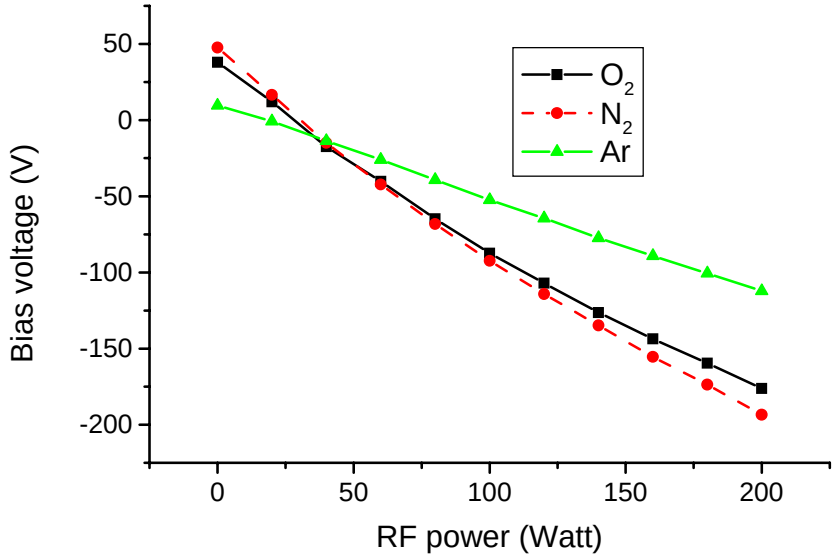

Figure 3.14. Self-bias voltage with increased power for different gases.

3.3. Characterization of the ECR Plasma by Optical Emission Spectroscopy

Optical emission spectroscopy (OES), which consists of the spectral analysis of the light issued from a plasma, is a non-intrusive and relatively straightforward method for monitoring plasma processes [7-9]. It enables the user to have a good understanding of the active species in the plasma, both qualitatively, in other words by the identification of emission lines from an electronic excited state of the precursors and quantitatively, where actinometry with a noble tracer gas is used. The emission must however be due to excitation from the ground state.

By adding small amounts of a known concentration of an inert tracer gas such as argon, the density of a radical, n_A can be obtained. If we consider an excited state T^* of the tracer T with an excitation threshold that closely matches that of the radical being investigated, the cross sections for photon emission of wavelength λ for radical A and λ' for tracer T, will have a small overlap with the electron energy distribution function (EEDF), as shown in Figure 3.15. We can then approximate these cross sections with values near the threshold [7]:

$$\sigma_{\lambda' T} \approx C_{\lambda' T}(v - v_{thr}) \tag{3.4}$$

$$\sigma_{\lambda A} \approx C_{\lambda A}(v - v_{thr}) \tag{3.5}$$

With $C_{\lambda' T}$ and $C_{\lambda A}$ being proportionality constants. The ratio of these equations gives:

$$n_A = C_{AT} n_T \frac{I_\lambda}{I_{\lambda'}} \tag{3.6}$$

Even if C_{AT} is unknown, we are able to see how changing the discharge parameters influences the radical's density. Typically, an argon flow of less than 5 % of the gas mixture is used in order not to influence the plasma emission. An *Ocean Optics USB-4000* spectrometer with a spectral range between 200 and 850 nm and an optical resolution of 2 nm, was used. Measurements were taken at both the level of the antennas and the substrate holder, as shown in Figure 3.16. A variety of plasma parameters, such as microwave power, gas flow, RF biasing of the substrate holder and pressure were investigated.

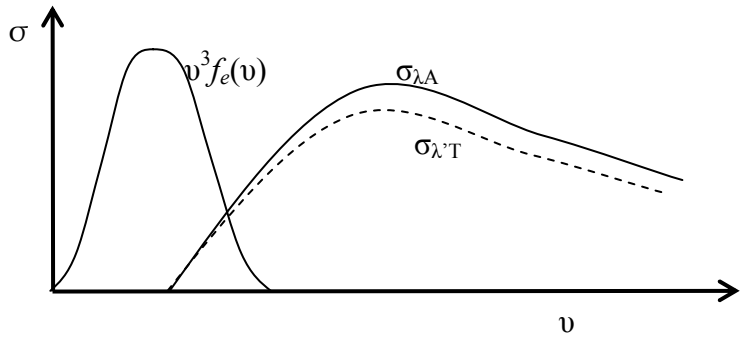

Figure 3.15. Overlap of the emission cross sections and the EEDF.

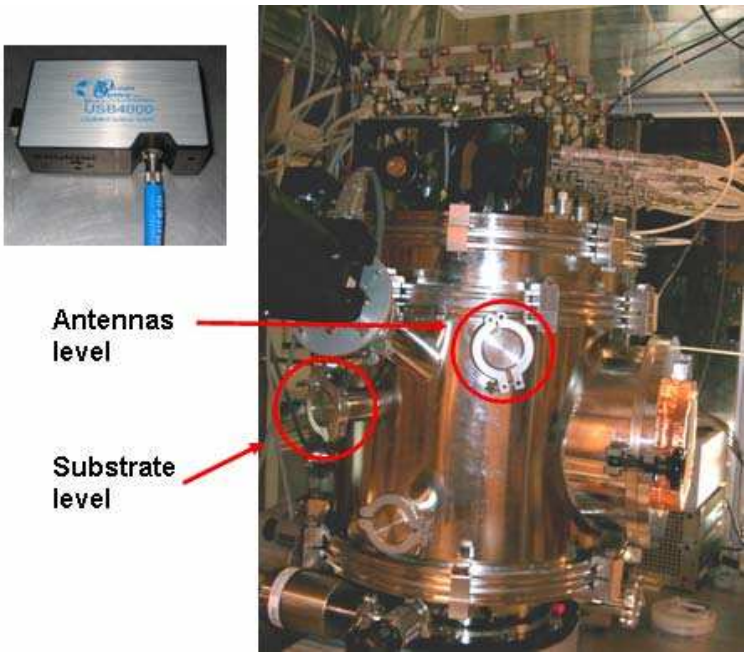

Figure 3.16. Optical ports used for OES measurements on the Venus reactor.

Table 3.1 gives a list of emission lines generally used in literature during characterization of the optical emission of ECR plasmas [10-12]. The precursor gases used were silane, oxygen and argon as actinometer gas. As mentioned previously, the excitation threshold energy of the emission lines for the tracer gas and the specie being investigated, must be similar. The emission lines shown in Table 3.1 satisfy this condition, with the shown argon having a threshold energy of 13.47 eV[7,13], the atomic oxygen emission line at 844 nm having a threshold energy of 10.98 eV[14] and the H_α threshold energy being 12.06 eV[13]. The hydroxyl system between 306.1 nm and 330 nm has also been used extensively in literature with the 750.4 nm Ar emission line[15,16].

Table 3.1. Studied emission lines for SiH_4, O_2 and Ar plasma.

Species	O*	Ar	Hα	OH
Wavelength (nm)	844	750.4	656.6	306.4 system

Figure 3.17 depicts a silica deposition plasma's optical emission spectrum, consisting of 5 sccm SiH_4, 40 sccm O_2 and 3 sccm Ar. The optical emission spectrum for a 5 sccm SiH_4, 80 sccm N_2 and 5 sccm Ar plasma can be seen in Figure 3.18. As discussed earlier, the optical resolution of the spectrometer is not sufficient to identify the 750.4 nm Ar emission line. Due to the vast amount of excited states of nitrogen, as shown in Figure 3.18 and the spectrometer's low resolution, the discussion will focus on plasmas without nitrogen.

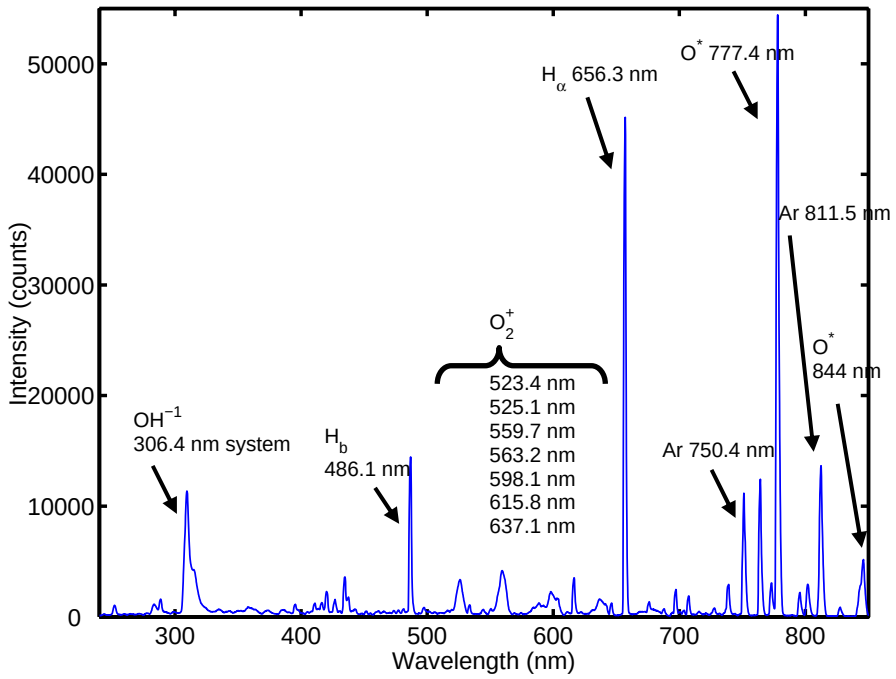

Figure 3.17. Optical emission spectra for a SiO_2 deposition plasma.

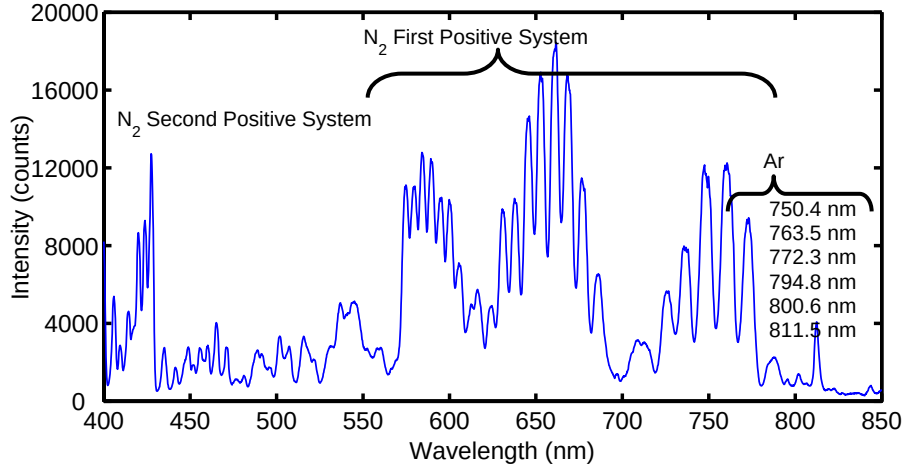

Figure 3.18. Optical emission spectra for a SiN_x deposition plasma.

3.3.1 Influence of SiH_4 Flow

Measurements of the plasma were taken at a constant pressure of 1.5 mTorr, with a fixed oxygen flow rate of 40 sccm and varying silane flow, as shown in Figure 3.19. The argon flow was also kept constant at 3 sccm. As can be expected, the intensity of the hydrogen Balmer line at 656 nm increased linearly with increased silane flow, as atomic hydrogen is a product of the primary dissociation of the silane molecule[17, 18]. The dissociation of oxygen, however, is not influenced and remains constant. The OH signal is also increasing, since water is the main reaction product of the SiH_4 and O_2 reaction. We conclude that the increased amount of silane is dissociated without influencing the oxidant dissociation, since the pressure was kept constant and hence also the mean free path.

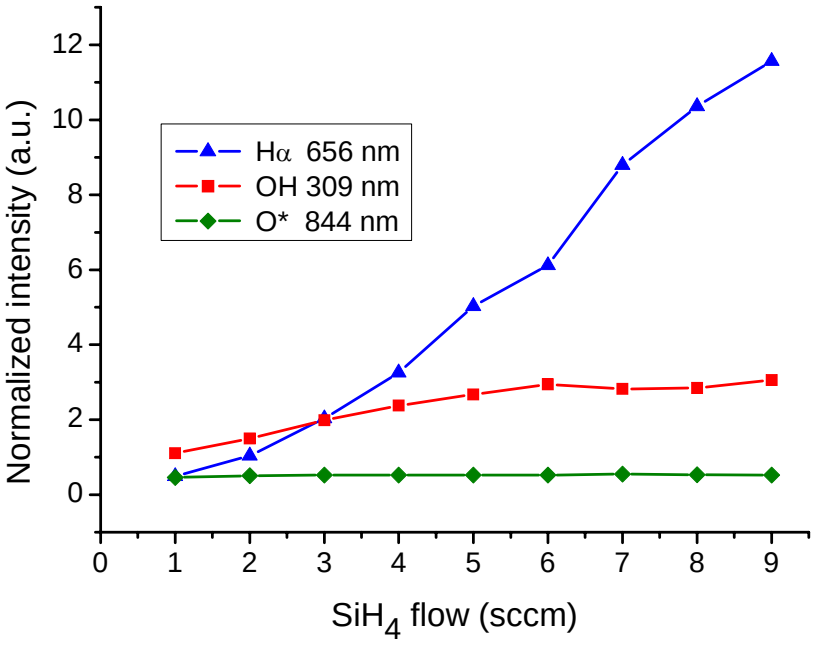

Figure 3.19. Optical emission intensities for H_α, O^* and OH spectral lines taken at various SiH_4 gas flows.

3.3.2 Influence of Increased Microwave Power

Figure 3.20 (a) shows OES measurements taken while varying microwave power, with the gas flows kept constant at 40 sccm of O_2, 5 sccm of SiH_4 and 3 sccm of Ar. The increase in H_α and in OH emissions can be explained by the dissociation of both water and silane [10]. No increase in the atomic oxygen emission was observed.

In order to further investigate this phenomenon, we did separate OES measurements on an oxygen plasma with various microwave power settings. Figure 3.20 (b) shows that in the absence of silane, atomic oxygen emission increases with microwave power, which demonstrates a higher dissociation of the oxygen [7, 11]. With silane, the atomic oxygen can be consumed in the silica growth by highly reactive silicon containing radicals, which may explain the difference in behavior between the two cases.

For a more precise explanation of this phenomenon we suggest doing QMS (quadrupole mass spectroscopy) measurements in the future and comparing the results with the OES data in order to find any correlation.

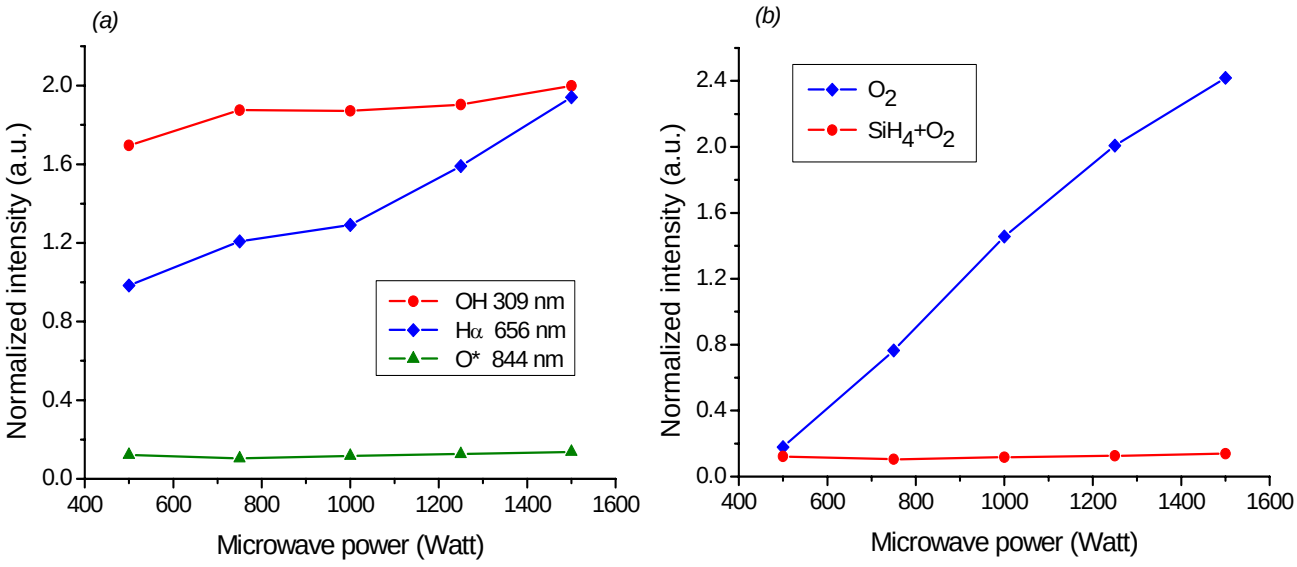

Figure 3.20. (a) Optical emission intensities taken at various microwave powers for SiH_4/O_2 plasma and (b) A comparison of the 844 nm O* emission line of an O_2 and a SiH_4/O_2 plasma.

3.3.3 Influence of Biasing the Substrate

The final process parameter to be investigated with OES is RF biasing of the substrate. OES spectra were taken at two levels: in the antennas plane and in the substrate plane. Whereas none of the emission intensities changed at the antenna level, the OH line marked increase when observed in the substrate plane.

Figure 3.21 depicts the influence of increasing the RF substrate bias on the OH^-, H_α and O^* concentrations, as viewed close to the substrate. As the ion flux increases in energy, the hydroxyl emission also increases, indicating a more and more efficient removal of water from the substrate surface. There will consequently also be a lower water incorporation into the growing film. The fact that the OH emission in the antenna plane did not show this increase is due to the vast difference in surface area of the biased and grounded surfaces of the reactor and hence little or no increase in the ion flux energy directed towards walls. This may serve as a proof of the efficient removal of water from growing films by applying a bias to the substrate holder.

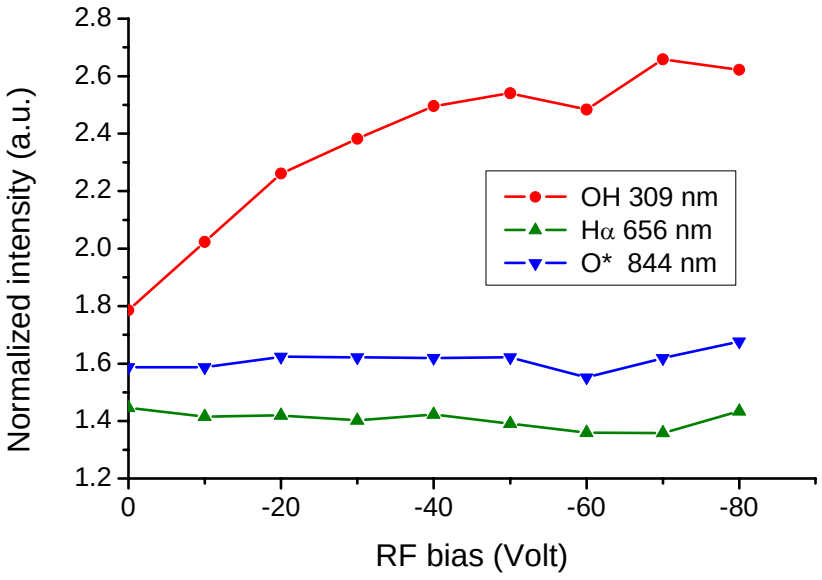

Figure 3.21. OES intensities taken at various RF bias voltages on the substrate level.

3.4. Nature of the Deposition Process in HDP-PECVD Reactor: Implications for Silica Deposition.

A lot of work has been done on the deposition of silicon based dielectrics and especially SiO_2 from oxygen or nitrous oxide and silane mixtures, however most of them used diluted silane, either in noble gases such as Ar and He or in H_2. Dilutions as low as 0.1 per cent were reported in the literature [19].

While it is obviously simpler and safer to work with highly diluted silane, industrial applications require the deposition rate to be as high as possible, while simultaneously preserving the good electrical and optical qualities of silica. Applications such as planar optical waveguide fabrication or scratch-resistant coatings on plastics demand growth rates exceeding 3-5 nm per second. Simple calculation of the flow rates necessary for depositing 10 nm of compact silica per second gives flows in the order of 0.05 sccm/cm^2 which translates into 35 sccm of undiluted silane for the deposition of SiO_2 on a 300 mm diameter wafer and consequently proportionally larger for diluted gas. This minimal amount will scale linearly with an increase in deposition area. Given the fact that the low limit of oxygen flux onto the surface for stoichiometric material deposition has to be about twice that of the silane, the pumping system required in such case of diluted silane is practically unrealistic, as far as low pressures typical for high density PECVD are concerned.

The current paradigm for the deposition process in low pressure, high-density plasma systems (ECR, TCP, ICP or helicon sources) is that the reactor can be considered in the frame of a model of a *well-mixed reactor* [20, 21]. That assumes that the deposition process is the same (except for temperature) on all surfaces of the reactor. This notion is based on the very large mean free path for high-density low-pressure plasmas of the order of several centimeters and assumption that species are not consumed at the moment they touch the surface. It will lead to equal fluxes onto all the surfaces of the reactor for any given species. However, while it is true for the noble gases, nitrogen and oxygen, for example, this is not the case for silane whose products of dissociation have very high sticking coefficients even in non-oxidizing atmosphere, approximately in the order of the unity for SiH and Si.

In the presence of oxygen, the ions and radicals, even usually low and moderately sticking such as SiH_3 and SiH_2, will be immediately oxidized on the surface of the substrate and included into the growing film. This means that flows on all the surfaces of the reactor are not at all the same for all the species. In fact, low pressure in this case prevents redistribution of the fluxes and leads to more or less ballistic (or beam-like) transport of the silicon precursors. All of this has a profound impact on the optimization of SiO_2 deposition from a silane plasma. Two experiments were done in order to confirm this point of view. Their principle is explained in Figures 3.22 where the arrangement of samples for testing the growth rate at different positions in the reactor are shown and Figure 3.23 where the gas distribution ring was replaced by a capillary through which silane was injected towards the substrate. The nozzle is positioned at a distance of 3 cm from the wafer surface and inclined at about 45 degrees.

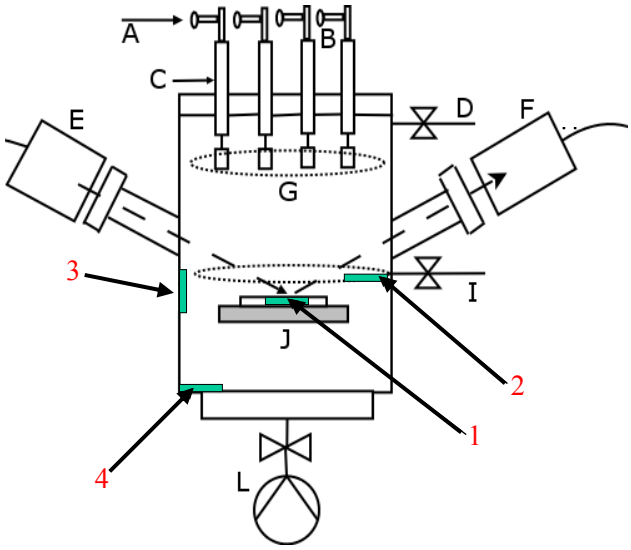

Figure 3.22. Sample arrangement for testing growth rate at different positions in the reactor.

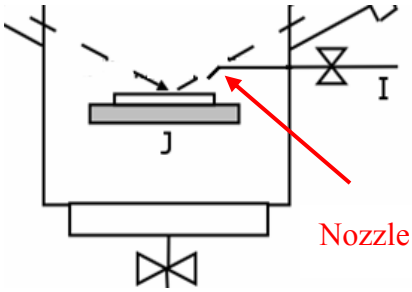

Figure 3.23. Gas distribution ring replaced by a capillary through which silane is injected towards the substrate.

Table 3.2. Thickness of SiO_2 deposited in different positions of the reactor

Sample number (as shown on Figure 3.22)	Thickness (nm)
1 (substrate holder)	419.0
2 (top of the gas ring)	288.9
3 (reactor wall)	33.3
4 (bottom of the reactor)	55.2

The results shown in Table 3.2 clearly show that the real system can not be considered or modeled as a well-mixed reactor, since the growth rate can differ by as much as 12 times within a 10 cm distance. The explanation of this can be given by the beam experiment, where flux of silane of different flows is injected towards the substrate from the capillary. A capillary with 1 mm opening is replacing the gas distribution ring and experiment is done in conditions where uniformity of the deposition of silica (with gas distribution ring) is ±5 percent across 200 mm wafer. Oxygen flow and microwave power were 40 sccm and 2x500 Watt, respectively, with pressure kept at 1.5 mTorr.

Results of mapping the thickness along the diameter of a 100 mm wafer clearly shows that not only the thickness is increasing almost linearly with silane flow, but also local concentration of silane is very important factor, as depicted in Figure 3.24. Non-uniform density within the beam evidently has impact on the deposition profile.

Further studies can give more quantitative data, but we already have demonstrated the important fact, that SiO_2 deposition in ECR plasma cannot be considered as process taking place in well-mixed reactor, contrary to the current believes[20, 21]. Figure 3.24 clearly shows that in the design of gas injection system one has to take utmost care in providing uniform silane fluxes onto the wafer. Not only the plasma need to be uniform, and uniform plasma alone will not provide uniform deposition.

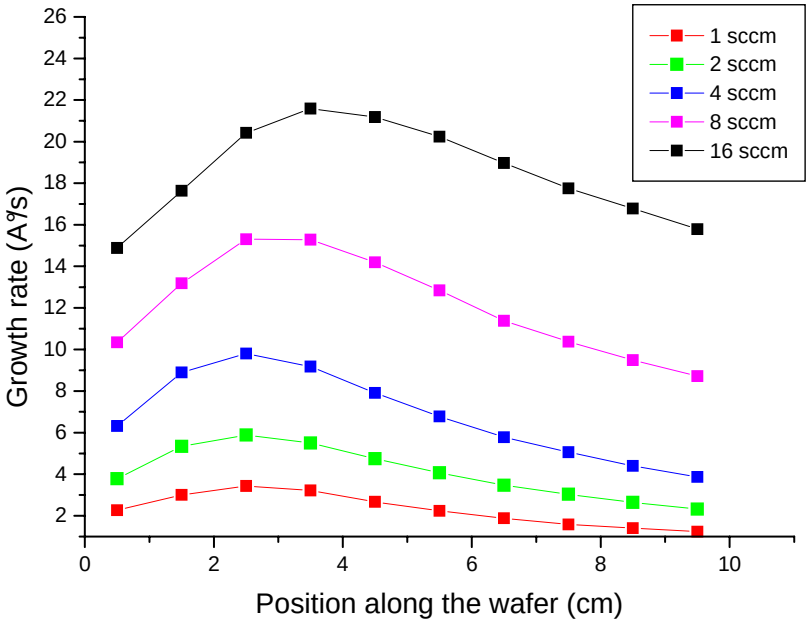

Figure 3.24. The growth rate distribution for various silane flows.

3.5. Conclusion

In this Chapter, the architecture of the *Venus* reactor, built during this thesis, was presented. Characterization of the different parts of the vacuum system and gas panel, the system leak rate and gas residence time, as well as the software developed for control of the MFCs, valves and magnetrons was discussed. In addition to the residence time, the response time of the developed software and MFCs was determined in order to ensure adequate operation during deposition and real-time control of depositions. Initial plasma characterization was carried out using OES measurements, with results showing good correlation with existing literature. Varying process parameters such as the RF substrate bias, microwave power and gas flows demonstrated the expected tendencies. The results contained in Section 3.3 will be referred to again later in Chapter 4. The use of multi-wavelength kinetic ellipsometry will be discussed in Chapter 5. To conclude this Chapter, the working principle of the entire system can be summarized as depicted in Figure 3.25.

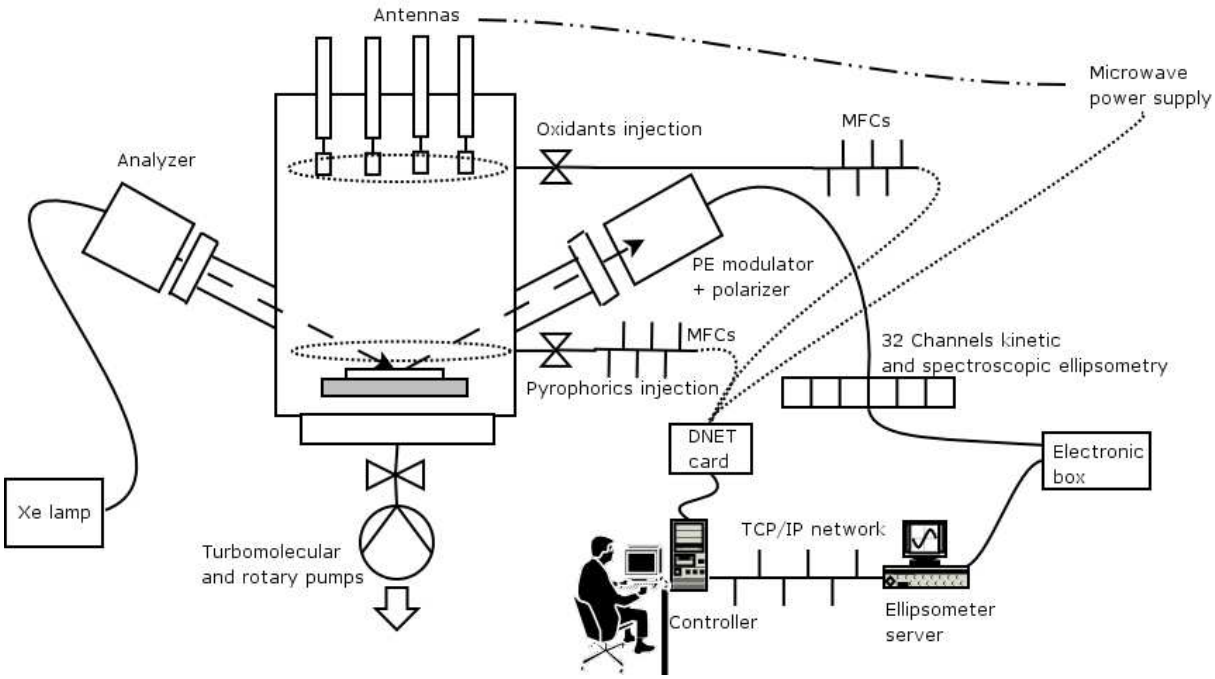

Figure 3.25. A summary of the different parts of the reactor Venus.

References

[1] B. Haj Ibrahim, P. Bulkin, D. Daineka, B. Drevillon, *Optical thin films deposition by MDECR-PECVD,* SPIE Proceedings 5963, pp. 500 –506, (2005).

[2] A. Lacoste, T. Lagarde, S. Béchu, Y. Arnal, J. Pelletier, Multi-*dipolar plasmas for uniform processing: physics, design and performance,* Plasma Sources Science Technology, Vol. 11, pp. 407-412, (2002).

[3] S. Béchu, O. Maulat, Y. Arnal, D. Vempaire, A. Lacoste, J. Pelletier, *Multi-dipolar for plasma-based ion implantation and plasma-based ion implantation and deposition,* Surface & Coatings Technology, Vol. 186(1-2), pp. 170-176, (2004).

[4] T.C. Pulick, *Guidelines for construction of low-pressure gas manifolds,* Journal of Vacuum Science and Technology, Vol 21(4), pp. 1032-1036, (1982).

[5] A. Chambers, R.K. Fitch, B.S. Halliday, *Basic Vacuum Technology, 2nd Edition, Institute of Physics Publishing,* IoP publishing, Bristol, (1998).

[6] M. Pirani, J. Yarwood, *Principles of Vacuum Engineering*, Chapmann and Hall, (1963).

[7] M.A. Lieberman, A.J. Lichtenberg, *Principles of Plasma Discharges and Materials Processing,* 2nd Edition, pp. 274-283, John Wiley & Sons, (2005).

[8] J.R. Roberts, *Optical emission spectroscopy on the Gaseous Electronics Conference RF Reference Cell,* Journal of Research of the National Institute of Standards and Technology, Vol. 100(4), pp. 353-371, (1995).

[9] U. Fantz, *Basics of plasma spectroscopy,* Plasma Sources Science and Technology, Vol. 15, pp. S137-S147, (2006).

[10] S.F. Yoon, K.H. Tan, Q. Zhang, M. Rusli, J. Ahn, L. Valeri, *Effect of microwave power on the electron energy in an electron cyclotron resonance plasma,* Vacuum, Vol. 61, pp. 29–35, (2001).

[11] T.T. Chau, K.C. Kao, *Optical emission spectra of microwave oxygen plasmas and fabrication of SiO2 films,* Journal of Vacuum Science and Technology B, Vol. 14(1), pp. 527–532, (1996).

[12] A.J. Flewitt, A.P. Dyson, J. Robertson and W.I. Milne, *Low temperature growth of silicon nitride by electron cyclotron resonance plasma enhanced chemical vapour deposition,* Thin Solid Films, Vol. 383, pp. 172 – 177, (2001).

[13] J.C. Thomaz, J. Amorim, C.F. Souza, *Validity of actinometry to measure N and H atom concentration in N2-H2 direct current glow discharges*, Journal of Physics D: Applied Physics, Vol. 32, pp. 3208 – 3214, (1999).

[14] M. Tadokoro, A. Itoh, H. Nakano, Z.L. Petrovic, T. Makabe, *Diagnostics of an Inductively Coupled Plasma in Oxygen*, IEEE Transactions on Plasma Science, Vol. 26(6), pp. 1724 - 1732, (1998).

[15] A. Granier, M. Vervloet, K. Aumaille, C. Vallée, *Optical emission spectra of TEOS and HMDSO derived plasmas used for thin film deposition*, Plasma Sources Science and Technology, Vol. 12, pp. 89 – 96, (2003).

[16] K. Aumaille, A. Granier, M. Schmidt, B. Grolleau, C. Vallée, G. Turban, *Study of oxygen/tetraethoxysilane plasmas in a helicon reactor using optical emission spectroscopy and mass spectrometry*, Plasma Sources Science and Technology, Vol. 9, pp. 331 – 339, (2000).

[17] S. M. Han, E. S. Aydil, *Plasma and surface diagnostics during plasma-enhanced chemical vapor deposition of SiO_2 from $SiH_4/O_2/Ar$ discharges*, Thin Solid Films, Vol. 290-291, pp. 427-434, (1996).

[18] A. Banerjee, T. DebRoy, *Optical emission investigation of the plasma enhanced chemical vapor deposition of silicon oxide films,* Journal of Vacuum Science and Technology A, Vol. 10(6), pp. 3395-3400, (1992).

[19] S. M. Han, E. S. Aydil, *Study of surface reactions during plasma enhanced chemical vapor deposition of SiO_2 from SiH_4*, O2, and Ar plasma Journal of Vacuum Science and Technology A , Vol.14(4), pp. 2062-2070, (2004).

[20] E. Meeks, R. S. Larson, P. Ho, C. Apblett, S.M. Han, E. Edelberg, E.S. Aydil, *Modeling of SiO_2 deposition in high density plasma reactors and comparisons of model predictions with experimental measurements*, Journal of Vacuum Science and Technology A, Vol. 16 (2), pp. 544-563, (1998).

[21] S. M. Suh, S. L. Girshick, U. R. Kortshagen, M.R. Zachariah, *Modeling gas-phase nucleation in inductively coupled silane-oxygen plasmas,* J Journal of Vacuum Science and Technology A, Vol. 21 (1), pp. 251-264, (2003).

Chapter 4

Deposition of SiO_xN_y Optical Filters by MDECR-PECVD

Silicon oxynitride alloys deposited by PECVD are perfectly suitable materials for realizing multilayer and gradient index filters. Despite a somewhat limited refractive index range, between 1.45 and 1.95 at 2 eV, this material composition is perfectly compatible with all planar technological processes and both, precursors and deposition systems are readily available. They allow deposition of refractive indices in the range between SiO_2 and Si_3N_4 (cf. §1.3.). Due to the fact that the control of the index is done by adjusting the oxygen, nitrogen and silane flows, continuous or abrupt changes are possible. This makes it a convenient technique for both the deposition of gradient index films [1] and multilayer films. Furthermore, optical monitoring done by reflectometry [2] or kinetic multi-channel ellipsometry [3], can allow precise control of the thickness and the index of the layers.

This chapter will start with a short introduction to phase modulated ellipsometry. Next, we will discuss the use of spectroscopic ellipsometry (SE) and Fourier transform infrared (FTIR) spectroscopy for various aspects of the deposition process and characterization of the grown layers. Special emphasis will be placed on the following:

- The characterization of different silicon oxynitride layers.
- The study of the parameters which influence the deposition, such as the magnets' matrix configuration, the biasing of the substrate and the gas flows.
- The relationship between properties of the plasma and of the films.
- The use of all these factors in the design and implementation of manufacturing procedures for optical filters.

The deposition technique used is MDECR-PECVD, but the control techniques can be easily adapted to any CVD process.

4.1. Phase Modulated Ellipsometry

Ellipsometry is an optical technique based on the measurement of the change in the polarization of light after reflection from a surface. This change is deduced from the measurement of the ratio ρ of the complex Fresnel reflection coefficients (cf. §1.1.2) between the two eigen-modes of polarization [4, 5] r_s and r_p:

$$\rho = \frac{r_p}{r_s} = \tan\Psi \exp(i\Delta) \qquad (4.1)$$

In phase modulated ellipsometry [4-8], the principle of operation lies in determining the ellipsometric angles Δ and Ψ from the parameters I_S and I_C, which are proportional to the first and the second harmonics of modulation frequency. If the base angular modulation frequency[a] is ω then the modulated phase is given by:

$$\delta(t) = A\sin(\varpi.t) \qquad (4.2)$$

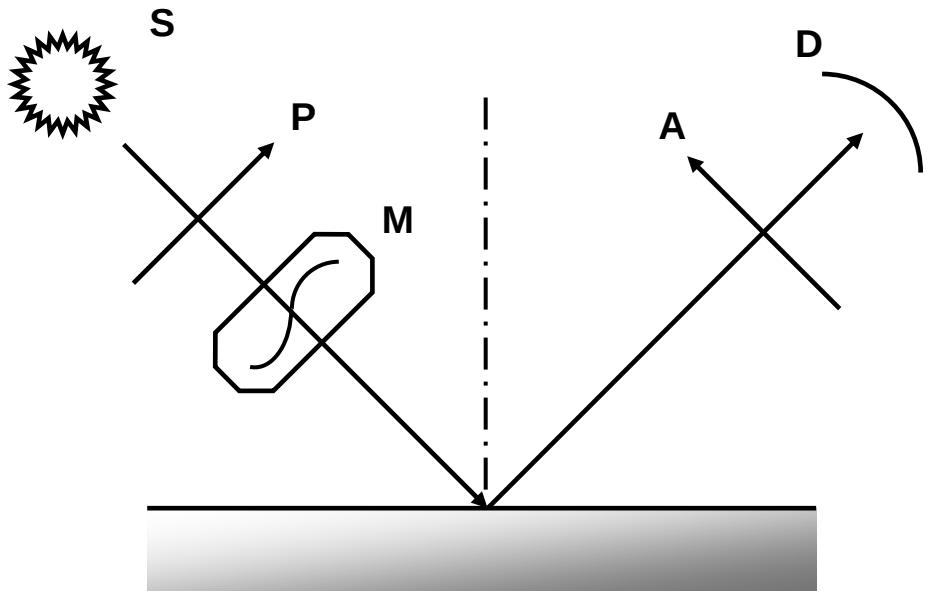

Figure 4.1. Schematic view of a phase modulated ellipsometer: S: source, P: polarizer, M: modulator, A: analyzer, D: detector.

[a] The modulation frequency for the UVISEL ellipsometer is 50 kHz.

After the analyzer (see Figure 4.1), the measured intensity is given by:

$$I(t) \propto I_0 + I_S \sin\delta(t) + I_C \cos\delta(t) \qquad (4.3)$$

During measurements, the parameters I_S and I_C are obtained directly from the digital signal processing unit of the UVISEL ellipsometer[a]. All the following calculations related to the sample, such as the deduction of the ellipsometric angles Ψ and Δ, or the determination of *n* and *k*, are done by a specialized software which fits the optical model to the data. When the modulator and the analyzer angles are respectively 0 and 45 degrees (which are the most common positions), the I_S and I_C parameters can be associated with the complex Fresnel reflection coefficients as follows:

$$I_S = 2\,\mathrm{Im}\left(\frac{r_S r_P^*}{r_S r_S^* + r_P r_P^*}\right) = \sin 2\Psi \sin\Delta \qquad (4.4)$$

$$I_C = 2\,\mathrm{Re}\left(\frac{r_S r_P^*}{r_S r_S^* + r_P r_P^*}\right) = \sin 2\Psi \cos\Delta \qquad (4.5)$$

Ellipsometers can be used *ex-situ* for the accurate characterization of samples. The interest of this work is, however, mainly in real-time process monitoring and control, in other words *in-situ* kinetic characterization during the deposition. In the kinetic acquisition mode, spectroscopic acquisition using normal scanning monochromator is, as a rule, not feasible, unless very slow processes are studied. For the real-time monitoring and control with reasonably fast reaction times (less than one second), acquisition is done using a spectrograph with a number of photomultiplier tubes (PMT) or a CCD detector. This technique allows one to obtain the ellipsometric parameters simultaneously for every wavelength investigated. By comparing the measured optical data of the different channels with simulated ellipsometric trajectories in (*Ic*, *Is*) space for the corresponding wavelengths, the deposition process can be monitored and controlled. In real-time, measured deviations from the theoretical trajectories can be corrected and fed back to the deposition system.

[a] The processing unit delivers S_ω and $S_{2\omega}$, the intensities carried by the first and second harmonics. The calibration parameters should then be taken into consideration. (cf. Chapter 5)

Two UVISEL (Jobin-Yvon, Horiba Group) phase modulated spectroscopic ellipsometers were used in this work, for kinetic control (*in-situ* configuration) and spectroscopic characterization (*ex-situ* configuration) in the wavelength range 826 nm to 248 nm (1.5 eV – 5 eV) and 1550 nm to 248 nm (0.8 eV - 5 eV) respectively. After ellipsometric measurement of the deposited layers, the classical Lorentz oscillator or Tauc-Lorentz models[a] are used for description of the dielectric functions of the films [9, 10], using *DeltaPsiII* software provided by the manufacturer of ellipsometer (Jobin-Yvon).

In the models we suppose that the single layers are isotropic and homogeneous with a surface layer representing roughness with a 50% material and 50% void composition [10]. The isotropy of the layer results from the amorphous nature of all the deposited layers and from the absence of stress. In the case of anisotropic materials, the coupling between the two main polarizations should be taken into account when modeling them.

4.2. Characterization by Spectroscopic Ellipsometry

Two silicon oxynitride series were deposited using N_2 and O_2, with 5 sccm and 10 sccm SiH_4 flows respectively, as precursors [11]. The oxygen to nitrogen ratio was varied, while the other process parameters were kept constant, namely a total oxidants flow of 80 sccm, 1kW microwave power and 1.5 mTorr process pressure. After the deposition, spectroscopic ellipsometry measurements were taken and modeled to obtain refractive indices and growth rate curves for each series. The in-depth homogeneity of each single layer is optimized by keeping all the parameters influencing the deposition stable, including gas flows, microwave power, temperature and pressure. In reality, there are small fluctuations of gas flows due to the pressure regulators behavior and the electronic stabilization of the MFCs, as well as an increase in the substrate temperature while depositing. These fluctuations do not have a significant effect on the homogeneity, since the resulting SE data fitting of single layer depositions with a two-layer model (for the bulk and the surface roughness) always gives a low χ^2.

[a] See Appendix I for a discussion of these models.

Figure 4.2 illustrates the corresponding refractive index dispersion curves for an increase in the oxygen to nitrogen flow ratio $O_2/(O_2+N_2)$, as noted on the figure. A silane flow of 5 sccm was used while the other parameters were kept constant as mentioned earlier. As can be seen, the refractive index corresponds to materials ranging from silicon nitride SiN_x when the ratio is set to 0, to silicon oxide SiO_x at a ratio of 0.25 [12]. At flow ratios in excess of 0.25 the index does not change noticeably and follows the index of reference silica material.

.

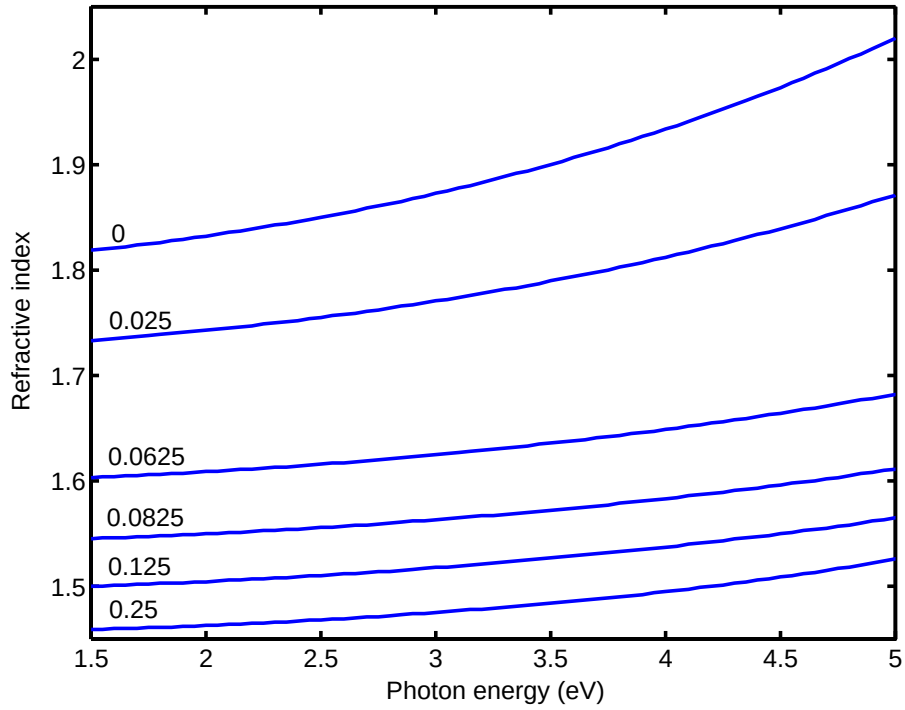

Figure 4.2. SiO_xN_y refractive index dispersion curves at various oxidants flow ratios.

As shown in Figure 4.3, the influence of the silane flow on the silicon oxynitride refractive index, when no RF substrate bias[a] is applied, depends on the oxidants ratio. For a higher oxygen to nitrogen ratio, an increase in the silane flow induces an increase in the index. Here, the films contain a greater nitride phase at high silane flow than the at lower silane flow. This is due to the higher reactivity of oxygen compared to nitrogen. The oxygen will consequently consume a higher amount of the silicon to produce Si-O bonds than the nitrogen will, when the silane supply is limited and there is competition for Si atoms.

[a] For a discussion on the influence of the substrate RF biasing has on depositions, please refer to Section 4.6.

However, when the silane flow increases, the amount of reactive oxygen arriving to the substrate surface starts to be insufficient to consume all the available silicon and we have a higher nitrogen contribution, leading to an increase in the N/O ratio in the layer and a resulting increase in the index of the SiO_xN_y film.

In the case of low oxygen to nitrogen ratios, the oxygen is already in limited supply and fully consumed, while the nitrogen reactivity is low. If we do not increase the nitrogen flow, any increase in the silane flux will lead to a rise in the hydrogen content of the film and will result in a decrease of the film density and the refractive index, as will be shown in the FTIR results in Section 4.6.

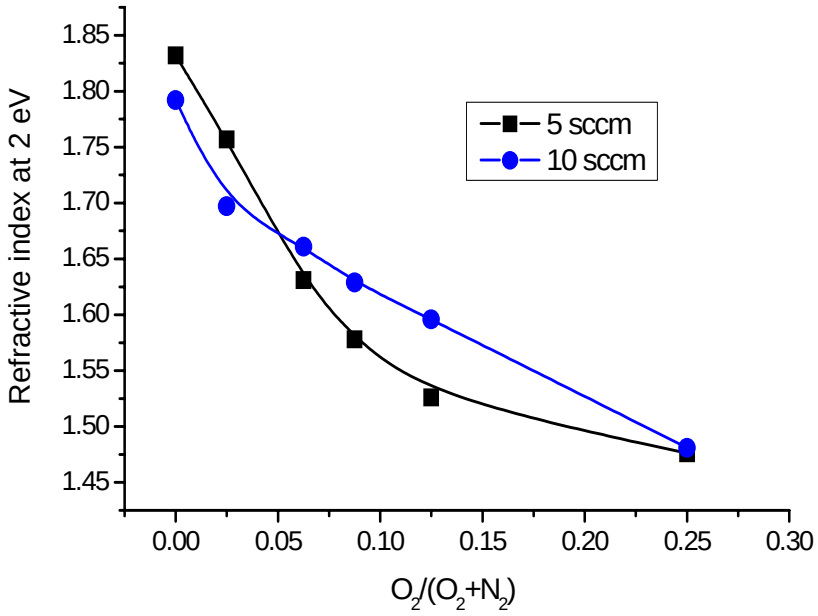

Figure 4.3. Refractive index versus oxidants ratio, at different SiH_4 flows.

Figure 4.4 shows the growth rate increase with increased $O_2/(O_2+N_2)$ ratio for two different silane flows. In both cases, the growth rate versus gas flow ratio curve tends towards saturation. If we consider that the amount of silicon arriving on the growth surface and being incorporated into the film does not change and the fact that the density of silicon nitride is considerably higher than that of silicon dioxide (3.2 versus 2.5 g/cm^3 for stoichiometric materials), this behaviour is to be expected.

For a 10 sccm silane flow, the growth rate is approximately double that of a 5 sccm silane flow for all the oxidants flow ratios. However, from Figure 4.3 we have seen a decrease in the nitride index for 10 sccm silane, which leads to a decreased range of the refractive index attainable at a higher deposition rate. We have done several other experiments with different silane flows, all of which have confirmed that lowering the silane flow increases the nitride index. Hence, while increasing the silane flow might offer the advantage of higher oxynitride deposition rate, the index range is lowered, whereas a higher index for nitride can be obtained by reducing the silane flow, but consequently also lowering the growth rate.

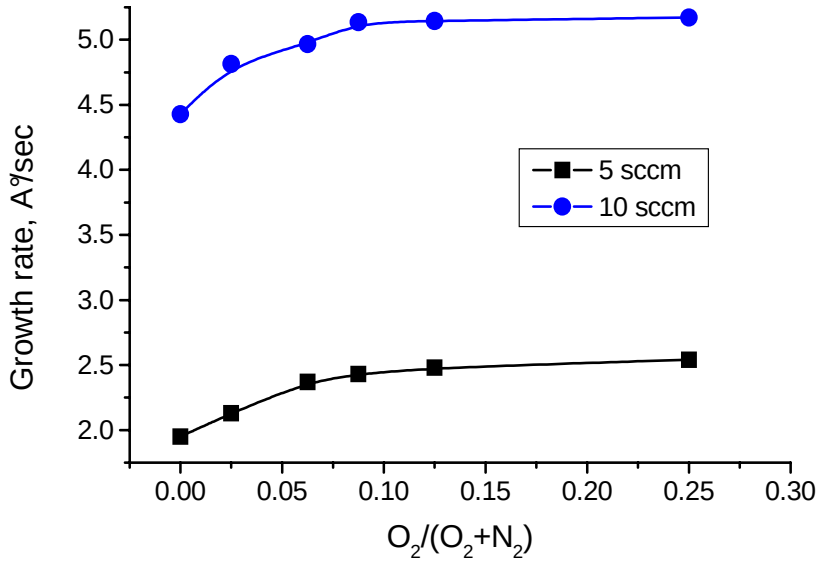

Figure 4.4. Growth rate versus oxidants ratio, at two different SiH_4 flows.

The decrease of the silicon nitride refractive index with increased silane flow, as shown in Figure 4.3, is due to an increase of N-H bonds forming in the layer as proven by Figure 4.5 [a]. When the deposition rate is an important parameter for the deposition, one has to consider other means to keep the refractive index from dropping. Increasing the ion bombardment will facilitate the removal of this reaction product (NH_3) from the growth surface and may offer a possible solution. This can be achieved by RF biasing the substrate holder (cf. § 4.6).

[a] For very high silane flows, we start again to have an increase in the index due to the increased silicon content in the layer [13, 14]. This limit is not reached at the gas flows used in the current work.

Conversely, the increase in the silicon oxide growth rate with raised silane flow does not affect the refractive index at all. The reason for this discrepancy is simple: When depositing silica, the formed byproduct is water [15]. Given the high thermal effect of the silane and oxygen reaction, the removal of water from the growth surface is much more efficient than in the silicon nitride case. Consequently, we have an almost similar hydrogen content in the silica films deposited at different silane flows, whether it is 5 or 10 sccm of SiH_4.

4.3. Characterization by FTIR Spectroscopy

In order to investigate the film quality and changes in the bonding structure when the gas composition is altered, FTIR measurements were taken. The necessary films with thickness between 250 and 300 nm were deposited onto double-polished, high-resistivity (more than 1200 Ω·cm) monocrystalline silicon wafers. A *Bruker Equinox 55* FTIR spectrometer was used in absorbance mode in the range of 400 to 4000 cm^{-1}. Baseline correction was done using a spectra of a bare silicon sample taken each time from the same wafer.

The spectra in Figure 4.5 shows that with an increased nitrogen content in the $O_2 / (O_2+N_2)$ ratio, there is a constant shift of the absorption maximum to shorter wavenumbers. This indicates a gradual replacement of the Si-O stretching bonds at 1050 cm^{-1} with Si-N bonds at 860 cm^{-1}. One different secondary peak can also be observed at 3340 cm^{-1} on all the oxynitride samples, with the exception of the 0.25 oxidants ratio one [12, 16]. This peak corresponds to an N-H bond due to the silane precursor's dissociation. No phase separation can be observed for any of the SiO_xN_y films, as is sometimes reported [17].

It is interesting to note that with only 25 percent of oxygen in the gas phase oxidants mixture, the deposited material constitutes a good quality silicon oxide [18], due to the much higher reactivity of oxygen than nitrogen, as discussed in § 4.2. Figure 4.6 shows the FTIR spectra of a pure silica layer [19, 20] and a SiO_xN_y layer with a 0.25 oxidants ratio which shows a negligible content of Si-N bonds at 880 cm^{-1} [18]. The influence of applying an RF bias to the substrate holder on the byproduct content of the films will be investigated in Section 4.5.

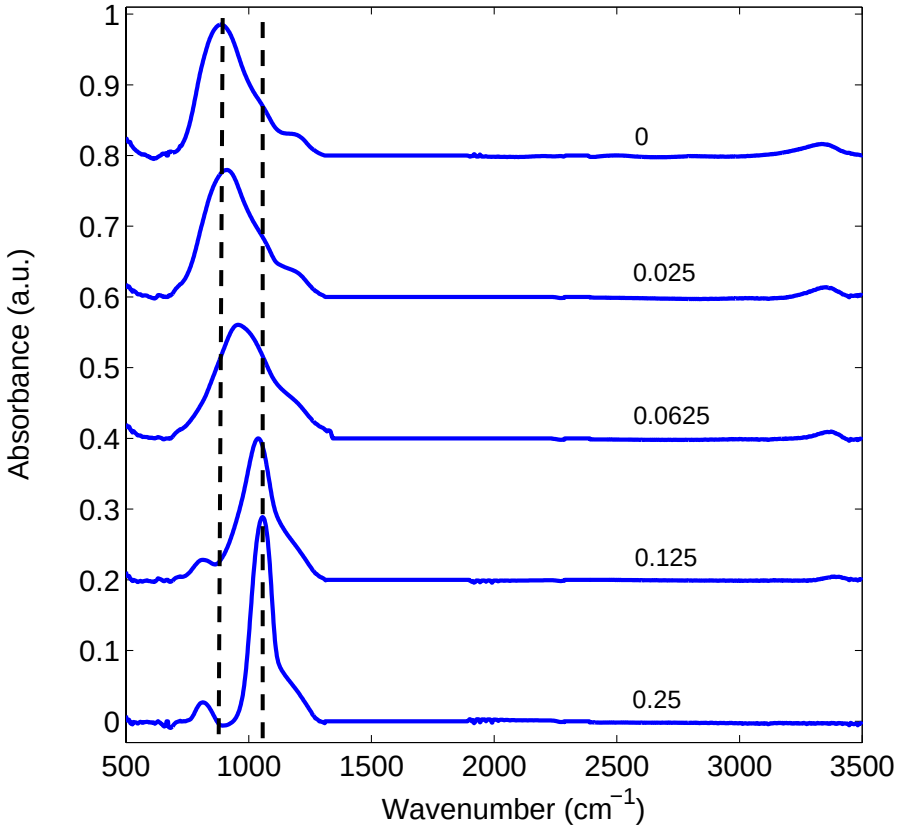

Figure 4.5. FTIR spectra of SiO_xN_y, using a 5 sccm SiH_4 flow.

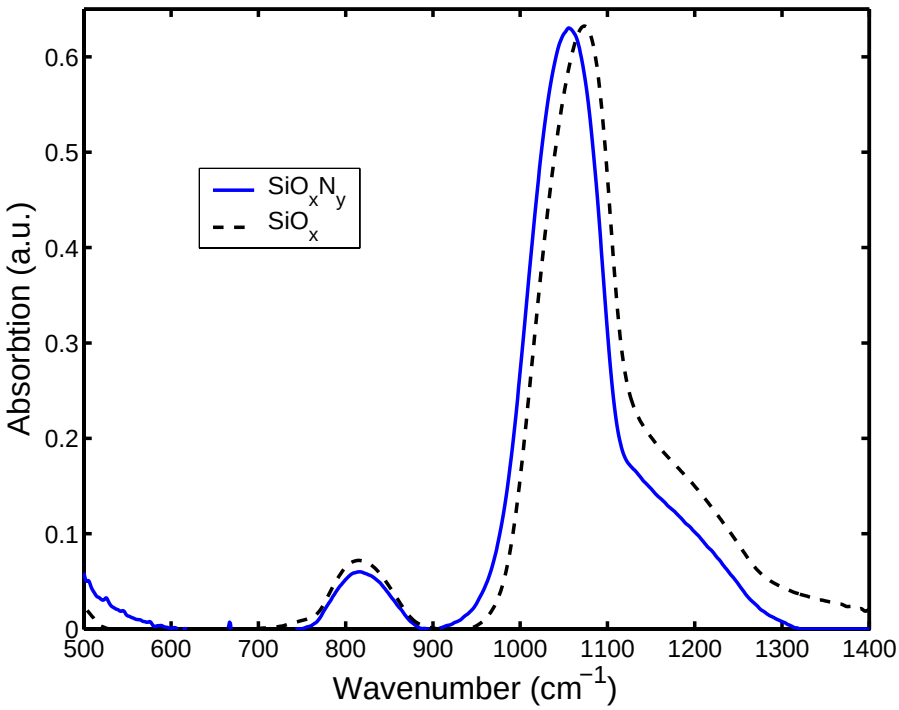

Figure 4.6. Comparison of SiO_2 deposited with pure O_2 and with O_2+N_2 mixture.

4.4. The Influence of the Magnet Matrix Configuration

The principal effect of the matrix configuration of magnets described in Chapter 3, is on the thickness uniformity of the deposition. The distribution of north or south poles on the antennas matrix influences the positions of the ECR regions which, in turn, influences the ionization zones [21-24] and ion and radical fluxes to the surface and therefore the uniformity.

In order to understand the effect the magnetic field uniformity and the distribution of the ECR regions have on the uniformity of the depositions, simulations were done for two antennas, using the *Vizimag 3.41* software. This allowed drawing of the magnetic field lines and their distribution. Figures 4.7 and 4.8 depict both the case of (a) two different and (b) two similar polarities facing the substrate[a].

When we have similar polarities, the ECR zones are larger and more evenly distributed than in the case of different polarities where they are markedly narrower, as can be seen in Figure 4.8. Since the substrate dimensions are smaller than the dimension of the antennas matrix, the most influencing antennas are located in the center[b].

[a] The 875 G zone is located between yellow and green.

[b] The substrate diameter (20 cm) puts samples directly under the 2x2 central antennas (16x16 cm) and their influence zone (3-4 cm added to the antennas sides).

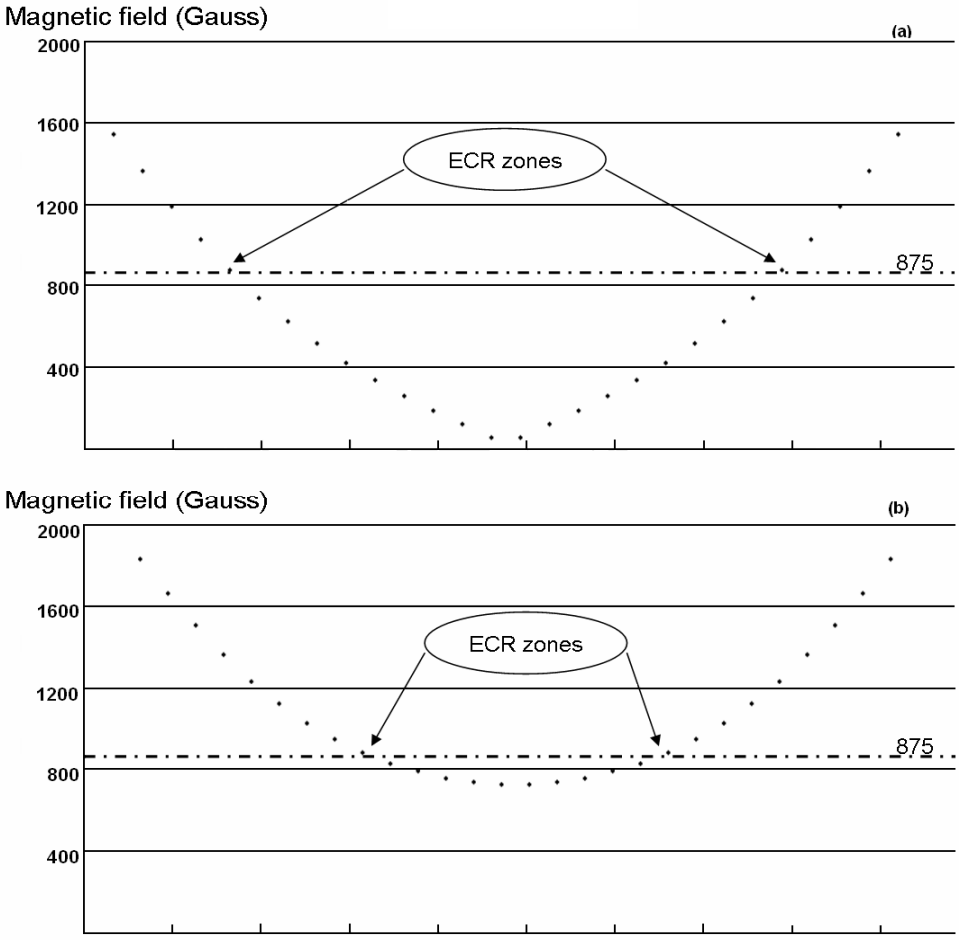

Figure 4.7. Magnetic field strength and ECR zones along a line connecting the midpoints of two magnets: (a) different directions of polarities, (b) similar directions of polarities.

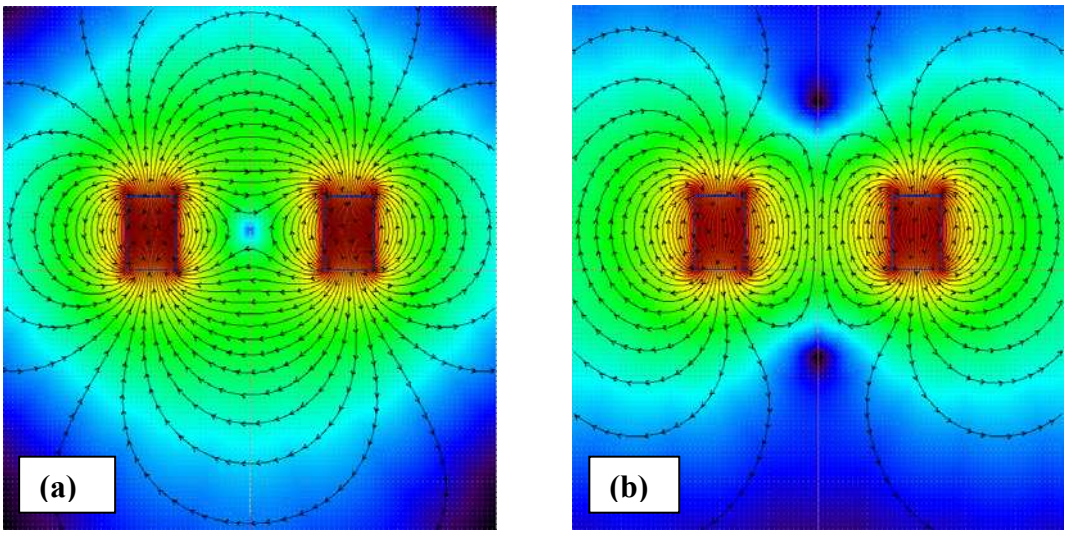

Figure 4.8. Simulation of the magnetic field distribution between two antennas: (a) different directions of polarities, (b) similar directions of polarities.

In *Venus*, 4 south-pole and 12 north-pole terminated antennas are only available. Initially, the configuration used was setting the S poles on the four corners of the antenna matrix. The highest growth rate was found under the central antennas in a cross shape, as shown in Figure 4.9(a). Outside this region the growth rate was markedly lower. The uniformity was of the order of ±10 % on a 200 mm diameter substrate as presented in Figure 4.10(a) with very sharp changes across the wafer[25].

In Figure 4.9(b), the second magnetic configuration is shown. It consists of four south poles on the diagonal, and the north poles arranged around them, with the purpose of providing more uniform deposition in the middle. This configuration allows for multipolar confinement between S and N poles, and then makes the deposition more uniform. The four south pole magnets in the center now have larger ECR zones, with increased growth rate under them. Figure 4.10(b) gives a view of the SE measurement mapping, showing an improvement in the uniformity to ±5 % over the 200 mm diameter of the sample. Due to the saddle shape of the samples uniformity, a third configuration was tested.

The final configuration is similar to the second, but with a gradual lowering of the N poles around the S diagonal, with the outermost being the lowest (closest to the substrate), as explained in Figure 4.9(c). The purpose is to increase the effect of the furthest antennas by reducing their distance from the substrate. This will lead to a compensation of the lower plasma density next to the walls, resulting in a higher growth rate under these antennas as can be seen in Figure 4.10(c). The result was an improvement in uniformity to ±3,3 % on a 200 mm wafer.

In all these cases the refractive index was found to be identical within the error margin of the ellipsometric measurements.

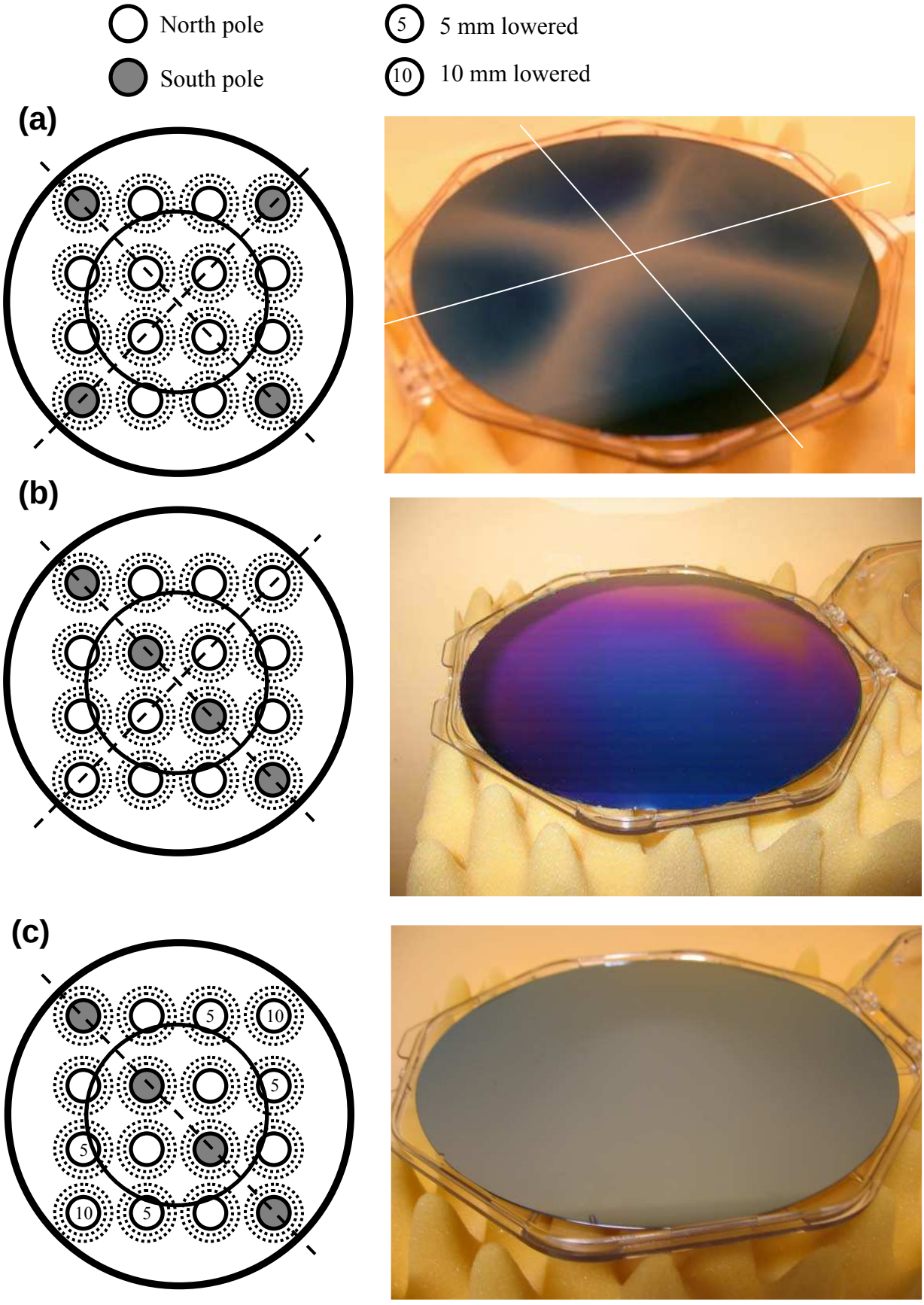

Figure 4.9. Uniformity with changes in the magnet matrix configuration. The small circle indicates the size of the substrate.

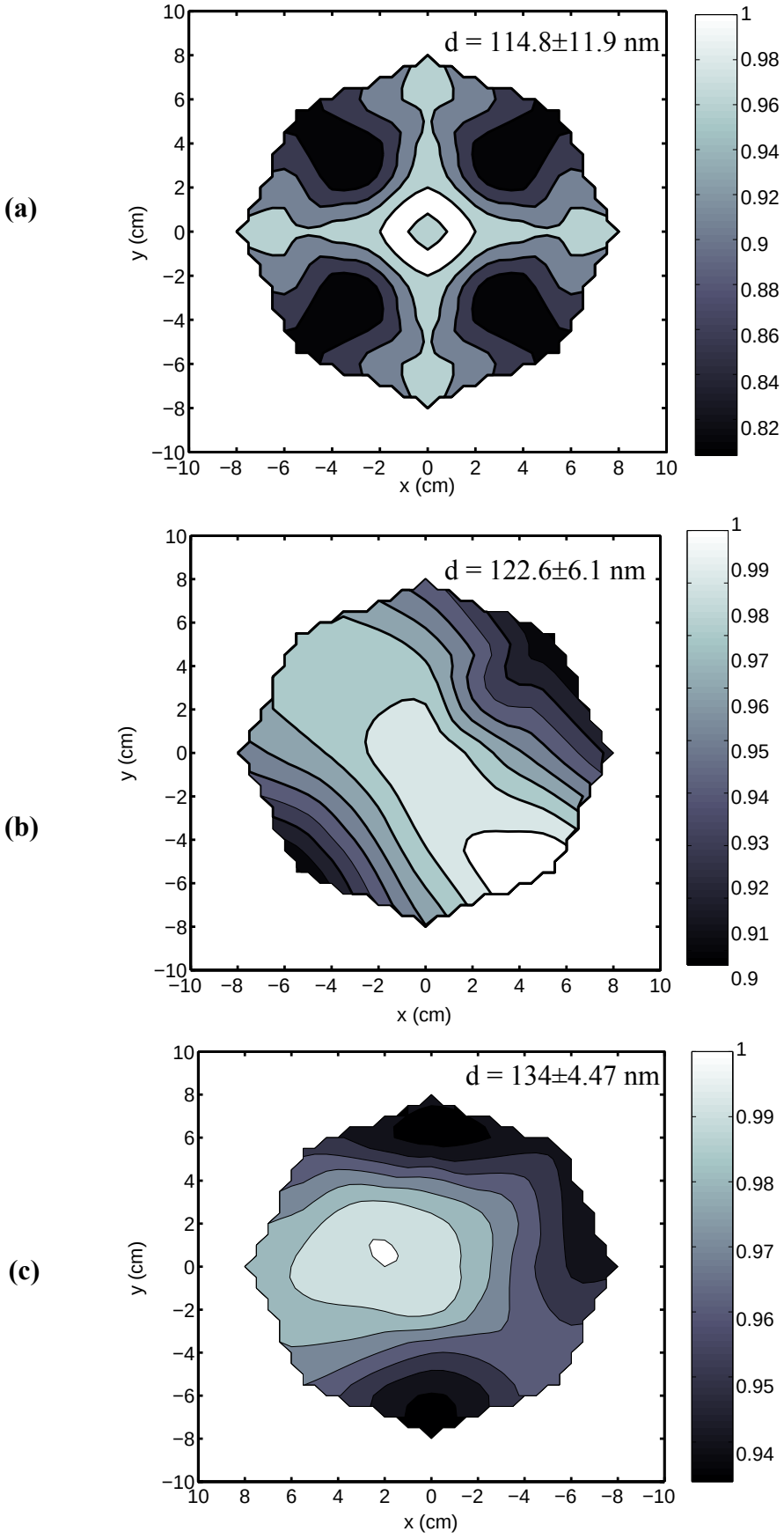

Figure 4.10. Uniformity contours for the configurations shown in Figure 4.16 (a)-(c).

4.5. The Influence of the Applied Microwave Power on SiN_x Deposition

Silicon oxide layers deposited from SiH_4-O_2 or oxygen-rich SiH_4-O_2-N_2 mixtures showed very good values of index of approximately 1.46, which is close to that of thermal silica, for different deposition parameters. On the other hand, silicon nitride layers did not display this stability for different gas ratios, as was mentioned in § 4.2. This led to the study of SiN_x depositions dependence on other operation parameters.

As it is not evident how the microwave power influences the silicon nitride layer's growth due to its gas ratio dependency, we fixed the gas flows at 80 sccm for nitrogen and 5 sccm for silane. These are the gas flow values typically used during optical layer depositions in the reactor. The microwave power was then varied between 600 and 1400 Watts.

As Figure 4.11 shows, the refractive index increases linearly with the microwave power. Thickness normalized FTIR spectra of these samples are depicted in Fig. 4.12, which showed a shift of the nitride peak towards the Si-N stretching bond at 860 cm^{-1} with a narrower shape at increased power, which correlates well with the observed increase in index. The Si-H stretching mode that can be found at ~2130 cm^{-1} is not seen in any of the samples [26].

The N-H stretching bond at 3330 cm^{-1} did not change, while the bonds at 1070 cm^{-1} and 1150 cm^{-1} are due to NH_2 and Si-NH-Si [27,28]. These three bonds give an indication of the hydrogen content of the films. The drop in the intensity of the 1070 cm^{-1} and 1150 cm^{-1} bonds suggest a decrease in the hydrogen content with increased microwave power, which is confirmed by the increase in refractive index observed in Figure 4.11.

For the majority of the experiments, the microwave power was set to 1000 Watts. While the quality of the layers is higher at increased microwave power, this intermediate solution is used to reduce the heating of the reactor. Higher powers can be used for short depositions or if a cooling system for the chamber is installed.

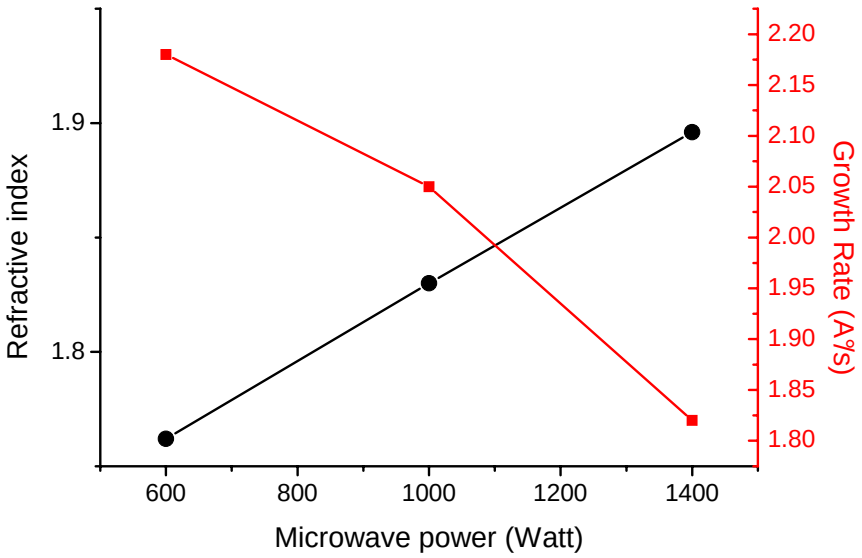

Figure 4.11. Variation of the refractive index and the growth rate of nitride layers versus microwave power

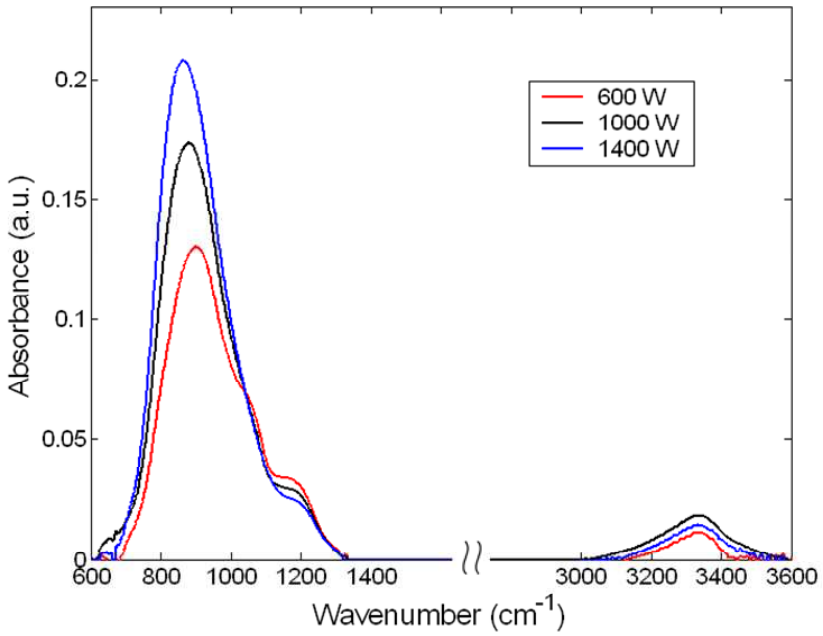

Figure 4.12. Shift of Si-N peak with microwave power.

4.6. The Influence of RF Substrate Biasing

It is known that RF biasing of the substrate holder [29,30] reduces somewhat the growth rate of silicon oxynitride for the same silane flow, as can be seen in Figure 4.13. As mentioned in Section 4.2, the increased ion bombardment facilitates the removal of reaction byproducts (NH_3 and H_2O) from the growth surface, thus increasing the compactness of the film and lowering the growth rate.

Figure 4.14. shows that without RF biasing, the silicon nitride contents of hydrogen for 5 sccm of silane flow is lower than for 10 sccm, and the Si-N bond density is higher.

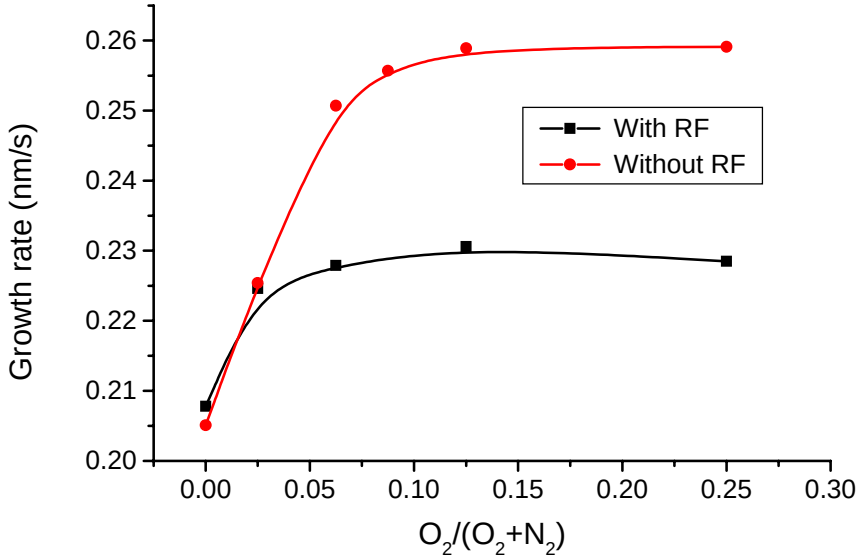

Figure 4.13. Influence of RF biasing of the substrate holder on SiO_xN_y growth rate.

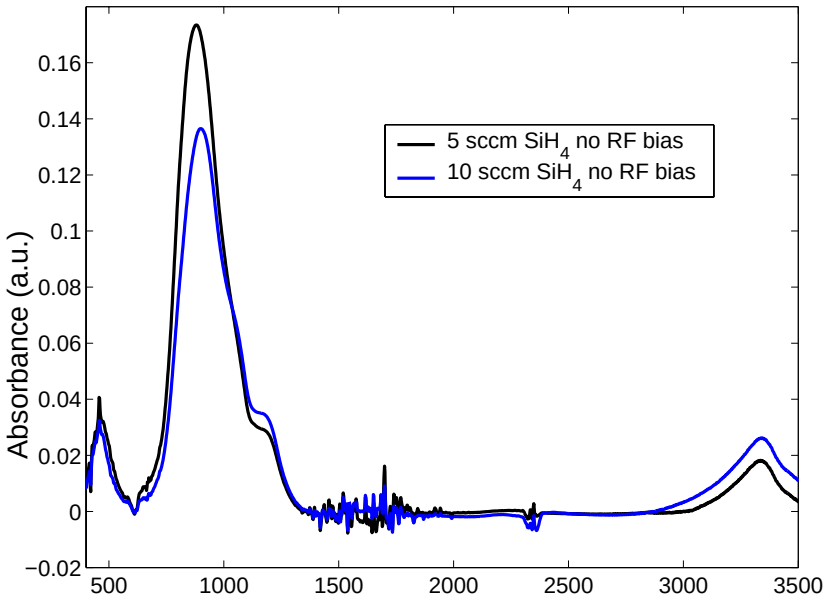

Figure 4.14. FTIR measurement of SiN_x at two different silane flows.

The effect of RF biasing on the refractive index of oxynitride is less clear, however. To study this, the 5 sccm and 10 sccm silane flows used in Section 4.2 will again be considered here.

Figure 4.15 shows a comparison of the refractive index of two oxynitride series, one deposited with and one without an RF bias applied to the substrate holder. A 5 sccm silane flow was used first. It can be seen that when using this low silane flow, the refractive index decreases when an RF bias is applied to the substrate holder.

In order to explain this result, FTIR measurements of silicon nitride layers deposited with and without RF were done. Figure 4.16 shows that applying RF at this silane flow helped decreasing the amount of incorporated hydrogen, since the N-H absorption peak at 3330 cm^{-1} becomes smaller. It also increased the ordering of the layer since it made the Si-N peak at 860 cm^{-1} narrower. But, it reduced the density of the material, demonstrated by the lower peak at 860 cm^{-1} too. So the material is lower in Si-N bond density and refractive index, but with lower hydrogen content.

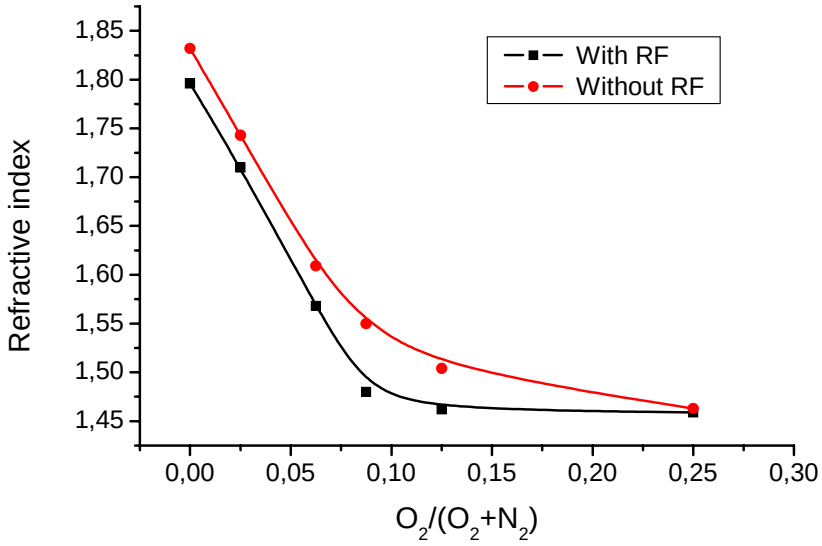

Figure 4.15. SiO_xN_y index at 5 sccm SiH_4 flow, with and without substrate biasing.

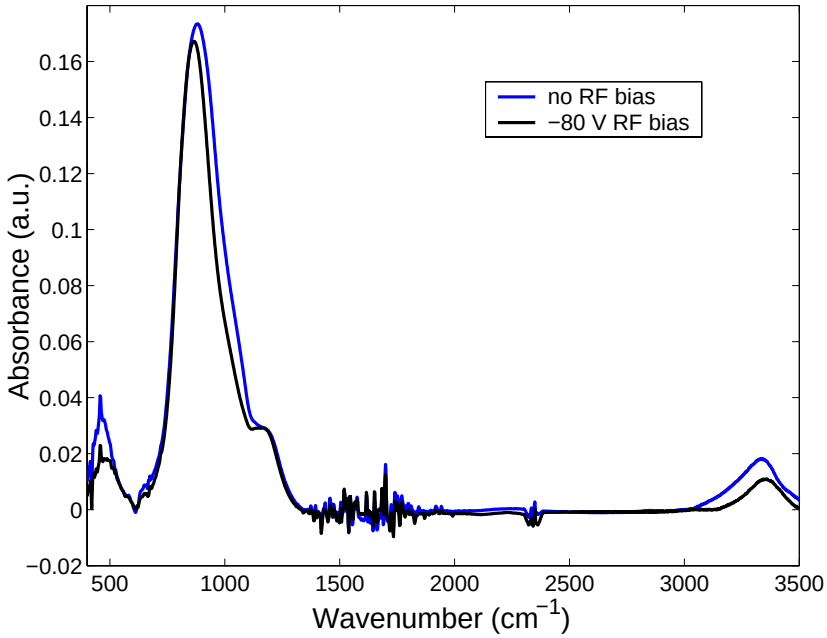

Figure 4.16. FTIR measurement of SiN_x at 5 sccm SiH_4, with and without RF biasing.

This trend however changes when a 10 sccm silane flow is used, as represented in Figure 4.17. As discussed in Section 4.2, a higher silane flow such as this will result in an increased hydrogen content in the layer, as seen from the lowered refractive index when compared with the 5 sccm silane gas flow. The consequent contribution of the RF bias is thus removal of hydrogen during the deposition process, leading to an increased refractive index. As depicted in Figure 4.18, FTIR measurements show that RF biasing contributes in the ordering and densification of the film at this silane flow since the Si-N peak at 860 cm^{-1} is narrower and higher, respectively. The removal of hydrogen is confirmed by the lowering of the N-H peak at 3330 cm^{-1}.

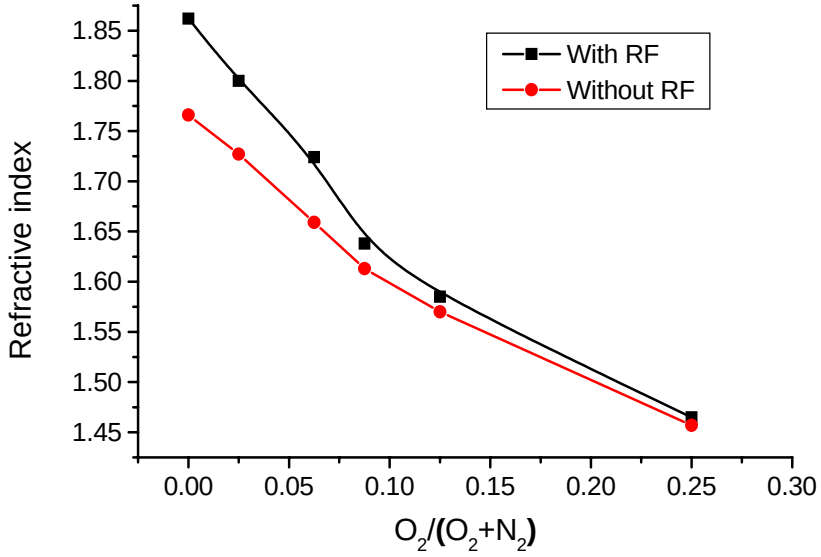

Figure 4.17. SiO_xN_y index at 10 sccm SiH_4 flow, with and without substrate biasing.

Increasing energy of bombarding ions with RF biasing improves the stoichiometry of the films. This was shown by FTIR on nitride layers in Figures 4.17 and 4.18. FTIR measurements taken on silica samples which were deposited with and without RF biasing of the substrate (Figure 4.19), showed a narrowing of the Si-O stretching band at 1080 cm^{-1} when the substrate bias was increased, pointing to an improvement in the ordering in the film[19].

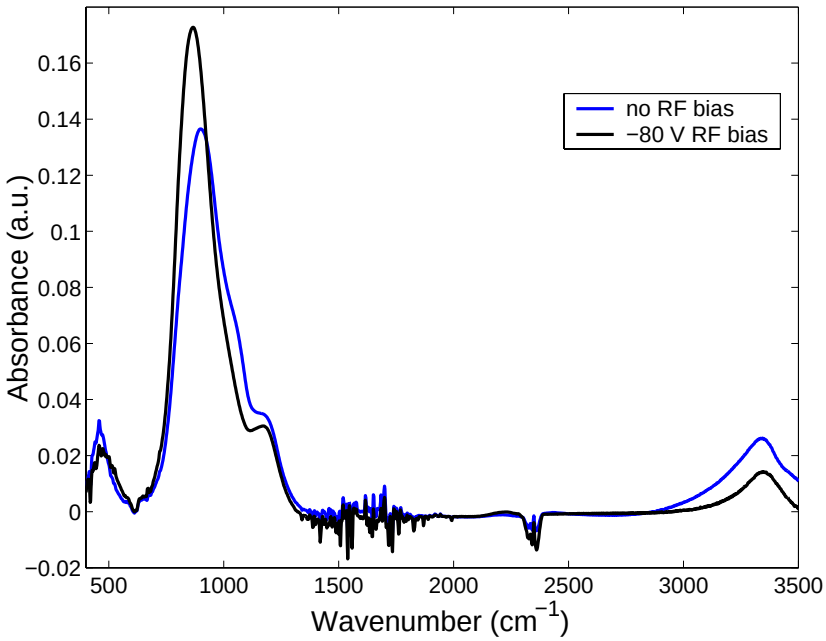

Figure 4.18. FTIR measurement of SiN_x at 10 sccm SiH_4, with and without RF biasing.

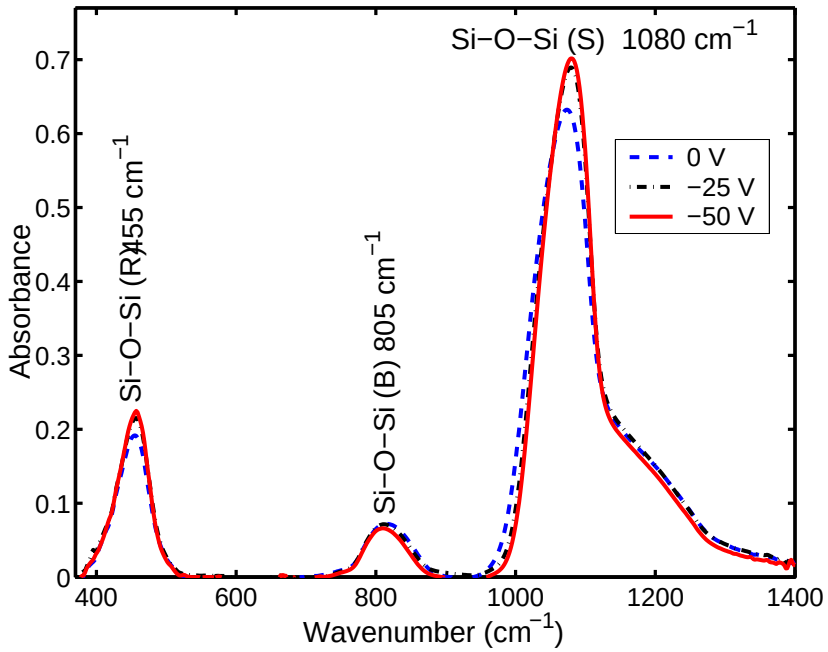

Figure 4.19. SiO_x deposited under different RF biasing conditions.

4.7. The Feed-Forward Deposition of Gradient Optical Filters

In order to perform the design and deposition of optical filters, knowledge of optical index versus flow dependencies is required. After optical characterization of the different SiO_xN_y alloys, the refractive index and growth rate were interpolated with cubic polynomials, since small-increment studies would be prohibitively time-consuming. This provides us with a rather precise table for the use in design calculations.

The following steps were followed in order to create the growth data:

- Writing the table of index versus thickness from the design specifications.
- Deducing the corresponding growth rate of each index.
- Transforming the tables versus thickness into tables versus time.
- Transforming the index tables into gas flow tables.

In order to correctly specify the gas flows, it is necessary to take into account two facts:

- To use at least the minimal values of the MFC flows[a], since the control valve will not open or will close automatically as soon as flow falls below 1 percent of the full scale.
- To use as flow quanta at least the minimal value that an MFC can reliably reproduce.

Consequently, the data were treated accordingly.

The obtained data tables allow deposition of gradient index coatings with pre-programmed index profiles as a function of the film thickness. A linear index profile [31], shown in Figure 4.20, was derived and grown in order to test this method and verify the adequacy of the linear interpolation of the indices and the rates, as well as check the response speed of the MFC's control system. Figure 4.21 presents the monitoring results using kinetic ellipsometry, where the deviation of the measured trajectory was very small compared to the simulated one. Good correlation between simulation and measurement of the deposited layer was found.

[a] This usually corresponds to 1 percent of the full scale.

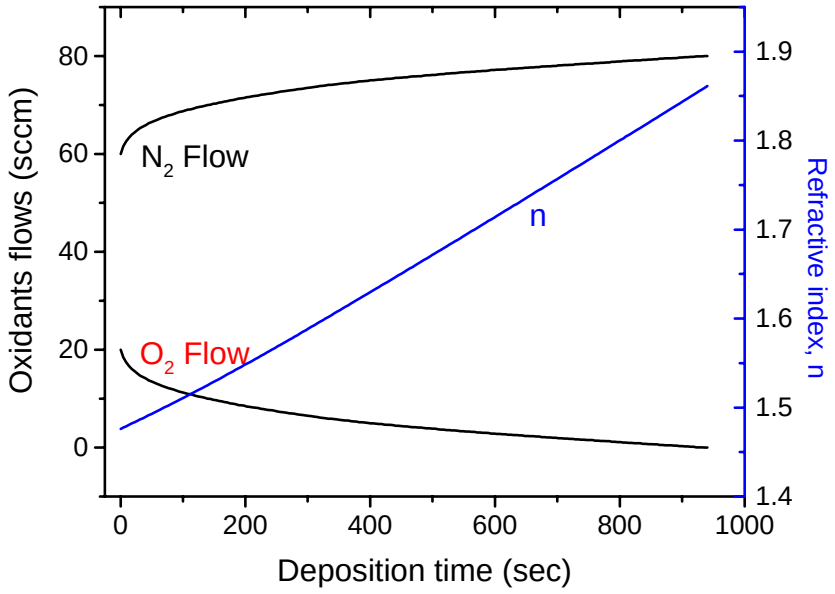

Figure 4.20. Variations in the O_2, N_2 flows and refractive index when depositing a linear gradient index layer.

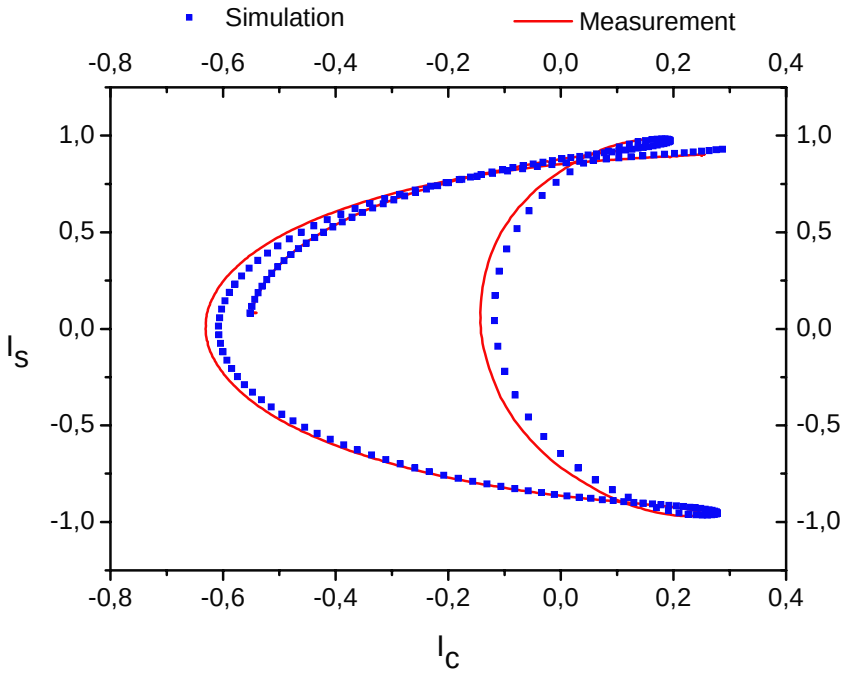

Figure 4.21. The kinetic trajectory of a linear profile at 3 eV.

4.7.1. A Gradient Index AR Coating in the Visible Range

After ensuring the satisfactory performance of the above-mentioned method, an anti-reflection coating for the visible wavelength range with complex gradient index profile was grown, both on one side and on two sides of *Corning 1737* type glass.

In order to simplify the theoretical calculations and conceive a simple deposition process which works with all MFCs, its profile was divided into twenty-one homogeneous sub-layers. Inside each of them the index and growth rate were taken as remaining constant, as demonstrated in Figure 4.22. The AR coating was deposited onto a glass substrate[a] at the same pressure, microwave power and temperature conditions as previously studied (cf. § 4.2) using kinetic ellipsometry monitoring.

Transmission measurements done on these AR coatings are presented in Figure 4.23. They showed good agreement with theoretical calculation, with approximately 2 percent increased transmission on each side, over the entire visible wavelength range.

Compared to classical M2HL multilayer antireflection coatings, these gradient index films can be manufactured in one run with no interfaces inside the coating. This provides higher durability and environmental stability by avoiding the use of low index fluorides which are typically used for multilayer AR coatings. Moreover, it shows a very good stability in terms of deposition parameters.

[a] *Corning 1737* glass, with a refractive index of 1.52 at 2 eV.

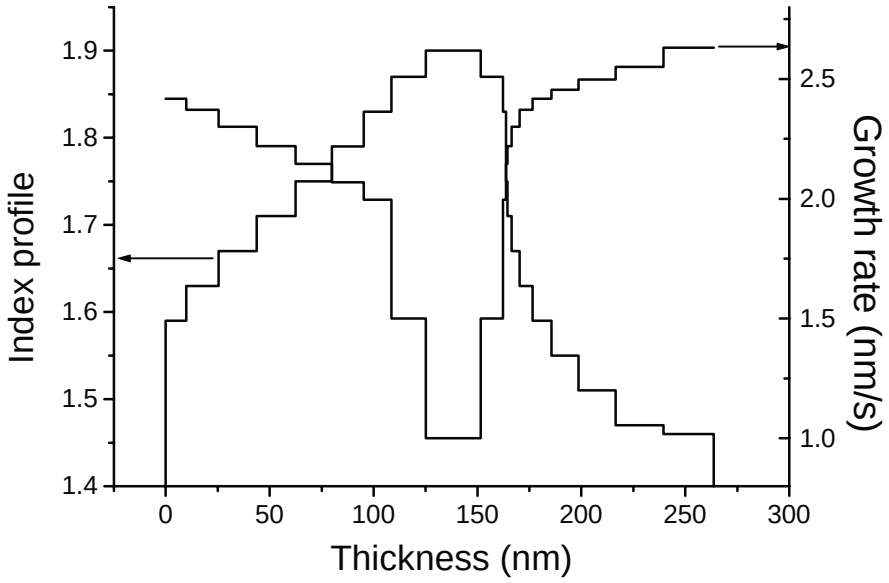

Figure 4.22. Index and rate profile for a gradient index AR coating.

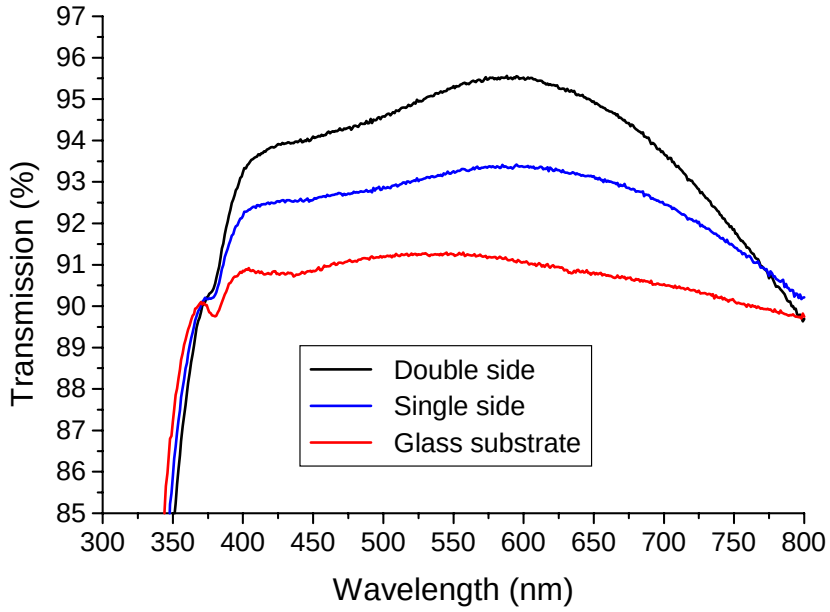

Figure 4.23. Transmission of a gradient index AR coating.

4.7.2. Rugate Filter Deposition and Side Lobe Suppression

The word *rugate* comes from the elementary shape of these filters, which is corrugated or wavy [32]. More precisely, a rugate filter is an interference coating consisting of one or multiple layers within which refractive index versus thickness profile is derived from sine or cosine functions, being of continuously varying value. This structure allows fabrication of reflective mirrors (notch filters) without the harmonic bands which are sometimes annoying in multilayer quarter wavelength filters [33].

A practical expression of the refractive index as a function of the physical thickness for a rugate layer is given by [32-34]:

$$n = \frac{n_2 - n_1}{2} \sin(4\pi \frac{n_{avg} \cdot x}{\lambda}) + n_{avg} \qquad (4.6)$$

Where, n_1, n_2, n_{avg} are the minimal, maximal and average values of the refractive index, respectively, x is the physical thickness and λ the reference wavelength.

In order to have a continuous transition of the index between the glass substrate and the filter, we looked for continuity in the index profile and its first derivative [35, 36]. We consequently suggested the following formula, where X is the optical thickness:

$$n = \frac{n_1 - n_2}{2} \cos(4\pi \frac{X}{\lambda}) + n_{avg} \qquad (4.7)$$

In the following sections, we will explain in more detail the previous choice for side lobe suppression in the passing band of rugate filters.

4.7.2.1. Bovard's model

In multilayer (Bragg) mirrors, the addition of an eighth wavelength optical thickness layer on the bottom and the top of the stack, followed by a software based refinement for these two layers was suggested as a typical solution [32]. On the other hand, for rugate filters, apodization of the index profile with addition of two quintic or rugated quintic layers on the two sides of the deposition was proposed [36]. While, no correlation between these solutions for suppression of the rugate and multilayer side-lobes is remarked, the study of B.G. Bovard [37] demonstrated the possibility of generalization of the rugate filters to the power-sine rugate mirrors. This generalization suggested the unification of multilayer and rugate structures by writing the optical admittance profile versus the optical thickness as the sum of N-shifted power-sine periods.

The previous approach was used in order to achieve rugate filters with reduced total optical thicknesses for a required reflectance and another application as a non-polarizing rugate filter at 45° of incidence. It was also demonstrated that multiple stop-band rugate reflectors can be designed with this approach by changing the power of the sine between the rugate and the multilayer [37]. On the other hand, the suppression of harmonics in reflectance for multilayer stacks using designs close in profile to the rugate was also shown [38].

Another application of this generalization can be the suppression of side-lobes of rugate filters. In case of normal incidence the optical admittance can be treated as the refractive index and the power-sine formula can be written as follows:

$$n(x) = n_a \sin^p\left(4\pi \frac{x}{\lambda}\right) + n_b \qquad (4.8)$$

Where x is the optical thickness, λ is the center wavelength, n_a is the half of the amplitude of the sine function, n_b is the mean value of the refractive index and p the power which should satisfy $0 \le p \le 1$. For a correct mathematical definition of the equation (4.8), the sine function should be written as:

$$\sin^p(x) = \sin(x) \cdot \left|\sin(x)\right|^{p-1}$$

In the case of *p=1* the function represents the typical rugate filter and in the case of *p=0* the function represents an *HL* multilayer stack, as shown in figure 4.24.

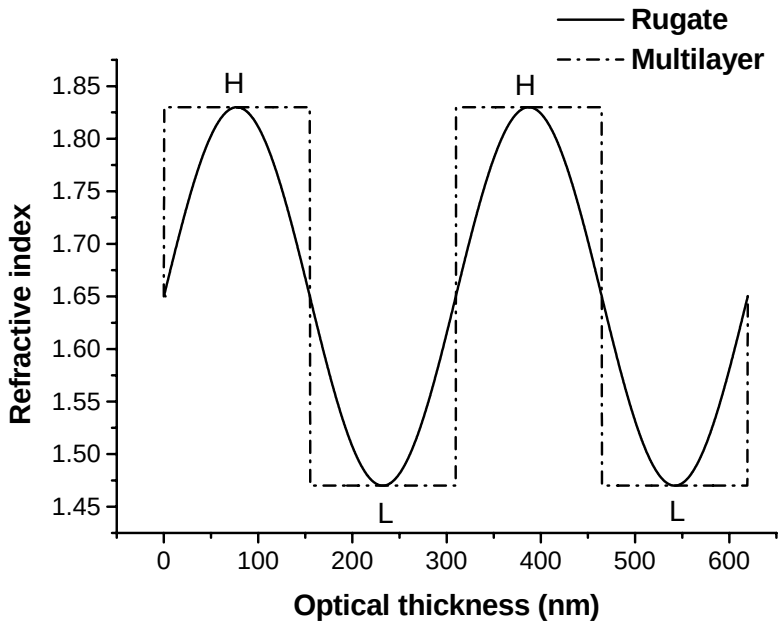

Figure 4.24. Index profile of a rugate filter and a multilayer mirror at 619.5 nm (2 eV) versus optical thickness.

4.7.2.2. Correlation of side lobe suppression between multilayer and rugate filters

The typical solution to remove side-lobes from a multilayer stack is to start and end the deposition by layers of eighth wavelength optical thickness (0.5L or 0.5H) instead of the quarter wavelength (L or H) [39] [a]. Studies showed that the addition of a layer of 0.5L to the top and the bottom of an $(HL)^NH$ stack or 0.5H layers to an $L(HL)^N$ stack, can considerably reduce the side-lobes in the lower or higher wavelengths spectrum respectively, which is suitable for low-pass or high-pass filter designs, as shown in Figure 4.25.

[a] Software based refinement of this layer can be done, depending on the used materials and their refractive index. In our case, we will just show the eighth wavelength addition and its influence, in order to compare it to its equivalent in the rugate filter.

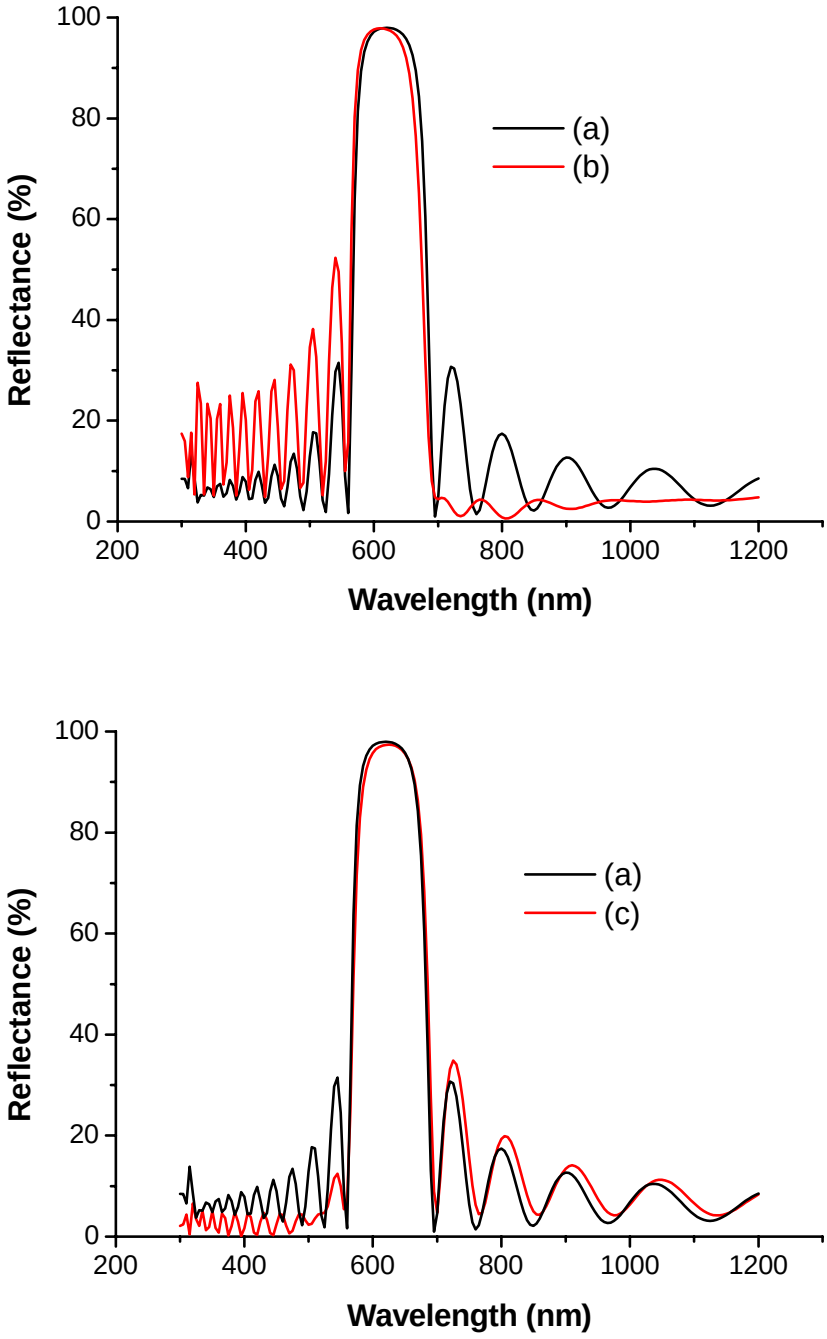

Figure 4.25. Reflectance of different multilayer mirrors for a glass substrate in air medium: (a) *$(HL)^NH$* stack. (b) *$0.5HL(HL)^N0.5H$*. (c) *$0.5L(HL)^NH0.5L$*.

When we use equation (4.8) for the description of a rugate filter or a multilayer stack, the addition of an eighth wavelength optical thickness layer, either of high or low index, to the multilayer mirror will be equivalent to the addition of an eighth or three eighths wavelength optical thickness of the sinusoidal function to the rugate index profile, as shown in Figure 4.26.

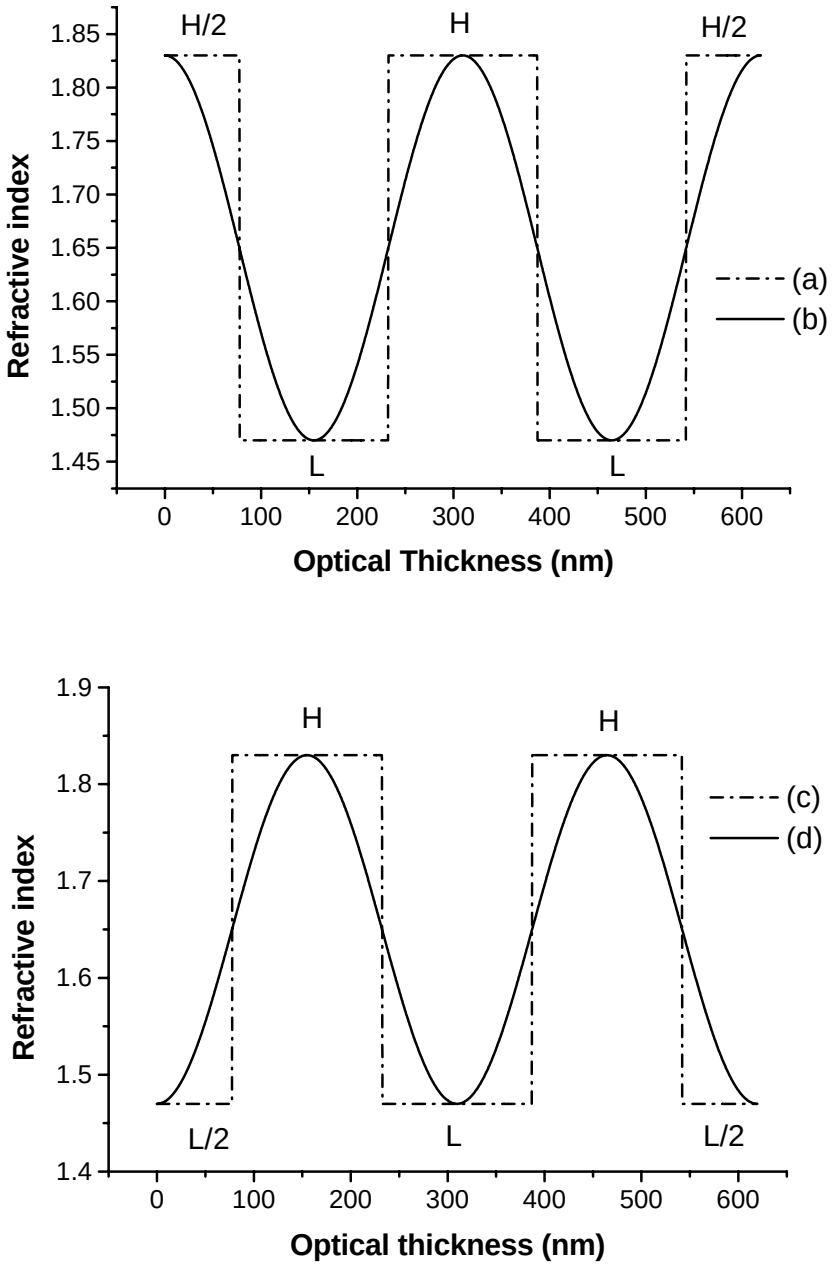

Figure 4.26. Index profiles of : (a) $0.5HL(HL)^N0.5H$. (b) Rugate filter with 3λ/8 and λ/8 layers. (c) $0.5L(HL)^NH0.5L$. (d) Rugate filter with λ/8 and 3λ/8 layers.

As a result, the simulation of the different rugate filters shows reflectance as in Figure 4.27. By comparison to the multilayer stacks, the added layers can be considered as matching layers for the rugate filters as they are extracted from matching layers for the multilayer.

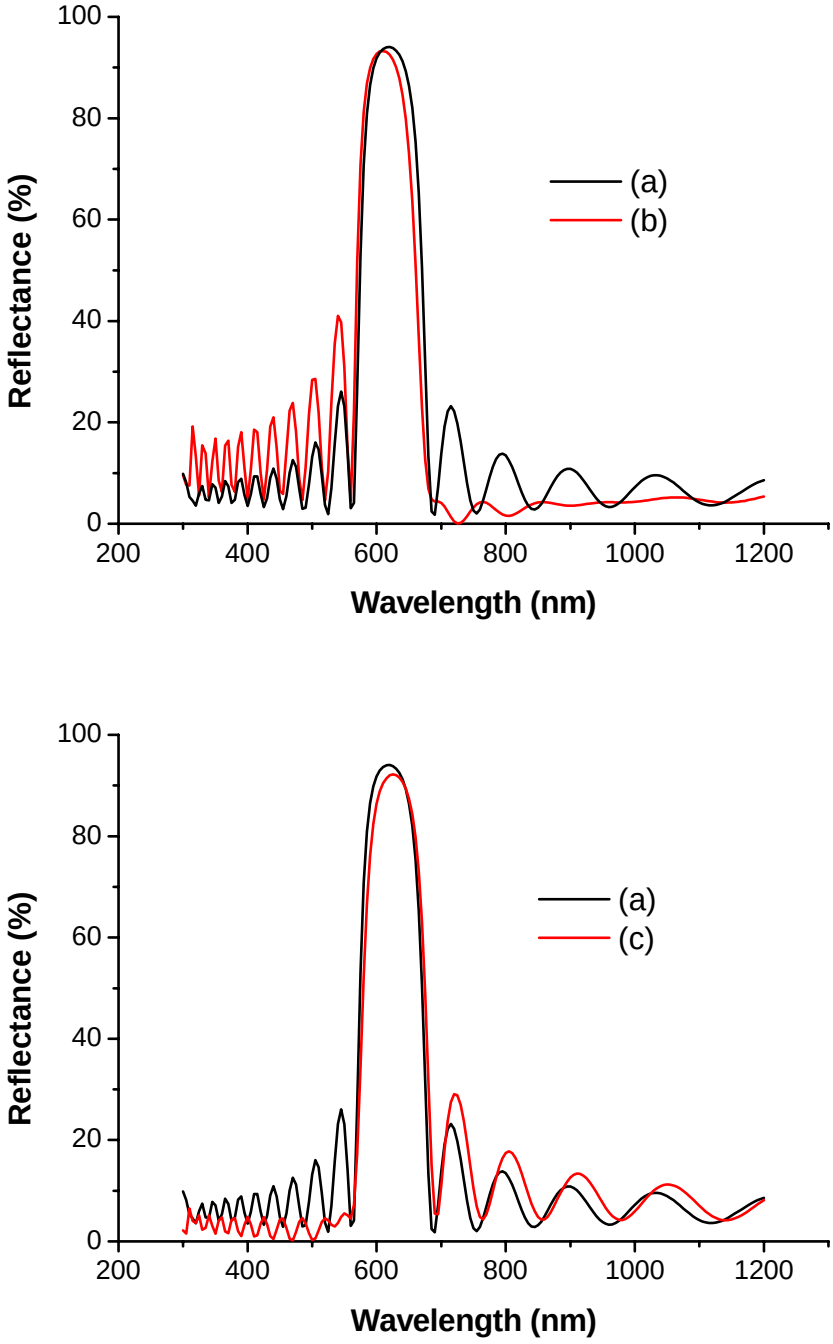

Figure 4.27. Reflectance of rugate filters : (a) typical, (b) with 3λ/8 and λ/8 layers, (c) with λ/8 and 3λ/8 layers.

4.7.2.3. Comparison between a sinusoidal layer and a quintic layer

Further investigation of the previous suggested solutions was done by comparing a conventional quintic layer [36] to a sinusoidal matching layer. For this comparison we suggest an index profile as mentioned in equation (4.8) with a phase shift of $-\pi/2$. This allows us to start the profile at the maximal refractive index. To this profile we add two different sets of layers in two separate designs: a) quintic layers and b) sinusoidal layers. Each is a quarter wavelength optical thickness, varying from the maximal to the minimal values of the refractive index towards the sides of the profile. Figure 4.28 shows the shape of the two matching layers.

By calculation of the spectral reflectance of the two different rugate layers formed each of ten periods and topped by the two previous matching layers, we find the reflectance shown in Figure 4.29. The comparison of the two proves their similarity of behavior for side-lobe suppression in the low wavelength range, moreover the sinusoidal layer is slightly better in the high wavelength range.

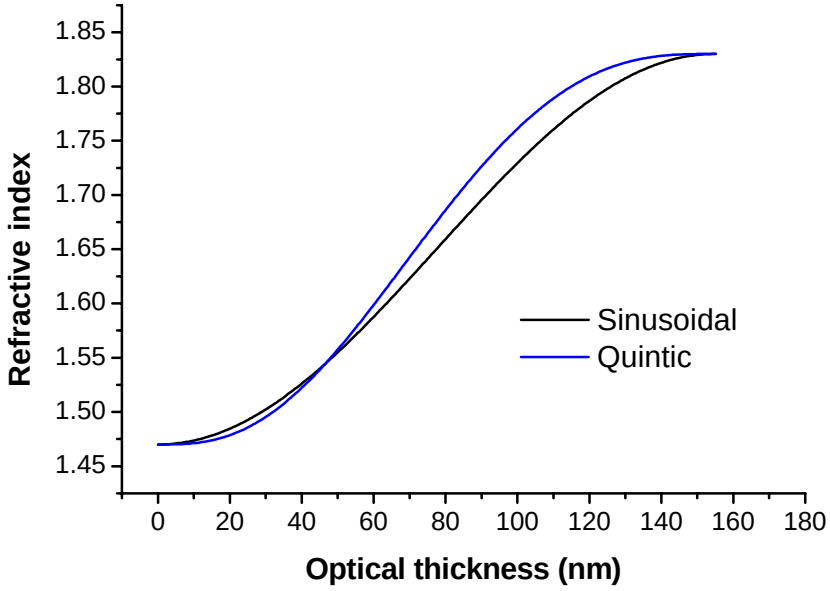

Figure 4.28. Quintic and sinusoidal matching layers.

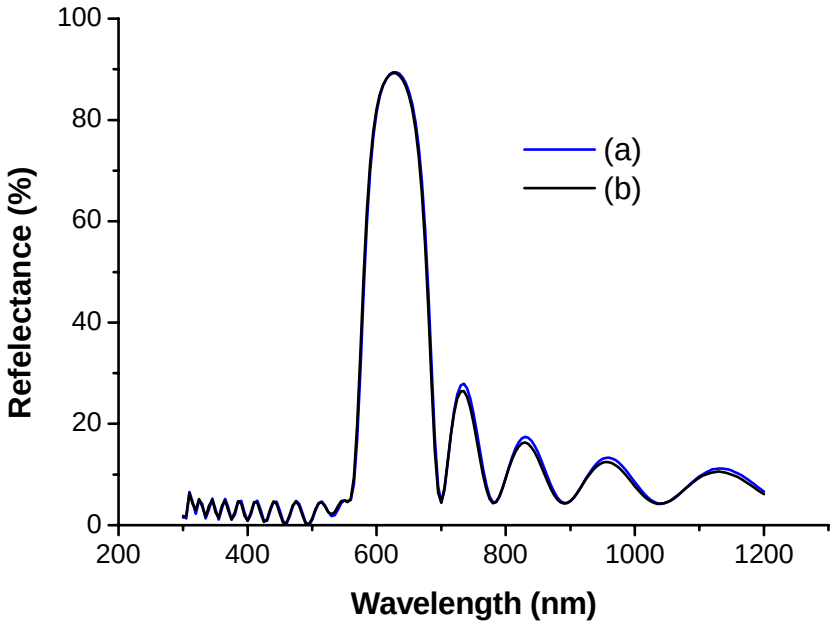

Figure 4.29. Reflectance of: (a) Quintic matched and (b) sinusoidal matched rugate filters.

The same previous behavior was also found in the case where the profile starts and ends at the maximal index, with quintic or sinusoidal layers.

In order to verify this simulation, a rugate filter similar to the one shown in Figure 4.29 was deposited with sinusoidal matching layers.

For the gas flows definition, we follow the same steps as done for the linear gradient layer discussed previously. A single period of a rugate filter at 2eV, of total thickness of 189 nm, is shown in Figure 4.30 with the gas flows as function of thickness, for a constant 5 sccm flow of silane, 1 kW of microwave power, and without RF bias.

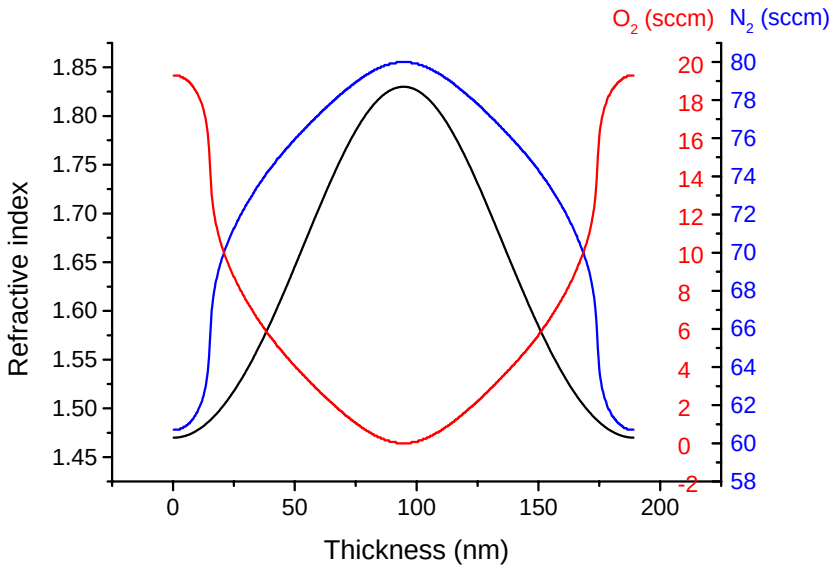

Figure 4.30. Oxidants flow and index profile versus thickness for one rugate period.

By using this set of gas flows, a ten period rugate filter centered at 2eV (~620 nm) was deposited using feed forward deposition. As depicted in Figure 4.31, the resulting wavelength accuracy was very good, with a shift of only 6 nm. The spectral shift can be reduced by improvement of the homogeneity of the deposition. A possible solution might be to lift the central antenna. The reflectivity at the central wavelength was 87%. The slight decrease in reflectance is due to the difference between the deposited and expected silicon nitride refractive index. The theoretical transmission was calculated taking into consideration the dispersion of the substrate only.

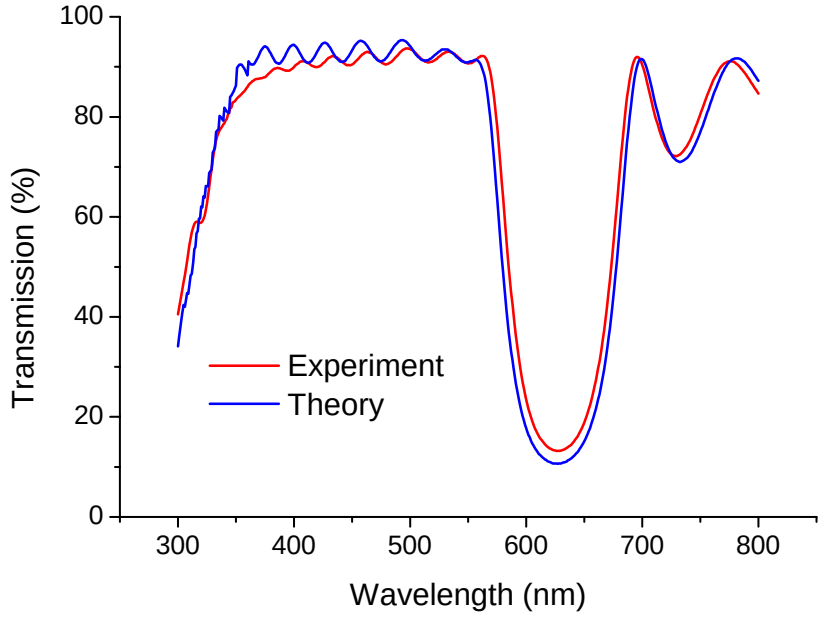

Figure 4.31. Transmission of a sinusoidally matched 10 period rugate filter.

4.8. Conclusion

In this chapter, the deposition of silicon oxynitride alloys was studied. The influence of different process parameters such as precursors flows, antenna configuration, MW power, and RF biasing was analyzed, in order to obtain the material properties in the real deposition conditions. The characterization data of the material showed to be suitable for gradient index films deposition. A gradient index antireflection coating and a rugate filter were deposited in feed-forward mode in order to show the stability of the technology.

We showed the correlation of side-lobe suppression between multilayer and rugate mirrors. We demonstrated the ability to transform an eighth wavelength optical thickness used for side-lobe suppression in multilayer stacks to an equivalent layer in the rugate profile. And we also compared these layers to typical quintic layers used for this purpose.

In the next chapter, more detailed depositions, controlled by multiwavelength kinetic ellipsometry will be shown. Different methods will be explained and compared with the advantages and constraints of each.

References

[1] D. Poitras, S. Larouche, L. Martinu, *Design and plasma deposition of dispersion-corrected multiband rugate filters*, Applied Optics, Vol. 41(25), pp. 5249-5255, (2002).

[2] D. Poitras, L. Martinu, *Simple method for determining slowly varying refractive-index profiles from in situ spectrophotometric measurements*, Applied Optics, Vol. 37(19), pp. 4160-4167, (1998).

[3] M. Kildemo, S. Deniau, P. Bulkin, B. Drévillon, *Real time control of the growth of silicon alloy multilayers by multiwavelength ellipsometry*, Thin Solid Films, Vol. 290-291, pp. 46-50, (1996).

[4] B. Drévillon, *Phase modulated ellipsometry from the ultraviolet to the infrared: In situ application to the growth of semiconductors*, Progress in Crystal Growth and Characteration of Materials, vol. 27(1), pp. 1-87, (1993).

[5] R. Azzam, N. Bashara, *Ellipsometry and polarized light*, North Holland Personal Library, (1970).

[6] S.N. Jasperson, *An improved method for high reflectivity ellipsometry based on a new polarization modulation technique*, Review of Scientific Instruments, Vol. 40, pp. 761-767, (1969).

[7] J.C. Kemp, *Piezo-optical birefringence modulators: New use for a long-known effect*, Journal of Optical Society of America, Vol.59(8), (1969).

[8] S.N. Jasperson, D.K. BurgE, R.C. O'Handley, *A modulated ellipsometer for studying thin film optical properties and surface dynamics*, Surface Science, Vol. 27, pp. 548-558 (1973).

[9] D. Poelman, P.F. Smet, *Methods for the determination of the optical constants of thin films from single transmission measurements: a critical review*, Journal of Physics D: Applied Physics, Vol. 36, pp. 1850-1857, (2003).

[10] G.E. Jellison, Jr., B.C. Sales, *Determination of the optical functions of transparent glasses by using spectroscopic ellipsometry*, Applied Optics, Vol. 30(30), pp. 4310-4315,(1991).

[11] A. Hofrichter, P. Bulkin, B. Drevillon, *Plasma enhanced chemical vapour deposition of SiO_xN_y in an integrated distributed electron cyclotron resonance reactor*, Applied Surface Science, 142, pp. 447–450, (1999).

[12] M.J. Hernandez, J. Garrido, J. Martinez, J. Piqueras, *Compositional and electrical properties of ECR-CVD silicon oxynitrides*, Semicond. Sci. Technol. 12, pp. 927–932, (1997).

[13] A.J. Flewitt, A.P. Dyson, J. Robertson, W.I. Milne, *Low temperature growth of silicon nitride by electron cyclotron resonance plasma enhanced chemical vapour deposition*, Thin Solid Films, Vol. 383, pp. 172-177, (2001).

[14] H. Schlemm, A. Mai, S. Roth, D. Roth, K.-M. Baumgartner, H. Muegge, *Industrial large scale silicon nitride deposition at photovoltaic cells with linear micro-wave plasma sources*, Surface and Coating Technology, Vol. 174-175, pp. 208-211, (2003).

[15] D. Daineka, P. Bulkin, G. Girard, B. Drévillon, *Simple method of gas flow ratio optimization in high rate deposition of SiO2 by electron cyclotron resonance plasma enhanced chemical vapor deposition*, Journal of Vacuum Science and Technology A, Vol. 22, pp.36-38 (2004).

[16] C. Doughty, D.C. Knick, J.B. Bailey, J.E. Spencer, *Silicon nitride films deposited at substrate temperatures <100°C in a permanent magnet electron cyclotron resonance plasma*, Journal of Vacuum Science and Technology A, Vol. 17(5), pp. 2612-2618, (1999).

[17] P.V. Bulkin, P.L. Swart, B.M. Lacquet, *Effect of process parameters on the properties of electron cyclotron resonance plasma deposited slicon-oxynitride*, Journal of Non-crystalline Solids, Vol. 187, pp. 403 – 408, (1995).

[18] S.V. Nguyen, K. Albaugh, *The characterization of electron cylcotron resonance plasma deposited nitride and silicon oxide films*, Journal of the Electrochemical Society, Vol. 136(10), pp. 2835-2940, (1989).

[19] D.F. Lai, J. Robertson, W.I. Milne, *Plasma oxidation of silicon using an electron cyclotron wave resonance (ECWR) oxygen plasma*, Thin solid films, Vol. 383, pp. 220-223, (2001).

[20] J. Zhang, Z. Ren, R. Liang, Y. Sui, W. Liu, *Planar optical waveguide thin films growth by microwave ECR PECVD*, Surface and Coatings Technology, Vol. 131, pp. 116-120, (2000).

[21] W. Miyazawa, S. Tada, K. Ito, H. Saito, S. Den, Y. Hayashi, Y. Okamoto, Y. Sakamoto, *A large-area ECR processing plasma*, Plasma Sources Science and Technology, Vol. 5, pp. 265–267, (1996).

[22] J.A.S. da Matta, R.M.O. Galvao, L. Ruchko, M.C.A. Fantini, P.K. Kiyohara, *Description and Characterization of a ECR Plasma Device Developed for Thin Film Deposition*, Brazilian Journal of Physics, vol. 33(1), (2003).

[23] S. Nakayama, *ECR plasma for thin film technology*, Pure and Applied Chemistry, Vol. 62(9), pp. 1751-1756, (1990).

[24] H. Wu, D.B. Graves, M. Kilgore, *Two-dimensional simulation of compact ECR plasma sources*, Plasma Sources Science and Technology, Vol. 6, pp. 231–239, (1997).

[25] R. Botha, B. Haj Ibrahim, P. Bulkin, B. Drévillon, *Deposition of dielectrics using a matrix distributed electron cyclotron resonance plasma enhanced chemical vapor deposition system*, Article in press, Thin Solid Films, doi: 10.1016/ j.tsf.2006.11.184, (2006).

[26] K. Coates, S. Morrison, S. Naraynan, A. Madan, *Deposition of Silicon Nitride to Improve the Conversion Efficiency of Multicrystalline Silicon Solar Cells*, Proceedings of the 16th European Photovoltaic Solar Energy Conference, Glasgow, p. 1279, (2000).

[27] A. Canillas, A. Pinyol, J. Sancho-Parramon, J. Ferré-Borrull, E. Bertran, *FTIR phase-modulated ellipsometry characterization of hydrogenated amorphous silicon nitride thin films with embedded nanoparticles*, Thin Solid Films, Vol. 455-456, pp. 167-171, (2004).

[28] Z. Chen, K. Prasad, C.Y. Li, S.S. Su, D. Gui, P.W. Lu, X. He, S. Balakumar, *Characterization and performance of dielectric diffusion barriers for Cu metallization*, Thin Solid Films, Vol. 462-463, pp. 223-226, (2004).

[29] A. Bieder, A. Sonnenfeld, P. R. von Rohn, *Uniformity and composition of silicon oxide films on 3D geometries by plasma enhanced chemical vapor deposition*, Thin Solid Films, Vol. 515(4), (2006).

[30] N. Jiang, B. Agius, M. C. Hugon, J. Olivier, M. Puech, Radio-frequency bias effects on SiO2 films deposited by distributed electron cyclotron resonance plasma enhanced chemical vapor deposition, Journal of Applied Physics, Vol. 76, pp. 1847-1855, (1994).

[31] C.K. Carniglia, *Ellipsometric calculations for nonabsorbing thin films with linear refractive-index gradients*, Journal of the Optical Society of America, Vol. 7(5), pp. 848-856 (1990).

[32] H.A. Macleod, *Thin Film Optical Filters*, 2nd edition, Macmillan, New York, (1986).

[33] G. Minott, R. Sprague, B. Shnapi, *Rugate notch filters find use in laser-based applications*, Laser Focus World, (September 2004).

[34] B.G. Bovard, *Rugate filter theory: an overview*, Applied Optics, Vol. 32(28), pp. 5427-5448, (1993).

[35] W.H. Southwell, *Gradient index antireflection coatings,* Optics Letters, Vol. 8 (11), pp.584-586, (1983).

[36] W.H. Southwell, R.L. Hall, *Rugate filter side-lobe suppression using quintic and rugated quintic matching layers,* Applied Optics, Vol. 28 (14), pp. 2949-2951, (1989).

[37] B.G. Bovard, *Graded index rugate filters: power-sine rugate mirrors,* SPIE Proceedings, Vol. 2046, pp.109-125, (1993).

[38] P. Baumeister, *Multilayer reflectors with suppressed higher-order reflectance peaks,* Applied Optics, Vol. 31 (10), pp. 1568-1573, (1992).

[39] P. Baumeister, *Design of multilayer filters by successive approximations,* JOSA, Vol. 48 (12), pp. 955-958, 1958.

Chapter 5

Real-Time Control Using Multi-Channel Kinetic Ellipsometry

The growth control in optical filter fabrication is typically done using either measurements of the total optical thickness (product of ***n*** and ***d***) by reflectometry, or by using physical thickness measurements deduced from the change of a quartz crystal's resonance frequency QCM, assuming a constant and known material density for the entire layer (cf. § 1.4.). However, small fluctuations of the deposition conditions can influence the stability of the refractive index and consequently change the deposition results. The continuous developments of optics and electronics require more information about the deposited material dielectric function, its roughness and its bulk properties. Moreover, increased reproducibility of the deposited layers is also needed. This necessitates the development of more accurate control tools with higher precisions.

Ellipsometry is a suitable technique for control growing layers in real-time, as it offers several advantages:

- A high sensitivity to index and thickness variations.
- As it is an optical method, it has a non-invasive nature which is in principle applicable to every deposition method, including PECVD.
- The possibility of increasing the amount of data by multiplying the number of measurement wavelengths.
- The robustness and stability of the algorithms, with fast acquisition times in the order of one second.
- It gives information about the layer composition and the surface roughness which is an advantage over reflectometry.
- When using a phase-modulated ellipsometer, the high frequency of the data acquisition will help to reduce the noise added by external factors.

In this Chapter, we will focus on:

- The calibration and utilization of the multi-channel kinetic ellipsometer.
- The inverse problem in ellipsometry and previous attempts to resolve it.
- Control of depositions done during this study.

The use of deposition control of dielectric layers is not exclusively restricted to optical filters. It can be applied to any process where precision of the thickness and index or the dielectric properties is required, such as flat panels and semiconductor circuits.

5.1. Kinetic Ellipsometry

The calibration parameters of kinetic ellipsometry have previously been studied in detail. However, for in-situ control during growth in real experimental conditions, these parameters require further investigation. While the sensitivity of ellipsometry is a big advantage, it can also be a disadvantage if the secondary signal sources are not considered. The objective of this section is to improve our understanding of these parameters and take them into account during measurements to ensure that they are not a disturbing factor.

5.1.1. Kinetic Ellipsometry Calibration

The phase modulated ellipsometer described in §3.1 can be used *in situ* in kinetic mode to measure simultaneously the variations of the ellipsometric parameters on all (or some of) its channels. The adaptation of Uvisel for the growth control in the reactor Venus implied a basic programming of the data acquisition. The procedure includes communication with the ellipsometric server via a TCP/IP protocol, collecting the data and taking into consideration the calibration parameters.

Since the system is highly sensitive to small variations it must be nearly perfectly calibrated. The calibration is done using DeltaPsi software to generate a file of calibration parameters, which is used later under the control software.

For each wavelength, I_c and I_s can be written as follows[a]:

$$I_c = \frac{\left(\frac{S_{2\omega}}{2T_2J_2}\right)\cos\delta_0 - \left(\frac{S_{\omega}}{2T_1J_1}\right)\sin\delta_0}{1 - J_0\left(\frac{S_{2\omega}}{2T_2J_2}\right)} \qquad (5.1)$$

$$I_s = \frac{\left(\frac{S_{\omega}}{2T_1J_1}\right)\cos\delta_0 + \left(\frac{S_{2\omega}}{2T_2J_2}\right)\sin\delta_0}{1 - J_0\left(\frac{S_{2\omega}}{2T_2J_2}\right)} \qquad (5.2)$$

Where S_ω and $S_{2\omega}$ are the normalized signals ratioed to the continuous signal S_{dc}:

$$S_{\omega} = \frac{S_1}{S_{dc}} \qquad (5.3)$$

$$S_{2\omega} = \frac{S_2}{S_{dc}} \qquad (5.4)$$

J_0, J_1 and J_2 are Bessel functions at the modulation amplitude value, T_1 and T_2 are the transmission coefficients of the two harmonics and δ_0 is the residual birefringence.

All the fitting and inversion methods will be applied directly to I_s, and I_c. The ellipsometric parameters ψ and Δ can be easily deduced from their definitions when needed (Equations 4.4 and 4.5).

[a] These formulas were taken from Jobin Yvon document *Calibration multi-lambda généralisée*, by Razvigor Ossikovski. They were verified by comparison with spectroscopic measurements done using DeltaPsi software.

5.1.2. Influence of The Plasma Emission

The ellipsometric calibration is normally performed in the absence of plasma where low environmental stray light can be neglected. In the case of high background emission, as is the case during deposition, two possible solutions exist: one is to measure the background emission for each step, which will slow down the control process. The second solution is to take into account the change in the S_{dc} signal for several specified wavelengths influenced by the plasma emission. In the latter case, the plasma emission is measured at the start of the deposition and assumed constant during the entire growth process.

For both these scenarios, the harmonic signals become:

$$S_{\omega} = \frac{S_1}{S_{dc} - S_{dc,plasma}} \qquad (5.5)$$

$$S_{2\omega} = \frac{S_2}{S_{dc} - S_{dc,plasma}} \qquad (5.6)$$

In order to show the influence of the plasma emission on the signal, the ellipsometry measurements were performed in the presence of O_2 and N_2 plasmas. OES measurements of the two plasmas were taken. In Figure 5.1 we can see that the oxygen plasma emission is low in the greater part of the spectrum except at specific wavelengths, while the nitrogen plasma emits over a broad part of the spectrum. To confirm the influence of the plasma emission has, multi-channel kinetic ellipsometry measurements were taken in both of these plasmas. In the case of the oxygen plasma the emission influences only the 235 nm channel as shown in Figures 5.2, which was not visible in the OES spectrum due to the absorption of the used fiber. The influence of the nitrogen plasma was, as expected, on almost all of the channels, as depicted in Figure 5.3. Further measurements taken during depositions using SiH_4 and O_2 gas mixtures, are also shown in Figures 5.4 and 5.5. They demonstrated the plasma emission's influence on additional wavelengths. These channels are avoided in Section 5.3, where different examples of optical layer control will be discussed.

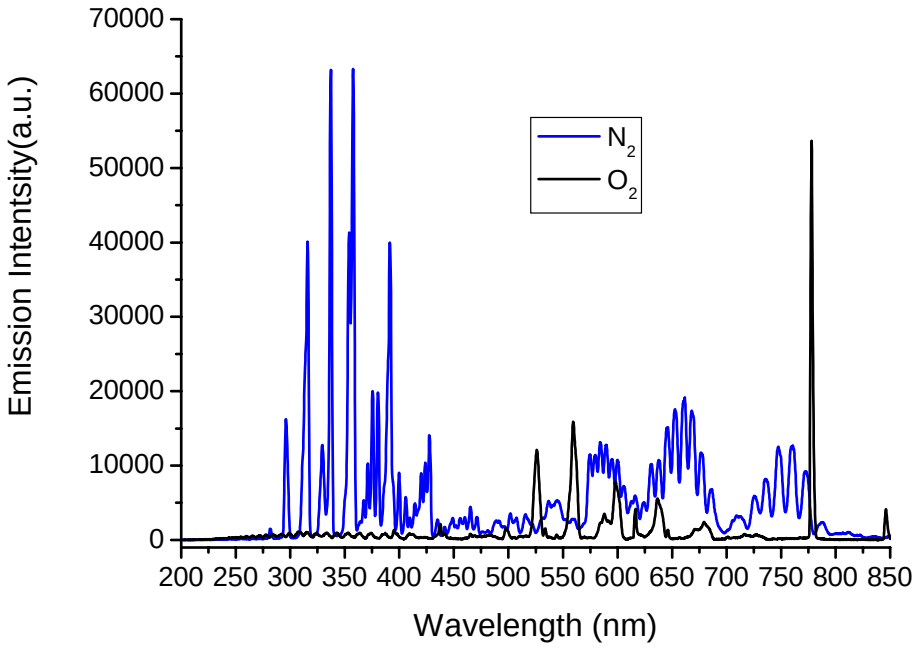

Figure 5.1. Optical emission of N_2 and O_2 plasmas.

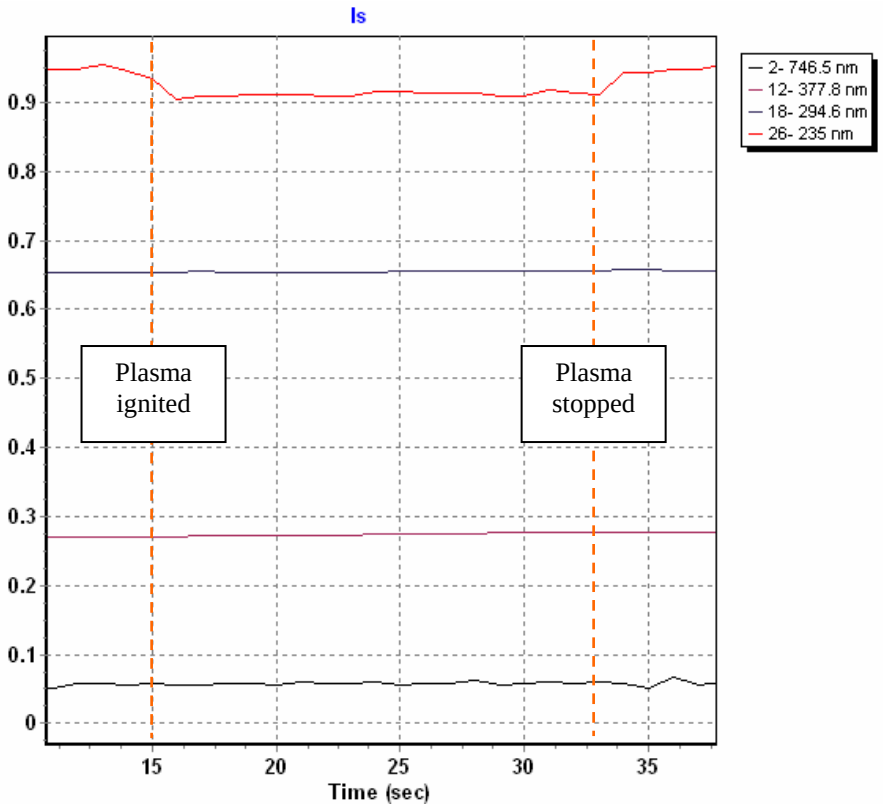

Figure 5.2. Changes in the ellipsometric parameter I_s when igniting and extinguishing an O_2 plasma.

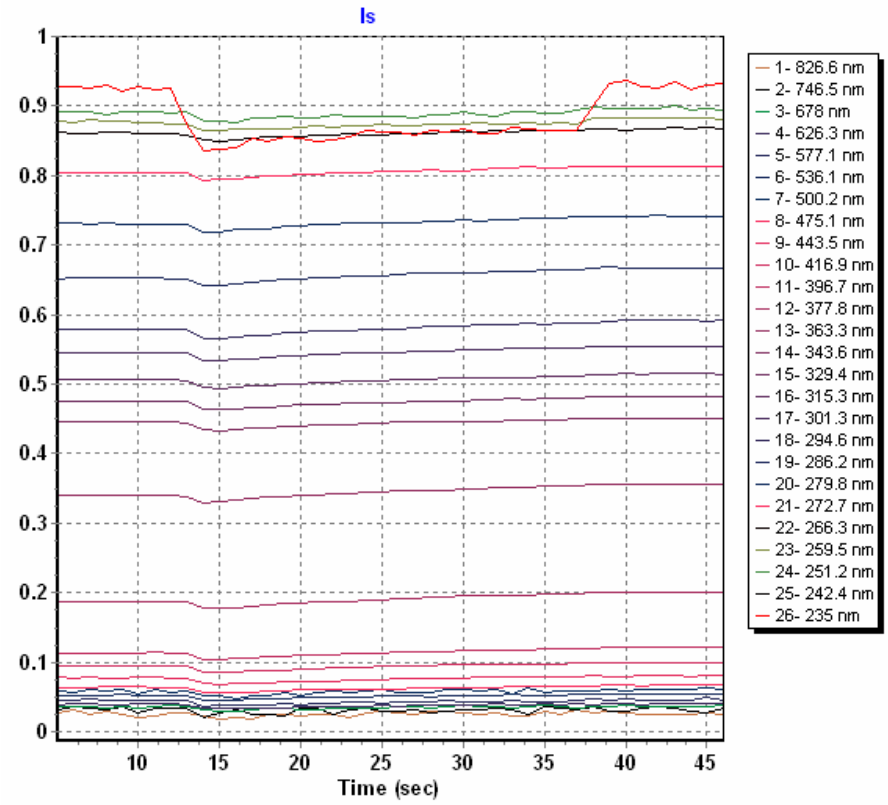

Figure 5.3. Ellipsometric parameter changes when igniting / extinguishing an N_2 plasma.

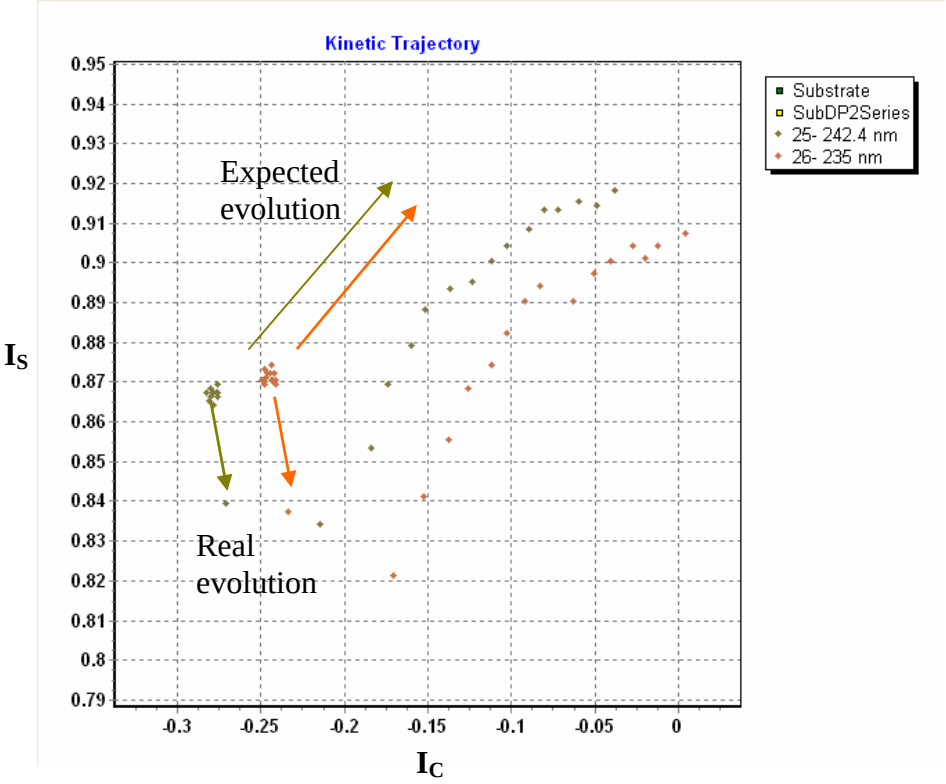

Figure 5.4. Change of the expected evolution of the trajectories by emission of SiH_4 / O_2 plasma.

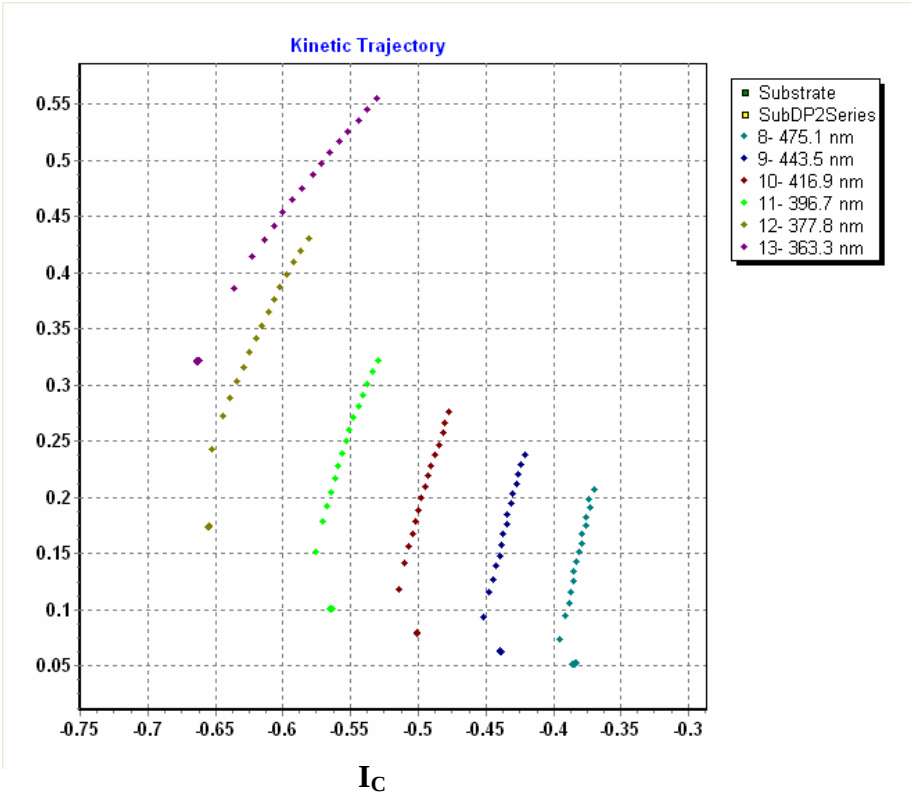

Figure 5.5. Influence of an SiH_4 / O_2 plasma.

5.1.3. Influence of the Heat Flux onto the Substrate

The influence of substrate heating due to the plasma might not seem to be very important at first glance, as the variation of the temperature is small during short periods of time. For long depositions this variation becomes more pronounced and the use of a model that takes substrate temperature variations into account is required when starting the deposition at room temperature. On the contrary, when depositing on a heated substrate, the change of the substrate index should be taken into account for the simulation.

Figures 5.6 and 5.7 show the change of the ellipsometric parameters for a crystalline Si substrate heated to 150°C during two hours. This variation can not be neglected as was done during previous studies. The channels in the near infrared (826 and 756 nm) must be ignored as they illustrate a low signal to noise ratio caused by the heated substrate.

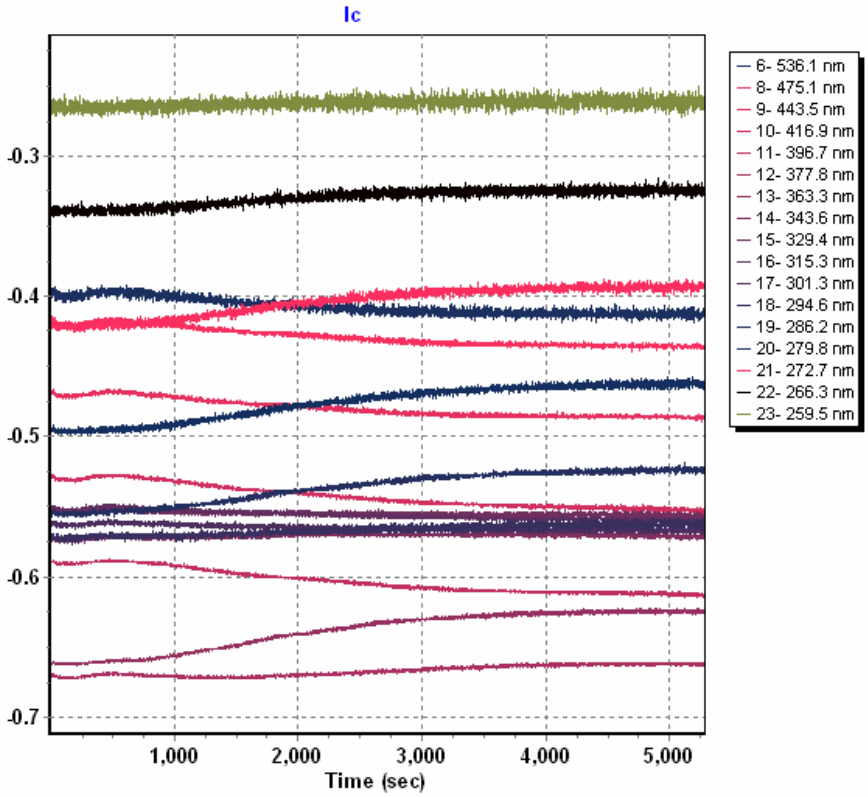

Figure 5.6. Influence of heating a c-Si substrate to 150°C on I_C.

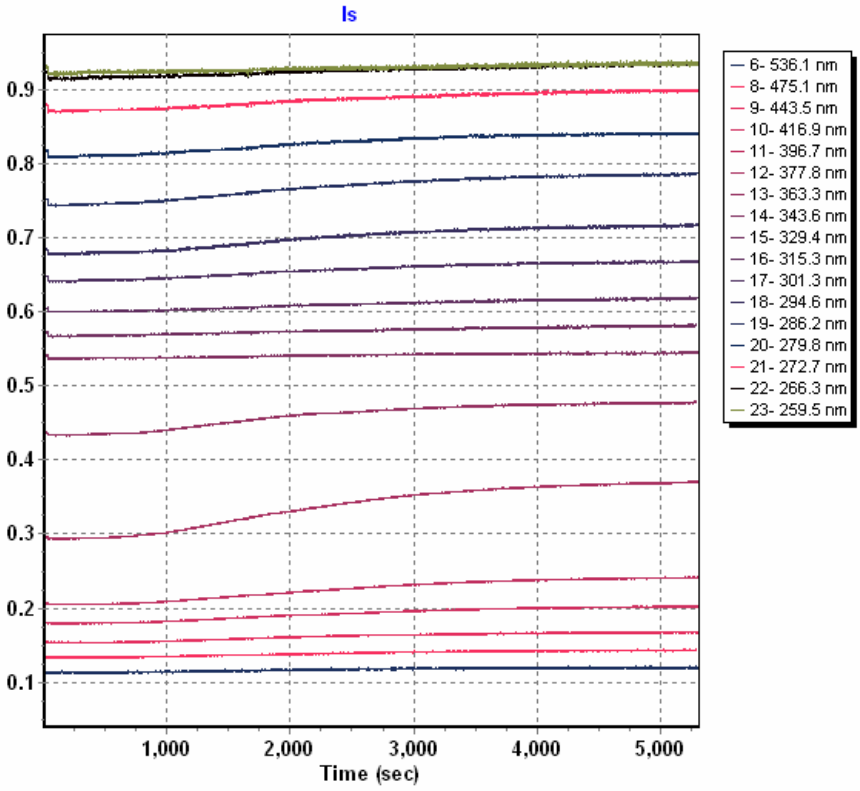

Figure 5.7. Influence of heating a c-Si substrate to 150°C on I_S.

In the previous part we discussed the experimental parameters, which influence our measurements. In order to ensure accurate growth control, the above mentioned parameters need to be modeled or taken into account to avoid their influence. This can be done by selectively choosing the channels uninfluenced by the plasma emission, and by pre-heating the substrate.

5.2. Methods for Controlling Layer Thickness And Refractive Index

Previous work done on the thickness and index control includes two different approaches: In trajectory control methods, a start-stop control based on the comparison of pre-calculated trajectories with measured ones is used, whereas direct inversion methods attempt to calculate the index and thickness in real time [1-4]. Most methods are developed for single wavelength use, and can sometimes be expanded to multi-wavelength applications with relative ease. In kinetic ellipsometry, each acquisition channel produces two values (I_c and I_s) in relation to a deposited layer of three unknowns: n, k and d (cf. § 1.1.). Since the physical thickness d is the same for all the channels, for m channels we have in total $2m+1$ unknowns with $2m$ data. Indeterminism is the governing rule in this case of inverse problem. This necessitates the use of fitting algorithms with convenient mathematical tools in order to obtain convergence and stability. The electronic noise created during measurements can add an additional constraint to the problem and noise reduction methods must be used.

5.2.1. Trajectory Control Methods

Trajectory control methods use the ellipsometric trajectory of a deposition in the (Ic, Is) plane. Simulated and experimental data are then compared in order to estimate the current position in the growth process. It is based on the evaluation of the minimum square difference between the target and the current deposition. Two different approaches can be used.

5.2.1.1. Trajectory Distance Method

In this method [1-3], the target points which represent the end of each layer on the ellipsometric trajectory (I_s^{th},I_c^{th}) for the expected index value and the required thickness, are predefined by calculation using the matrix formalism mentioned in §1.3. For each layer, the stop condition on a single wavelength is to have a null distance between the current point and the target point. The predefined trajectory is calculated before the deposition and after measurement of the substrate spectrum. With multi-wavelength control, we consider the sum of the distances across all channels for each layer:

$$\chi^2 = \sum_{i=1}^{N} \left\{ I_S^{\exp}(\lambda_i) - I_S^{th}(\lambda_i) \right)^2 + \left(I_C^{\exp}(\lambda_i) - I_C^{th}(\lambda_i) \right)^2 \right\} \qquad (5.7)$$

Thus, we stop the deposition when the minimum of this quadratic sum is reached. The method can be used for thickness control when the index is well known. Its principle is explained in Figure 5.8 below. An example of a deposition using this method for thickness control is shown in Figure 5.9. The risk in using this method is stopping too early due to a local minimum in the trajectory. This is explained in Figure 5.10, where the distance method observes a local minimum to be closer to the target endpoint than to the next points in the trajectory. For this reason the use of an estimate of the deposition time, or combination of this method with another control method, is required. Another disadvantage is its sensitivity to the substrate index. Small errors in the substrate index estimation or changes in the substrate temperature can make this approach unstable.

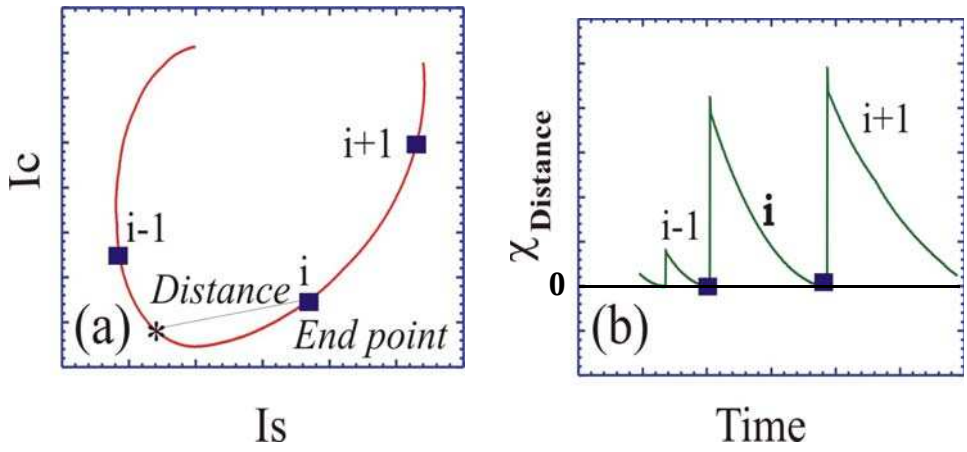

Figure 5.8. Kinetic trajectory for one channel and distance control of each layer.

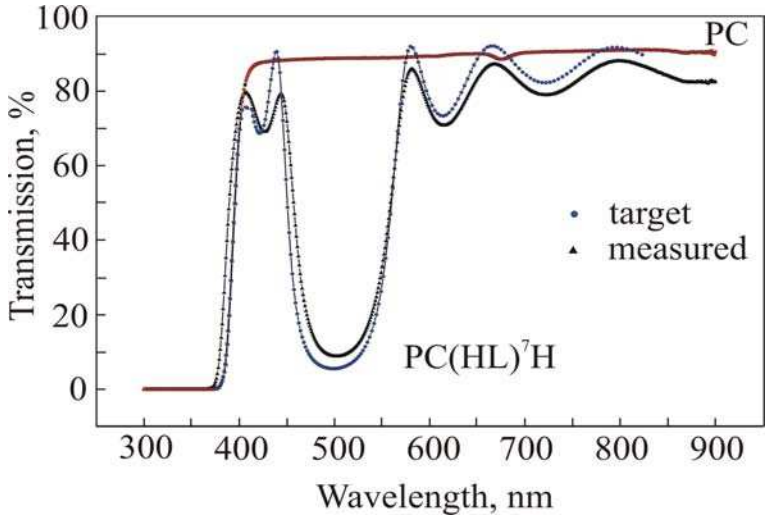

Figure 5.9. A multilayer Bragg mirror deposited on Polycarbonate as in [2].

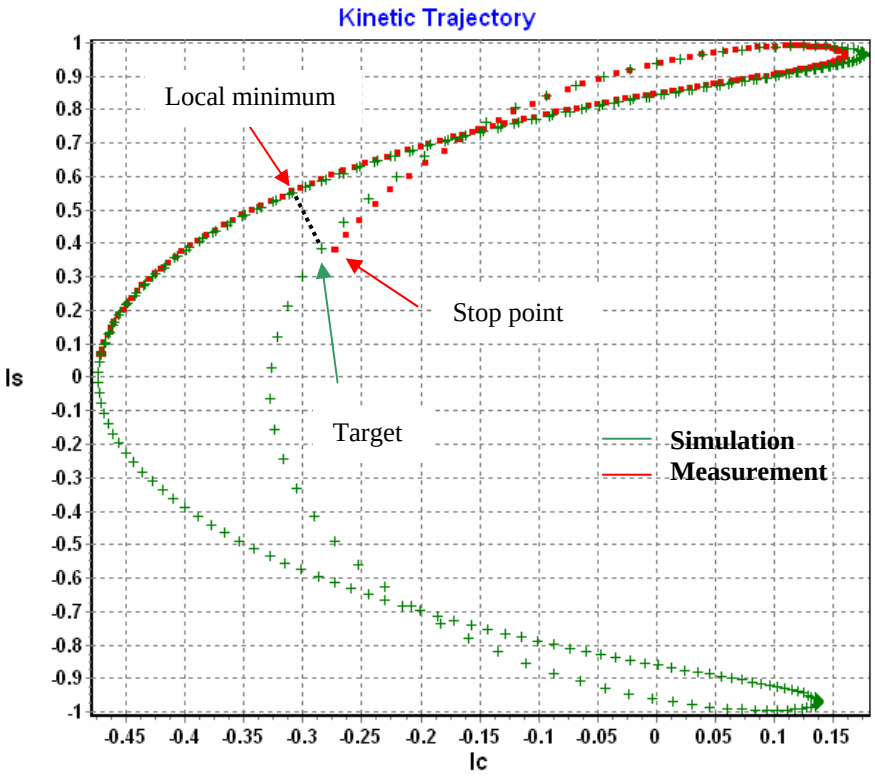

Figure 5.10. Example of a local minimum in the distance method for a silica layer.

5.2.1.2. Trajectory length method

In the trajectory length approach [2, 4] one pre-calculates the length of the ellipsometric trajectories of each layer before the deposition. This is done after measurement of the substrate before deposition. The stop condition during the deposition is the closest point to the target length for each monitoring channel. The advantage of this method is its low sensitivity to errors in the substrate index estimation, since it deals only with the trajectory length. On the other hand, as for the previous technique, it relies on foreknowledge of refractive indices. An additional condition is implemented that only allows stopping after 80 percent of the trajectory at any monitoring wavelength for the current layer is completed. Figure 5.11. shows this operation principle.

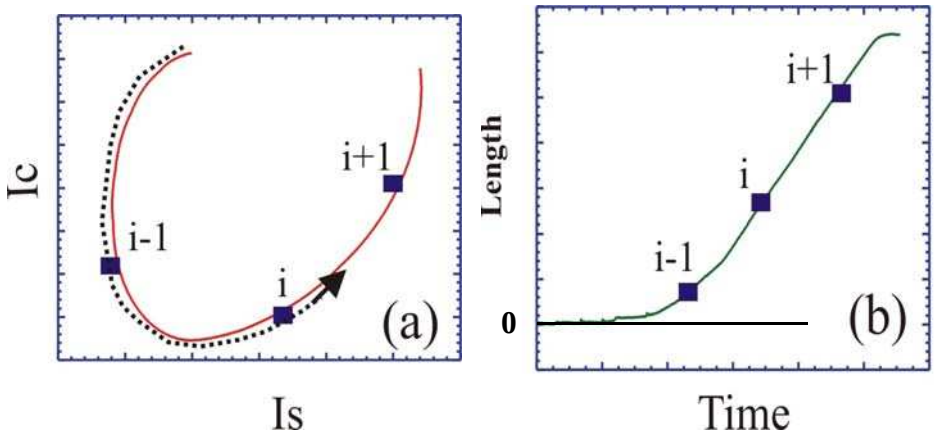

Figure 5.11. Principle of trajectory length control.

5.2.2. Direct Numerical Inversion Method

The disadvantages of the ellipsometric trajectory methods, the main of which is an assumed certainty of the refractive indices of the layers, can be avoided by using directly calculated index and thickness (or growth rate) values [1, 5, 6]. Two main approaches are used.

The main idea in this method is to develop an Abelès matrix of the current superficial layer into Taylor polynomials of the second order [4], since the change in the phase $\delta\varphi$ is small for one step[a]. The developed matrices can be written as follows (cf. Equations 1.2 and 1.5):

$$dM_S \approx \begin{pmatrix} 1-\frac{1}{2}k^2\left(\varepsilon-\alpha^2\right).dx^2 & ik.dx \\ ik\left(\varepsilon-\alpha^2\right).dx & 1-\frac{1}{2}k^2\left(\varepsilon-\alpha^2\right).dx^2 \end{pmatrix} \qquad (5.8)$$

$$dM_P \approx \begin{pmatrix} 1-\frac{1}{2}k^2\left(\varepsilon-\alpha^2\right).dx^2 & ik\left(1-\frac{\alpha^2}{\varepsilon}\right).dx \\ ik.\varepsilon.dx & 1-\frac{1}{2}k^2\left(\varepsilon-\alpha^2\right).dx^2 \end{pmatrix} \qquad (5.9)$$

Where ε is the dielectric function taken to be constant during the current elementary layer, α is the effective index ($n_i sin\theta_i = \alpha$), $k = 2\pi/\lambda$ is the angular wavenumber, and dx is the elementary thickness change.

The matrix product for the two polarizations for the current step is (from Equation 1.6.):

$$M_N = dM.M_{N-1} \qquad (5.10)$$

By writing Fresnel's reflection coefficients for the two polarizations *s* and *p* (from Equations 1.8 and 1.9), the variation of I_S and I_C can be written as a function of dx and dx^2 multiplied by polynomials in ε of known coefficients:

$$dI_C = A_C(\varepsilon)dx^2 + B_C(\varepsilon)dx \qquad (5.11)$$

$$dI_S = A_S(\varepsilon)dx^2 + B_S(\varepsilon)dx \qquad (5.12)$$

[a] For a control wavelength of 500 nm, a deposited refractive index of 1.5, a growth rate of 0.5 nm/s and an angle of incidence 70°, the order of the phase change per second is: $\delta\varphi = \frac{2\pi}{\lambda}\sqrt{(n^2 - {n_0}^2 \sin^2\theta_0)}.dx \approx 0.007$

From these equations a polynomial equation of the 8th order in ε will result. The solutions of this equation are filtered to exclude the non-physical values of ε and dx. Only relevant values with choices close to the expected ones are kept. Finally the mean value of dx is calculated for the different wavelengths of control. Figure 5.12 depicts a previously done, post-treatment of measurements of the ellipsometric parameters by this method for a linear gradient profile deposited between two constant index layers. Comparison with spectroscopic ellipsometry, as shown in Figure 5.13, proved a good agreement with the thickness found by kinetic ellipsometry inversion, in the order of 1% of difference on a 300 nm layer.

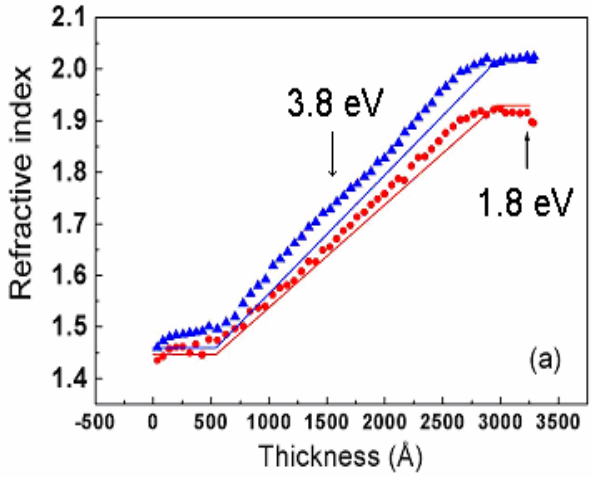

Figure 5.12. Reconstruction of the refractive index for a linear gradient profile using the direct numerical inversion on post-treated measurements, published in [1].

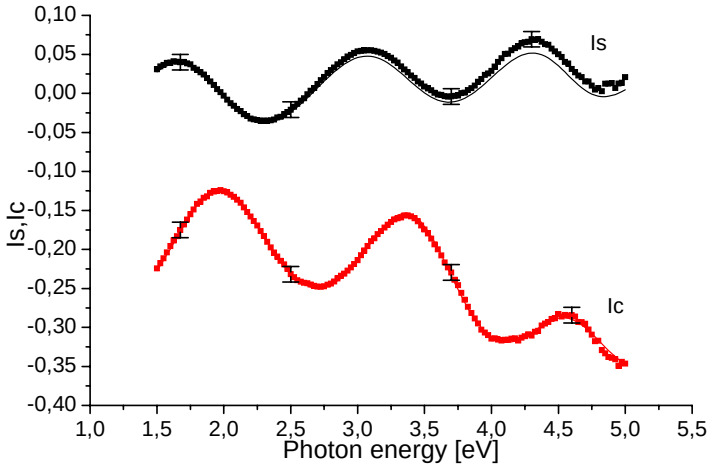

Figure 5.13. Spectroscopic ellipsometry fit between the theoretical model and the measured data in [1].

This method showed good accuracy in post treatment of gradient index layers. It is not stable at the index discontinuities of a multilayer. Moreover, it did not provide good accuracy in real-time, probably due to the need to develop the Abélès matrix elements to a higher order.

5.2.3. Real-time Least Square Fit

This approach was implemented in the PICM laboratory for the control of multilayer stacks of constant refractive index [1]. It consists of least square fitting using several rules:

- Parallel treatment of multi-channel ellipsometric data without use of a dispersion relationship.
- Eliminating the noise origin by only accepting data changes in the order of double the noise level.
- In order to lower the divergence risk, the fit is done on the thickness. Only in case of insufficiency of this fit, indicated by a maximum value of χ^2, a simultaneous fit on n and k is done.
- In order to eliminate noise and stabilize the algorithm, a sliding window of a specific length is used with a second order polynomial approximation inside it.

Examples of filters grown using this method, taking into account the factors mentioned in §5.1, will be discussed in the subsequent section in order to show its importance and capabilities.

5.3. Optical Layer Control by Real-Time Least Square Fit

5.3.1. Thickness Control of a Single Layer

In several situations control of a single layer can be very important, as is the case for the optical thickness of the intermediate layer of a Fabry-Perot filter. Here, the optical thickness should be accurately controlled in order to have constructive interference in transmission.

A Fabry-Perot filter based on two rugate mirrors at 660 nm, composed of 10 periods each (cf. § 4.7.2) with an intermediate constant index oxynitride layer having an optical thickness equal to 3λ/2 was manufactured. Only the intermediate layer was controlled, using the least square fit technique. The rugate filters were successively feed-forward deposited by time control as was previously shown in Figure 4.28.

The design and control was primarily done for an intermediate layer of silica-like oxynitride with a refractive index 1.46 and an oxidants flow ratio of $O_2/(O_2+N_2)=0.25$. In order to simulate the departure of the process from the required conditions, the flow ratios were changed to $O_2/(O_2+N_2)=0.14$ during deposition. In this case the index is expected to increase to approximately 1.52.

The expected programmed thickness for the oxide layer is:

$$d_1=\frac{3\lambda}{2n_1}=677.6nm \tag{5.13}$$

When depositing, using the thickness fit, an auto-correction of the optical thickness is done between the two trajectories corresponding to the simulated and measured materials.

When the layer thickness, calculated on the basis of the expected index (and not the actually deposited one), reaches the value 677.6 nm, it in reality has a different index and consequently different thickness, but the real value of the optical thickness remains the same:

$$n_2 d_2 = \frac{3\lambda}{2} \qquad (5.14)$$

Therefore in this case, the deviation of the refractive index of the layer does not influence the total optical thickness and the real deposited physical thickness can be calculated from it.

The principle of optical thickness auto-correction with the fit on thickness used for the previous layer is shown in Figure 5.13. The transmittance of the deposited Fabry-Perot filter can be seen in Figure 5.14.

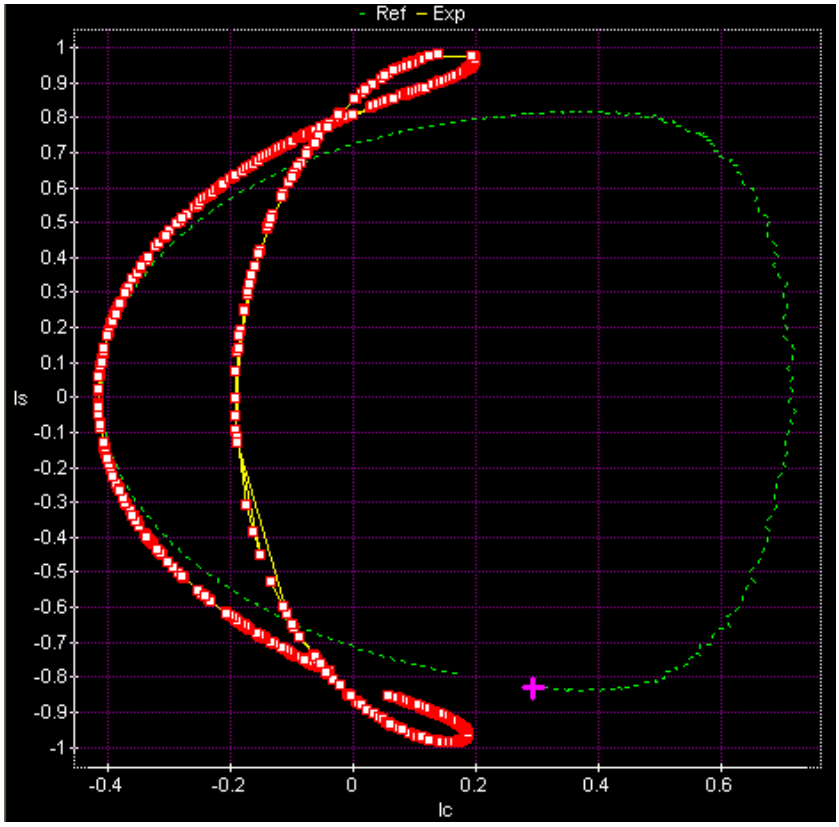

Figure 5.14. Fitted and measured trajectories for thickness control of one layer.

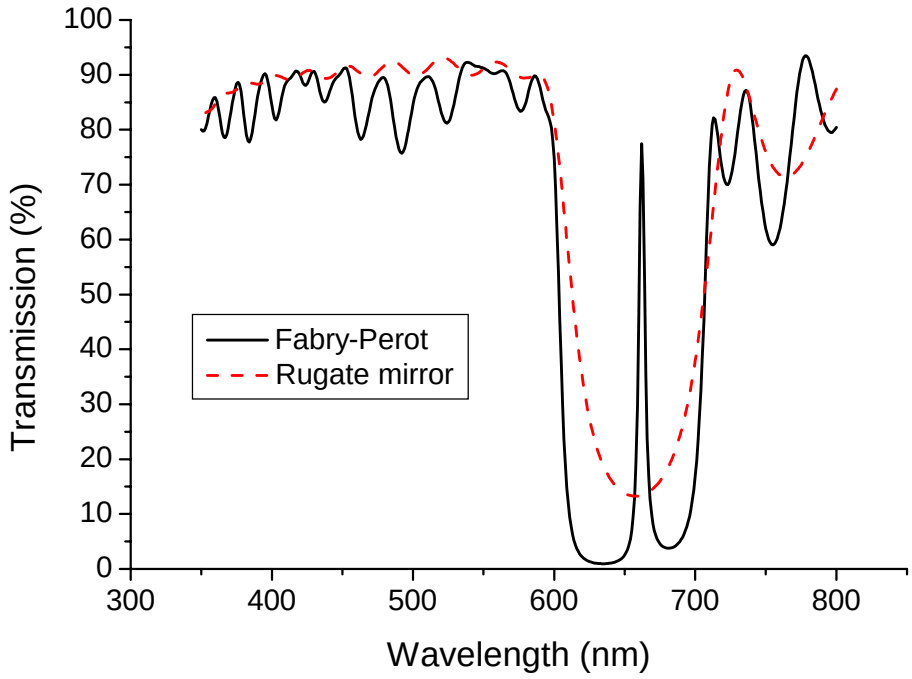

Figure 5.15. Transmission of a Fabry-Perot at 660 nm, made of two feed-forward rugate filters and an intermediate SiO_xN_y constant index layer controlled by fitting on the thickness.

5.3.2. Thickness Control of Two Layers *HL*

In periodic structures such as the Bragg mirror, the focus of control is on the optical thickness of the *HL* deposited sequence, which allows one to achieve a high reflection at the required wavelength. The change in the refractive indices while controlling the optical thickness and the reproduction of the same *HL* sequence, will influence the width of the reflection band and the value of the reflection at the specified central wavelength.

Let us consider the multilayer $(HL)^N H$ Bragg mirror. We need to perfectly characterize the couple *HL* to have a good accuracy in wavelength with good reflection. Moreover, the typical solution to remove the ripples in the transmission part is to add a $\frac{1}{2}L$ layer at the end of the deposition.

The optical control of this layer in single wavelength reflectometry, for example, necessitates changing the control wavelength to the half of the target wavelength, which will create a constraint caused by the dispersion of the material, since it can not always be known perfectly.

We therefore deposited an *HL* sequence at 660 nm, controlled by thickness fit under multi-wavelength kinetic ellipsometry. The auto-correction of the optical thickness explained in §5.3.1 was verified while depositing the two layers. The deposition times related to the required thickness of the two layers were precisely measured. Figure 5.16 shows the kinetic ellipsometry trajectory in the fit and the measurement. The white line in the bottom indicates the *H* to *L* transition on the trajectory.

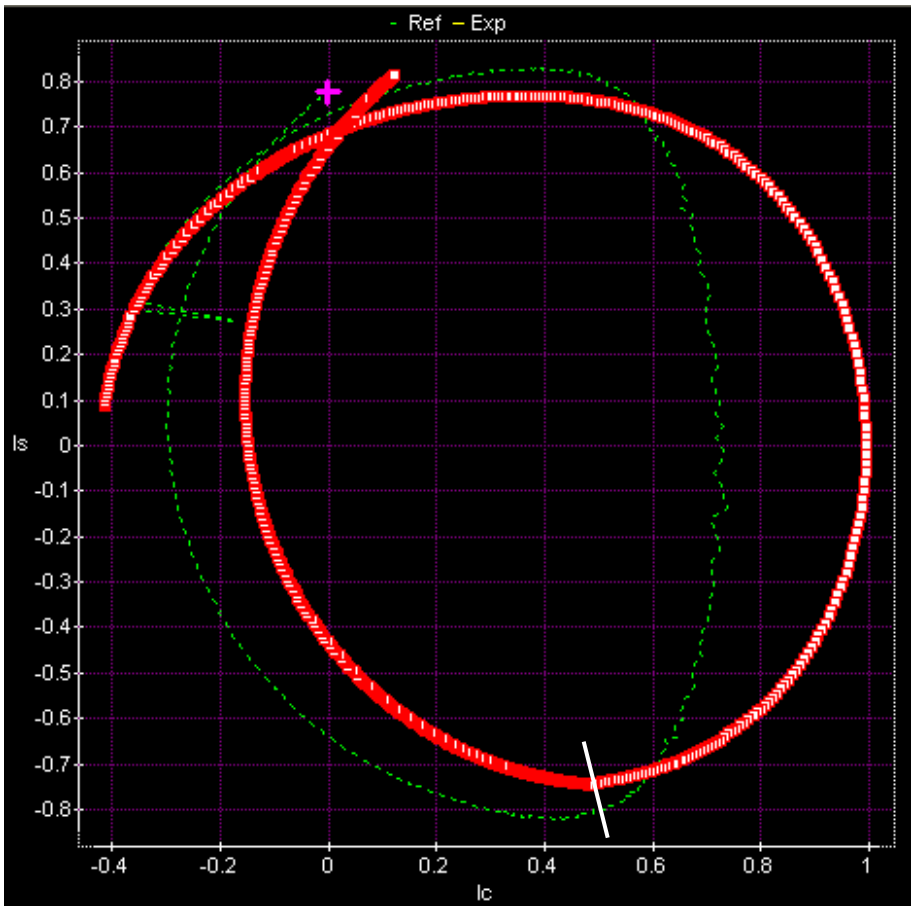

Figure 5.16. Kinetic trajectories at 2 eV of the *HL* layers.

The rest of the filter composed of a total of $(HL)^{12} H \frac{1}{2} L$ layers was deposited by reproducing the time for the first two deposited *HL* layers. After spectroscopic transmission measurements, the mirror showed a very good agreement with the expected theoretical reflectance in the position of the central wavelength of rejection, whereas the bandwidth and rejection value are somewhat lower than those for the designed filter due to a slightly lower refractive index of the grown nitride, as shown in Figure 5.17. A photograph taken of the deposited filter can be seen in Figure 5.18. The red color on the black background shows the color in reflection, whereas the sky blue color on the white background shows the complementary in transmission after scattering from the white paper.

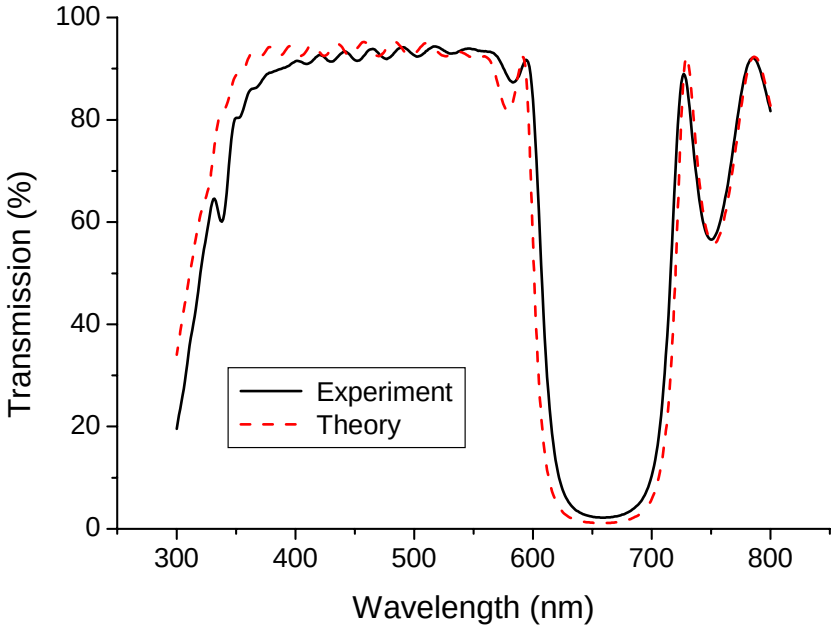

Figure 5.17. Experimental and theoretical transmission of an *(HL)^{12}H 0.5L* mirror.

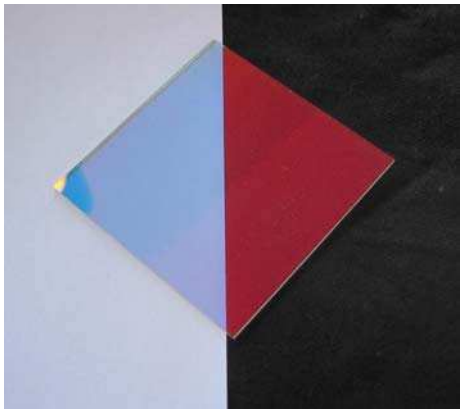

Figure 5.18. An *(HL)^{12}H 0.5L* filter.

5.3.3 Thickness and Index Control of a Three Layer *MHL* AR Coating for the Visible Range

In some non-periodic structures, precise knowledge of the index is of utmost importance, as any change in the refractive index can considerably decrease the quality of the resulting filter, even if the optical thickness is controlled as in the previous sections, where a lower or higher refractive index could be compensated for by increasing or decreasing the thickness, respectively.

As mentioned in § 5.2.3, the fit on index is added only in the case where the fit on the thickness does not give an adequate fit. The principle of this fit is shown in Figure 5.19.

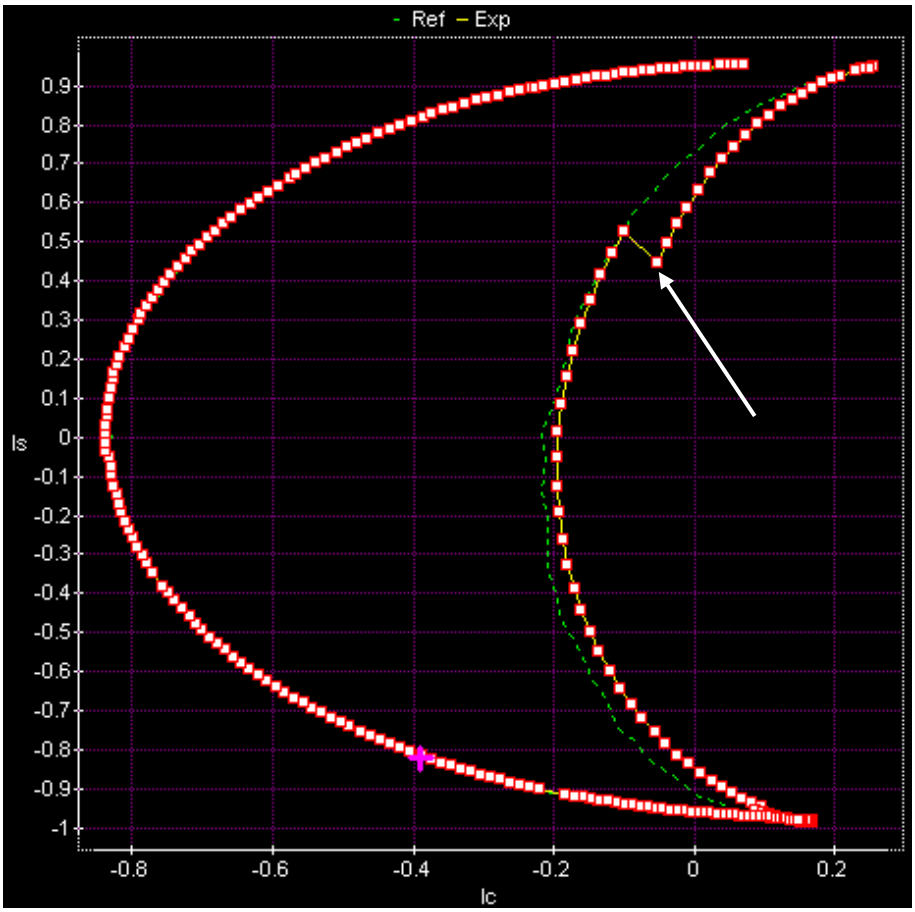

Figure 5.19. An example of an index fit on a silicon nitride layer at 1.7 eV.

In order to demonstrate the importance of the index fit, we used as a starting design an antireflection coating of three layers *MHL*. The design was modified in order to allow the use of the available materials of silicon oxynitrides, for 5 sccm of silane flow, without RF biasing. The used *H* material was the highest available for SiN_x with a refractive index equal to 1.83 at 2eV. The *L* layer was a silica layer with a 1.46 refractive index. For the medium index layer *M* we used the advantage of the accessibility to all the refractive indices in the SiO_xN_y range.

A refinement was done on this layer's index, in order to have an optimal transmission in the visible range. This led to a refractive index of 1.71 instead of 1.65 as start value before the refinement. Figure 5.20 shows the influence of this refinement on the transmission for treatment of one side only.

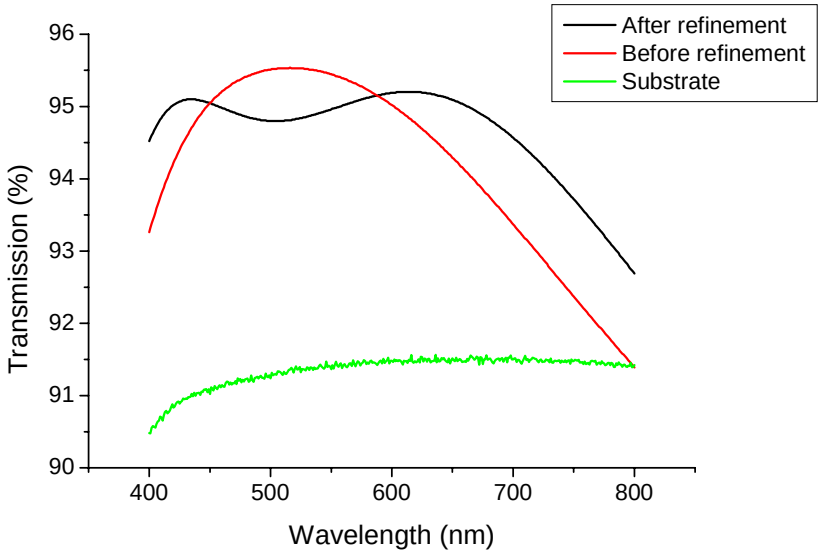

Figure 5.20. Refinement on the index of the first layer in the MHL stack.

The previous design was deposited twice using two different methods: the first with a thickness fit only and the second with thickness and index fit. The results of the two depositions are shown in Figure 5.21 where we remark that the index fit case was closer to the theoretical design than the thickness fit only.

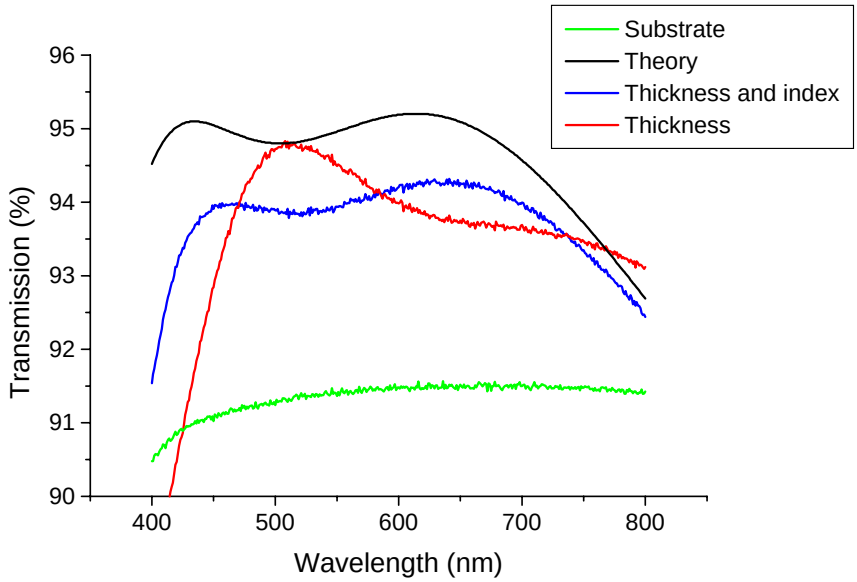

Figure 5.21. Comparison of thickness control with thickness and index control for an MHL AR coating.

5.4. Conclusion

In this chapter, the different methods of multi-wavelength kinetic ellipsometry control of deposition were explained. The influence of the plasma on the ellipsometric signal was analyzed and various ways to deal with it were considered.

Controlled deposition of a rugate based Fabry-Perot filter, multilayer Bragg reflector and 3-layer MHL antireflection coating were done, and showed good agreement with the targeted designs.

The physical thickness control showed to be suitable for cases where requirements are on optical thickness only. The index and thickness control was used for cases of more precise requirements.

References

[1] P. Bulkin, D. Daineka, D. Kouznetsov, B. Drévillon, *Deposition of optical coatings with real time control by the spectroellipsometry*, European Physics Journal of Applied Physics, Vol. 28, pp. 235–242, (2004).

[2] M. Kildemo, S. Deniau, P. Bulkin, B. Drévillon, *Real time control of the growth of silicon alloy multilayers by multiwavelength ellipsometry,* Thin Solid Films, Vol. 290-291, pp. 46-50, (1996).

[3] M. Kildemo, P. Bulkin, B. Drévillon, O. Hunderi, *Real-time control by multiwavelength ellipsometry of plasma-deposited multilayers on glass by use of an incoherent-reflection model,* Applied Optics, Vol. 36, Issue 25, pp. 6352-6359, (1997)

[4] A. Hofrichter, T. Heitz, P. Bulkin, B. Drévillon*, Ellipsometric method for real time control of thin film deposition on imperfect substrates,* Journal of Vacuum Science and Technology A, Vol. 20(3), pp. 702-706, (2002).

[5] D. Kouznetsov, A. Hofrichter, B. Drévillon, *Direct numerical inversion method for kinetic ellipsometric data. Presentation of the method and numerical evaluation,* Applied Optics, Vol. 41(22), pp. 4510-4518, (2002).

[6] A. Hofrichter, D. Kouznetsov, P. Bulkin, B. Drévillon, *Direct numerical inversion method for kinetic ellipsometric data. II. Implementation and experimental verification*, Applied Optics, Vol. 41, No. 22, 99. 4519-4525, (2002).

Chapter 6

Conclusion and Perspectives

During this study, a new MDECR PECVD reactor Venus, dedicated to the deposition of optical thin films based on silicon oxynitride alloys, was designed and constructed. The main points that had to be taken into consideration during the implementation of the reactor were the use of fast digital technology for mass flow control, high throughput turbomolecular pumping, accurate design of the gas distribution system and the computer control of growth in both feed-forward and ellipsometric control modes.

For optical coating technology, precise knowledge of the material dispersion is very important. We characterized our process and material properties using spectroscopic photo-elastic modulation ellipsometry and infrared transmission spectroscopy. Optical emission spectra were taken on the substrate and antenna levels and used to correlate changes in the plasma with trends in the deposited materials. By optimizing the magnetic field configuration and process conditions, very stable refractive indices in the range of 1.45-1.9 and good uniformity were obtained: for silica in the order of ±3 percent across a 200 mm wafer. FTIR spectroscopy confirmed the importance of RF biasing in depositing good quality oxide and nitride films.

The system is adapted for gradient index coatings as well as classical multilayer designs. This was demonstrated through the successful fabrication of rugate filters, rugate-based Fabry-Perot, gradient and MHL three-layer antireflection coatings. These filters were designed during the course of this thesis, using commercial software such as Optilayer and Essential Macleod, as well as software developed by the author.

It was found that the plasma has a significant influence on the ellipsometric signal during a multi-channel acquisition. Corrections of these influences were incorporated in the calibration procedure.

Ellipsometric control using a real-time least square fit method was also improved on the basis of optical thickness correction. This allowed the design wavelength to be placed within one percent of the target value.

The focus of the study, initially being ellipsometric control, has evolved with time to include the investigation of silane-based HDP PECVD in general. It was found that the currently accepted paradigm for low-pressure HDP systems is not correct, at least for silica deposition from silane and oxygen and such plasma reactors may not be considered as well-mixed (or well-stirred) reactors. Silane beam experiments clearly showed that the contribution of the primary precursor beam constitutes a very significant part of the growth rate.

Suggestions for future process improvement include:

- More extensive characterization of materials, available with current set of precursor gases, with inclusion of amorphous silicon and amorphous silicon carbide.
- Modification of the reactor by rotating the system 90 degrees, in order to position sample vertically and not horizontally, as multiple and long depositions increase the chance of coating delaminating from the reactor walls and falling onto the substrate, inducing defects in the coatings.
- Search for an efficient etching procedure, as simple plasma etching with $SF_6/O_2/Ar$ currently employed, given the ratio of biased to grounded surfaces, is not very efficient for wall cleaning, even with relatively high RF bias powers.
- Modification of the optical path for the ellipsometer by introducing several diaphragms in the analyzer and polarizer arms to reduce the influence of stray light from plasma.
- Taking into consideration the optical emission of the plasma and the substrate heating for more precise control of multilayer stacks and in order to implement a gradient index control method.
- Quadrupole mass spectrometry with differential pumping done simultaneously with OES.

General recommendations:

- A broader study of the optical materials available by ECR PECVD, such as titania and tantala for high index materials and possibly to search for other low index material, in order to enlarge the range of the refractive index, which is currently limited by silica and silicon nitride.

- To test a spectroscopic polarimeter MM16 for in-situ control applications, as it provides more redundancy of the data than the spectroscopic ellipsometer due to full Mueller matrix measurements and offers the possibility to determine roughness in real time and deal with anisotropic and depolarizing samples.

Appendix I

The Lorentz Classical Oscillator Model

The classical Lorentz oscillator[1,2] is one of the most widely used approximations for the modeling of wavelength-dependent complex refractive index of amorphous materials in spectroscopic ellipsometry and reflectometry.

It consists of the following two equations[3]:

$$n^2 - k^2 = 1 + \frac{A\lambda^2}{\lambda^2 - {\lambda_0}^2 + g\lambda^2/(\lambda^2 - {\lambda_0}^2)} \qquad (I.1)$$

$$2nk = \frac{A\sqrt{g}\lambda^3}{(\lambda^2 - {\lambda_0}^2)^2 + g\lambda^2} \qquad (I.2)$$

Where λ_0 is the oscillator central wavelength, A the oscillator strength, g the damping factor and n and k the real and complex parts of the refractive index. This set of coupled equations for n and k is consistent with the Kramers-Kronig relations[a]. The one on the right hand side of equation *(I.1)* represents the dielectric function at infinite energy (zero wavelength). It is usually replaced by a fitting parameter ε_∞ that represents the dielectric function at smaller wavelengths than measured. In *Delta-Psi II,* the implemented classical Lorentz oscillator model is given by:

$$\varepsilon = \varepsilon_\infty + \frac{(\varepsilon_s - \varepsilon_\infty){\omega_t}^2}{{\omega_t}^2 - \omega^2 + i\Gamma_0\omega} + \frac{{\omega_p}^2}{-\omega^2 + i\Gamma_D\omega} + \sum_{j=1}^{2}\frac{f_j\omega_{0j}^2}{\omega_{0j}^2 - \omega^2 + i\gamma_j\omega} \qquad (I.3)$$

[a] The Kramers-Kronig relations relate the real part of an analytical complex function to an integral containing the imaginary part of the function, and vice versa.

The Tauc-Lorentz Model

The Tauc-Lorentz model was applied in ellipsometry by Jellison et al.[4]. This model can be used to fit a complex refractive index and interpret the experimental spectroscopic ellipsometry results for amorphous materials[5,6]. It offers several benefits, such as reasonable values within the spectrum limits of applicability, it is Kramers-Kronig consistent and will fit data within the experimental error of the data[5].

The Tauc expression for the imaginary part of the dielectric function near the band edge, is given by [6]:

$$\varepsilon_2(E) = A_T \frac{(E - E_g)^2}{E^2} \Theta(E - E_g) \qquad (I.4)$$

Where *Eg* in equation *(I.4)* is the band gap of the material and *Θ* the Heaviside function, with *Θ(E<0) = 0* and *Θ(E≥0) = 1*. By multiplying this function with the complex dielectric function for a Lorentz oscillator, we obtain the Tauc-Lorentz expression for the imaginary part of the complex dielectric function:

$$\varepsilon_2(E) = \frac{AE_0\Gamma(E - E_g)^2}{E[(E^2 - {E_0}^2)^2 + \Gamma^2 E^2]} \Theta(E - E_g) \qquad (I.5)$$

E_0 represents the peak in the joint density of states, Γ is the broadening parameter and A the prefactor. Using Kramers-Kronig integration on equation *(I.5)*, we get the Tauc-Lorentz dielectric function's real part:

$$\varepsilon_1(E) = \varepsilon 1(x) + \frac{2}{\pi} P_{E_g}^{x} \frac{\xi \varepsilon_2(E)}{\xi^2 - E^2} d\xi \qquad (I.6)$$

With P being the Cauchy principle part of the integral and $\varepsilon_1(\infty) = 1$ (or greater than 1 if a large optical transition takes place at an energy greater than sampled by the ellipsometer).

References

[1] F.A. Jenkins, H.E. White, *Fundamentals of Optics*, McGraw-Hill, Auckland, pp. 482 – 486, (1981).

[2] E. Hecht, *Optics*, Fourth Edition, Addison-Wesley, San Francisco, Chapter 3, (2002).

[3] D. Poelman, P.F. Smet, *Methods for the determination of the optical constants of thin films from single transmission measurements: a critical review*, Journal of Physics D: Applied Physics, Vol. 36, pp. 1850 - 1857, (2003).

[4] G.E. Jellison Jr., F.A. Modine, *Parameterization of the optical functions of amorphous materials in the interband region*, Applied Physics Letters, Vol. 69, pp. 371 - 373, Errata Vol 69, p.2137, (1996).

[5] G.E. Jellison Jr., V.I. Merkulov, A.A. Puretzky, D.B. Geohegan, G. Eras, D.H. Lowndes, J.B. Caughman, *Characterization of thin-film amorphous semiconductors using spectroscopic ellipsometry*, Thin Solid Films, Vol. 377 – 378, pp. 68 – 73, (2000).

[6] J. Tauc, *Optical Properties of Solids*, p. 123, Plenum, New York, (1969).

Appendix II

List of publications and attended conferences

- Published papers:

- B. Haj Ibrahim, P. Bulkin, D. Daineka, B. Drevillon, *Optical thin films deposition by MDECR-PECVD,* SPIE Proceedings Vol. 5963, pp. 500-506, (2005).

- R. Botha, B. Haj Ibrahim, P. Bulkin, B. Drevillon, *Deposition of dielectrics using a matrix distributed electron cyclotron resonance plasma enhanced chemical vapor deposition system,* Article in press, Thin Solid Films, doi: 10.1016/ j.tsf.2006.11.184, (2006).

- Submitted papers:

- B. Haj Ibrahim, R. Botha, J.E. Bourée, P. Bulkin, B. Drévillon, "Correlation of side-lobe suppression between rugate filters and multilayer mirrors", Applied optics, April 2007.

- Conferences and training:

- Advances in Optical Thin Films, SPIE conference, Jena – Germany, September 2005.

- CIP 05, 15th international colloquium on plasma processes, SFV Société Françasie du Vide, Autrans – France, June 2005.

- 4th Workshop on Ellipsometry, Berlin - Germany, February 2006.

Bibliography

A

F. Abelès, *Annales de Physique 5*, pp. 596-640, 706-782, (1950).

J. Asmussen, *Electron cyclotron resonance microwave discharges for etching and thin-film deposition*, Journal of Vacuum Science and Techology A, Vol. 7(3), pp. 883 - 893, (1989).

J. Asmussen, M. Dahimene, *The experimental test of a microwave ion beam source in oxygen*, Journal of Vacuum Science and Technology B, Vol. 5(1), pp. 328 - 331, (1987).

K. Aumaille, A. Granier, M. Schmidt, B. Grolleau, C. Vallée, G. Turban, *Study of oxygen/tetraethoxysilane plasmas in a helicon reactor using optical emission spectroscopy and mass spectrometry*, Plasma Sources Science and Technology, Vol. 9, pp. 331 - 339, (2000).

R. Azzam, N. Bashara, *Ellipsometry and polarized light*, North Holland Personal Library, (1970).

B

A. Banerjee, T. DebRoy, *Optical emission investigation of the plasma enhanced chemical vapor deposition of silicon oxide films*, Journal of Vacuum Science and Technology A, Vol. 10(6), pp. 3395-3400, (1992).

P. Baumeister, Multilayer reflectors with suppressed higher-order reflectance peaks, Applied Optics, Vol. 31 (10), pp. 1568-1573, (1992).

P. Baumeister, Design of multilayer filters by successive approximations, JOSA, Vol. 48 (12), pp. 955-958, 1958.

S. Béchu, O. Maulat, Y. Arnal, D. Vempaire, A. Lacoste, J. Pelletier, *Multi-dipolar plasmas for plasma-based ion implantation and plasma-based ion implantation and deposition*, Surface and Coatings Technology, Vol. 186(1), pp. 170 - 176, (2004).

A. Bieder, A. Sonnenfeld, P. R. von Rohn, *Uniformity and composition of silicon oxide films on 3D geometries by plasma enhanced chemical vapor deposition*, Thin Solid Films, Vol. 515(4), pp. 2807-2813, (2006).

R. Botha, B. Haj Ibrahim, P. Bulkin, B. Drévillon, *Deposition of dielectrics using a matrix distributed electron cyclotron resonance plasma enhanced chemical vapor deposition system*, Article in press, Thin Solid Films, doi: 10.1016/ j.tsf.2006.11.184, (2006).

B.G. Bovard, *Graded index rugate filters: power-sine rugate mirrors,* SPIE Proceedings, Vol. 2046, pp.109-125, (1993).

B.G. Bovard, *Rugate filter theory: an overview*, Applied Optics, Vol. 32(28), pp. 5427-5448 (1993).

N.St J. Braithwaite, *Introduction to gas discharges*, Plasma Sources Science and Technology, Vol. 9(4), pp. 517 - 527, (2000).

C. Buzea, K. Robbie, *State of the art in thin film thickness and deposition rate monitoring sensors*, Reports on Progress in Physics, Vol. 68(2), pp. 385-409, (2005).

P. Bulkin, D. Daineka, D. Kouznetsov, B. Drévillon, *Deposition of optical coatings with real time control by the spectroellipsometry*, Eur. Phys. J. Appl. Phys. 28, pp. 235-242 (2004).

P.V. Bulkin, *Electron cyclotron resonance plasma enhanced chemical vapour deposition SiO_xN_y: Optical properties and applications,* PhD Thesis, Rand Afrikaans University, Johannesburg, South Africa, (1994).

P.V. Bulkin, P.L. Swart, B.M. Lacquet, *Effect of process parameters on the properties of electron cyclotron resonance plasma deposited slicon-oxynitride*, Journal of Non-crystalline Solids, Vol. 187, pp. 403 - 408, (1995).

P. Bulkin, R. Brenot, B. Drevillon, R. Vanderhaghen, *Structure and transport properties of integrated distributed electron cyclotron resonance grown micro-crystalline silicon*, Journal of Non-Crystalline Solids, Vol. 231, pp. 268 - 272, (1998).

C

A. Canillas, A. Pinyol, J. Sancho-Parramon, J. Ferré-Borrull, E. Bertran, *FTIR phase-modulated ellipsometry characterization of hydrogenated amorphous silicon nitride thin films with embedded nanoparticles*, Thin Solid Films, Vol. 455-456, pp. 167-171, (2004).

C.K. Carniglia, *Ellipsometric calculations for nonabsorbing thin films with linear refractive-index gradients*, Journal of the Optical Society of America, Vol. 7(5), pp. 848-856 (1990).

A. Chambers, R. K. Fitch, B. S. Halliday, *Basic Vacuum Technology*, 2nd Edition, Institute of Physics Publishing, IoP publishing, Bristol, (1998).

T.T. Chau, K.C. Kao, *Optical emission spectra of microwave oxygen plasmas and fabrication of SiO2 films*, Journal of Vacuum Science and Technology B, Vol. 14(1), pp. 527-532, (1996).

Z. Chen, K. Prasad, C.Y. Li, S.S. Su, D. Gui, P.W. Lu, X. He, S. Balakumar, *Characterization and performance of dielectric diffusion barriers for Cu metallization*, Thin Solid Films, Vol. 462-463, pp. 223-226, (2004).

B. Chapman, *Glow discharge processes: Sputtering and plasma etching*, John Wiley & Sons, pp. 49-75, (1980).

F.F. Chen, J.P. Chang, *Lecture notes on principles of plasma processing*, University of California, Los Angeles, (2002).

K. Coates, S. Morrison, S. Naraynan, A. Madan, *Deposition of Silicon Nitride to Improve the Conversion Efficiency of Multicrystalline Silicon Solar Cells*, Proceedings of the 16th European Photovoltaic Solar Energy Conference, Glasgow, p. 1279, (2000).

D

J.A.S. da Matta, R.M.O. Galvao, L. Ruchko, M.C.A. Fantini, P.K. Kiyohara, *Description and Characterization of a ECR Plasma Device Developed for Thin Film Deposition*, Brazilian Journal of Physics, vol. 33(1), pp. 123 – 127, (2003).

D. Daineka, P. Bulkin, G. Girard, B. Drévillon, *Simple method of gas flow ratio optimization in high rate deposition of SiO2 by electron cyclotron resonance plasma enhanced chemical vapor deposition*, Journal of Vacuum Science and Technology A, Vol. 22, pp.36-38 (2004).

D.M. Dobkin, M.K. Zuraw, D.M. Dobkin, *Principles of chemical vapor deposition*, Kluwer Academic Publishers, (2003).

C. Doughty, D.C. Knick, J.B. Bailey, J.E. Spencer, *Silicon nitride films deposited at substrate temperatures <100°C in a permanent magnet electron cyclotron resonance plasma*, Journal of Vacuum Science and Technology A, Vol. 17(5), pp. 2612-2618, (1999).

J.A. Dobrowolski, J.R. Pekelsky, R. Pelletier, M. Ranger, B.T. Sullivan, A.J. Waldorf, *Practical magnetron sputtering system for the deposition of optical multilayer coatings*, Applied Optics, Vol. 31(19), pp. 3784-3789 (1992).

J.A. Dobrowolski, *Optical properties of films and coatings*, in Handbook of Optics, Vol. I, (M. Bass, E. W. van Stryland, D. R. Williams, and W. L. Wolfe, editors), McGraw-Hill, (1995).

J.A. Dobrowolski, D. Poitras, P. Ma, H. Vakil, M. Acree, *Toward perfect antireflection coatings: numerical investigation*, Applied Optics, Vol. 41(16), pp. 3075-3083, (2002).

B. Drévillon, *Phase modulated ellipsometry from the ultraviolet to the infrared: In situ application to the growth of semiconductors*, Progress in Crystal Growth and Characteration of Materials, vol. 27(1), pp. 1-87, (1993).

F

U. Fantz, *Basics of plasma spectroscopy*, Plasma Sources Science and Technology, Vol. 15, pp. S137-S147, (2006).

A.J. Flewitt, A.P. Dyson, J. Robertson, W.I. Milne, *Low temperature growth of silicon nitride by electron cyclotron resonance plasma enhanced chemical vapour deposition*, Thin Solid Films, Vol. 383, pp. 172-177, (2001).

S. Furman, A.V.Tikhonravov, *Basics of optics of multilayer systems*, Editions Frontières, Gif-sur-Yvette, (1992).

G

A. Granier, M. Vervloet, K. Aumaille, C. Vallée, *Optical emission spectra of TEOS and HMDSO derived plasmas used for thin film deposition*, Plasma Sources Science and Technology, Vol. 12, pp. 89 - 96, (2003).

H

B. Haj Ibrahim, P. Bulkin, D. Daineka, B. Drévillon, *Optical thin films deposition by MDECR-PECVD*, SPIE Proceedings Vol. 5963, pp. 500 - 506, (2005).

S. M. Han, E. S. Aydil, *Study of surface reactions during plasma enhanced chemical vapor deposition of SiO_2 from SiH_4,* O2, and Ar plasma, Journal of Vacuum Science and Technology A, Vol. 14 (4), pp. 2062-2070, (2004).

S.M. Han, E.S. Aydil, *Plasma and surface diagnostics during plasma-enhanced chemical vapor deposition of SiO_2 from $SiH_4/O_2/Ar$ discharges*, Thin Solid Films, Vol. 290-291, pp. 427-434, (1996).

E. Hecht, *Optics*, Fourth Edition, Addison-Wesley, San Francisco, Chapter 3, (2002).

M.J. Hernandez, J. Garrido, J. Martinez, J. Piqueras, *Compositional and electrical properties of ECR-CVD silicon oxynitrides*, Semicond. Sci. Technol. 12, pp. 927-932, (1997).

A. Hofrichter, T. Heitz, P. Bulkin, B. Drévillon, *Ellipsometric method for real time control of thin film deposition on imperfect substrates*, J. Vac. Sci. Technol. A, Vol 20, Issue 3, pp. 702-706, (2002).

A. Hofrichter, D. Kouznetsov, P. Bulkin, B. Drévillon, *Direct numerical inversion method for kinetic ellipsometric data. II. Implementation and experimental verification*, Applied Optics, Vol. 41(22), pp. 4519-4525, (2002).

J. Hopwood, D.K. Reinhard, J. Asmussen, *Charged particle densities and energy distributions in a multipolar electron cyclotron plasma etching source*, Journal of Vacuum Science and Technology A, Vol. 8(4), pp. 3103 - 3112, (1990).

J. Hopwood, R. Wagner, D.K. Reinhard, J. Asmussen, *Electric fields in a microwave-cavity electron-cyclotron-resonant plasma source,* Journal of Vacuum Science and Technology A, Vol. 8(3), pp. 2904 - 2908, (1990).

A. Hofrichter, P. Bulkin, B. Drévillon, *Plasma enhanced chemical vapour deposition of SiO_xN_y in an integrated distributed electron cyclotron resonance reactor,* Applied Surface Science, 142, pp. 447-450, (1999).

J

S.N. Jasperson, D.K. Burge, R.C. O'Handley, *A modulated ellipsometer for studying thin film optical properties and surface dynamics,* Surface Science, Vol. 27, pp. 548-558 (1973).

S.N. Jasperson, *An improved method for high reflectivity ellipsometry based on a new polarization modulation technique*, Review of Scientific Instruments, Vol. 40, pp. 761-767, (1969).

G.E. Jellison Jr., V.I. Merkulov, A.A. Puretzky, D.B. Geohegan, G. Eras, D.H. Lowndes, J.B. Caughman, *Characterization of thin-film amorphous semiconductors using spectroscopic ellipsometry*, Thin Solid Films, Vol. 377 – 378, pp. 68 – 73, (2000).

G.E. Jellison Jr., F.A. Modine, *Parameterization of the optical functions of amorphous materials in the interband region,* Applied Physics Letters, Vol. 69, pp. 371 - 373, Errata Vol 69, p.2137, (1996).

G.E. Jellison Jr., B.C. Sales, *Determination of the optical functions of transparent glasses by using spectroscopic ellipsometry*, Applied Optics, Vol. 30(30), pp. 4310-4315,(1991).

F.A. Jenkins, H.E. White, *Fundamentals of Optics*, McGraw-Hill, Auckland, pp. 482 – 486, (1981).

N. Jiang, B. Agius, M. C. Hugon, J. Olivier, M. Puech, *Radio-frequency bias effects on SiO2 films deposited by distributed electron cyclotron resonance plasma enhanced chemical vapor deposition*, Journal of Applied Physics, Vol. 76, pp. 1847-1855, (1994).

K

J.C. Kemp, *Piezo-optical birefringence modulators: New use for a long-known effect*, Journal of Optical Society of America, Vol.59(8), pp. 950 – 954, (1969).

M. Kildemo, S. Deniau, P. Bulkin, B. Drévillon, *Real time control of the growth of silicon alloy multilayers by multiwavelength ellipsometry*, Thin Solid Films, Vol. 290-291, pp. 46-50, (1996).

M. Kildemo, P. Bulkin, B. Drévillon, O. Hunderi, *Real-time control by multiwavelength ellipsometry of plasma-deposited multilayers on glass by use of an incoherent-reflection model*, Applied Optics, Vol. 36(25), pp. 6352-6359, (1997).

D. Kouznetsov, A. Hofrichter, B. Drévillon, *Direct numerical inversion method for kinetic ellipsometric data. Presentation of the method and numerical evaluation*, Applied Optics, Vol. 41, Issue 22, pp. 4510-4518 (2002).

L

A. Lacoste, T. Lagarde, S. Béchu, Y. Arnal, J. Pelletier, *Multi-dipolar plasmas for uniform processing: physics, design and performance*, Plasma Sources Science Technology, Vol. 11, pp. 407-412, (2002).

L. Latrasse, A. Lacoste, J. Sirou, J. Pelletier, *High density distributed microwave plasma sources in a matrix configuration: concept, design and performance*, Plasma Sources Science and Technology, Vol. 16(1), pp. 7 -12, (2007).

D.F. Lai, J. Robertson, W.I. Milne, *Plasma oxidation of silicon using an electron cyclotron wave resonance (ECWR) oxygen plasma*, Thin solid films, Vol. 383, pp. 220-223, (2001).

A. Lacoste, T. Lagarde, S. Bechu, Y. Arnal, J. Pelletier, *Multi-dipolar plasmas for uniform processing: physics, design and performance*, Plasma Sources Science and Technology, Vol. 11, pp. 407 - 412, (2002).

M.A. Lieberman, A.J. Lichtenberg, *Principles of plasma discharges and materials processing, 2nd edition*, John Wiley & Sons, (2005).

M

A. Macleod, *Oblique incidence rules*, SVC Winter Bulletin, pp. 22-28, (Feb. 2006).

E. Meeks, R. S. Larson, P. Ho, C. Apblett, S.M. Han, E. Edelberg, E.S. Aydil, *Modeling of SiO_2 deposition in high density plasma reactors and comparisons of model predictions with experimental measurements*, J. Vac. Sci. Technol. A16 (2), pp. 544-563, (1998).

L. Martinu, *Plasma deposition of optical films and coatings: A review*, Journal of Vacuum Science and Technology A, Vol.18 (6), pp. 2619-2645, (2000).

P. Mak, G. King, T.A. Grotjohn, J. Asmussen, *Investigation of the influence of electromagnetic excitation on electron cyclotron resonance discharge properties*, Journal of Vacuum Science and Technology A, Vol. 10(4), pp. 1281 - 1287, (1992).

H.A. Macleod, *Thin Film Optical Filters, 2nd edition*, Macmillan, New York, (1986).

G. Minott, R. Sprague, B. Shnapi, *Rugate notch filters find use in laser-based applications*, Laser Focus World, Vol. 40(9), pp. 107 – 111,(September 2004).

W. Miyazawa, S. Tada, K. Ito, H. Saito, S. Den, Y. Hayashi, Y. Okamoto, Y. Sakamoto, *A large-area ECR processing plasma*, Plasma Sources Science and Technology, Vol. 5, pp. 265-267, (1996).

M. Moisan, J. Pelletier, *Microwave Excited Plasmas*, Elsevier Science, (1992).

M. Moisan, J. Pelletier, *Physique des plasmas collisionnels: Application aux décharges hautes fréquences*, EDP Sciences, (2006).

H. Muta, *Investigation of Electron Behaviour in ECR Plasmas Using a Self-Consistent Particle Wave Model*, Japanese Journal of Applied Physics, Vol. 38(7B), pp. 4455 - 4459, (1999).

N

S. Nakayama, *ECR plasma for thin film technology*, Pure and Applied Chemistry, Vol. 62(9), pp. 1751-1756, (1990).

S.V. Nguyen, K. Albaugh, *The characterization of electron cylcotron resonance plasma deposited nitride and silicon oxide films*, Journal of the Electrochemical Society, Vol. 136(10), pp. 2835-2940, (1989).

O

M. Ohring, *Materials science of thin films, deposition and structure, 2nd edition*, Elsevier Academic Press, (2002).

P

J. Pelletier, T. Lagarde, *Chemical vapour deposition in high-density low-pressure plasmas: reactor scale-up and performance*, Thin Solid Films, Vol. 241, pp. 240 - 246, (1994).

R. Petit, *Ondes Électromagnétiques en radioélectricité et en optique*, Masson, (1988).

M. Pirani, J. Yarwood, *Principles of Vacuum Engineering*, Chapmann and Hall, (1963).

D. Poelman, P.F. Smet, *Methods for the determination of the optical constants of thin films from single transmission measurements: a critical review*, Journal of Physics D: Applied Physics, Vol. 36, pp. 1850-1857, (2003).

D. Poitras, L. Martinu, *Simple method for determining slowly varying refractive-index profiles from in situ spectrophotometric measurements*, Applied Optics, Vol. 37(19), pp. 4160-4167, (1998).

D. Poitras, S. Larouche, L. Martinu, *Design and plasma deposition of dispersion-corrected multiband rugate filters*, Applied Optics, Vol. 41(25), pp. 5249-5255, (2002).

O.A. Popov, *High Denstiy Plasma Sources : Design, Physics and Performance*, pp. 251-311, Noyes Publications, (1995).

T.C. Pulick, *Guidelines for construction of low-pressure gas manifolds*, Journal of Vacuum Science and Technology, Vol 21(4), pp. 1032-1036, (1982).

R

J.R. Roberts, *Optical emission spectroscopy on the Gaseous Electronics Conference RF Reference Cell,* J. Re. Natl. Inst. Stand. Technol., Vol. 100(4), pp. 353-371, (1995).

S

H. Schlemm, A. Mai, S. Roth, D. Roth, K.-M. Baumgartner, H. Muegge, *Industrial large scale silicon nitride deposition at photovoltaic cells with linear micro-wave plasma sources*, Surface and Coating Technology, Vol. 174-175, pp. 208-211, (2003).

S. M. Suh, S. L. Girshick, U. R. Kortshagen, M.R. Zachariah, *Modeling gas-phase nucleation in inductively coupled silane-oxygen plasmas,* Journal of Vacuum Science and Technology A, Vol. 21 (1), pp. 251-264, (2003).

W.H. Southwell, *Gradient index antireflection coatings,* Optics Letters, Vol. 8(11), pp.584-586, (1983).

W.H. Southwell, R.L. Hall, *Rugate filter side-lobe suppression using quintic and rugated quintic matching layers,* Applied Optics, Vol. 28 (14), pp. 2949-2951, (1989).

B.T. Sullivan, G.A. Clarke, T. Akiyama, N. Osborne, M. Ranger, J.A. Dobrowolski, L. Howe, A. Matsumoto, Yizhou Song, Kazuo Kikuchi, *High-rate automated deposition system for the manufacture of complex multilayer coatings*, Applied Optics, Vol. 39(1), pp.157-167, (2000).

B.T. Sullivan, J.A. Dobrowolski, *Deposition error compensation for optical multilayer coatings: I. Theoretical description*, Applied Optics, Vol. 31(19), pp.3821-2835, (1992)

B.T. Sullivan, J.A. Dobrowolski, *Deposition error compensation for optical multilayer coatings: II. Experimental results-sputtering system*, Applied Optics, Vol. 32(13), pp. 2351-2360, (1993).

B.T. Sullivan, J.A. Dobrowolski, G. Clarke, T. Akiyama, N. Osborne, M. Ranger, L. Howe, A. Matsumoto, Y. Song, K. Kikuchi, *Manufacture of complex optical multilayer filters using an automated deposition system*, Vacuum, Vol. 51(4), pp.647-654, (1992).

T

M. Tadokoro, A. Itoh, H. Nakano, Z.L. Petrovic, T. Makabe, *Diagnostics of an Inductively Coupled Plasma in Oxygen*, IEEE Transactions on Plasma Science, Vol. 26(6), pp. 1724 - 1732, (1998).

J. Tauc, *Optical Properties of Solids*, p. 123, Plenum, New York, (1969).

A. Thelen, *Design of Optical interference Coatings*, McGraw-Hill, (1988).

J.C. Thomaz, J. Amorim, C.F. Souza, *Validity of actinometry to measure N and H atom concentration in N2-H2 direct current glow discharges*, Journal of Physics D: Applied Physics, Vol. 32, pp. 3208 - 3214, (1999).

W

M.R. Wertheimer, M. Moisan, *Processing of electronic materials by microwave plasma*, Pure and Applied Chemistry, Vol. 66(6), pp. 1343-1352, (1994).

G.M. Wells (Chairman), *The Application of Metallic Fluoride Reflection Reduction Films to Optical Elements*, Published at Frankford Arsenal, (October 1943).

H. Wu, D.B. Graves, M. Kilgore, *Two-dimensional simulation of compact ECR plasma sources*, Plasma Sources Science and Technology, Vol. 6, pp. 231-239, (1997).

Y

S.F. Yoon, K.H. Tan, Q. Zhang, M. Rusli, J. Ahn, L. Valeri, *Effect of microwave power on the electron energy in an electron cyclotron resonance plasma*, Vacuum, Vol. 61, pp. 29-35, (2001).

Z

J. Zhang, Z. Ren, R. Liang, Y. Sui, W. Liu, *Planar optical waveguide thin films growth by microwave ECR PECVD*, Surface and Coatings Technology, Vol. 131, pp. 116-120, (2000).